DEPARTMENT OF ONCOLOGY
Medical Sciences Division

Optimising Radiotherapy of Liver Tumours:
Radiobiology of Yttrium-90 Microsphere Treatment

Elliot Mitchell Abbott

St Cross College
University of Oxford

A thesis submitted for the degree of
Doctor of Philosophy

Under the supervision of
Professor Katherine Anne Vallis and Dr Nadia Falzone

Trinity 2019

Declaration

I declare that this thesis has been written solely by myself, and that it has not been submitted, in whole or in part, in any previous application for a degree. Except where stated otherwise by reference or acknowledgment, the work presented is a true and honest account of my own research, which was conducted ethically, and the results obtained are genuine.

Acknowledgements

I would like to express my sincere gratitude to all those who have supported me throughout my DPhil journey.

First and foremost, I am deeply grateful to my supervisors, Kate Vallis and Nadia Falzone, for their guidance and unwavering support throughout my academic development. From the moment I first met them in the Old Road Campus Research Building atrium and learned about the project that ultimately spawned this thesis, I knew I had found the mentors who shared my motivations and interests. Their experience and dedication were instrumental in the success of this work, and I am truly fortunate to have had the opportunity to work with them.

I also want to express my appreciation to Professors Mark Hill and Bleddyn Jones for enabling me to expand my work within their areas of expertise of dosimetry and radiobiology. In addition, I am grateful to the members of my thesis committee for their time and feedback throughout my DPhil studies. I must also mention, Dr Sarah Norman for teaching me how to write with impact. Furthermore, Dr Christiana Kartsonaki has been an instrumental collaborator helping to make sense of the bench and clinical data through statistical inference. Their diverse perspectives and expertise have helped me to refine my research questions and methodology.

I would like to acknowledge the support I received from my colleagues and labmates at the Radiobiology Research Institute. Their feedback and encouragement, particularly from Drs Martin Gill, Ole Tietz, Rachel Anderson, Irini Skaripa-Koukelli, Javian Malcolm, and Bas Bavelaar, have been critical in shaping my research and advancing my professional development. Their support and friendship have made my journey much more enjoyable.

I am also grateful to The Department of Oncology for providing me with the resources, facilities, and funding that have enabled me to conduct my research. Specifically, I would like to acknowledge grants from Cancer Research UK (CRUK, Grant No. C5255/A15935) and the Medical Research Council (MRC, Grant No. MC_PC_12004), as well as John Prentice and Kyle Hallett at the Mechanical Workshop for development of the ClonogenCity experimental container.

I want to further acknowledge from clinical collaborators who enabled this research to translate bench findings to their implications in the clinical setting. I am deeply grateful to the team at TriStar Centennial Clinic in Nashville, especially Dr Andy Kennedy, for providing me with access to relevant data and experience that highlighted clinically impactful areas. I would also like to thank Pamela Purcell and Caroline Hale for curating the patient datasets, and Justin Roper for his assistance with radiotherapy treatment planning. Additionally, I want to acknowledge the team at The Churchill Hospital, including Drs Ricky Sharma, Tessa Greenhalgh, Helen Winter, and Phil Boardman, for their invaluable support related to patient treatment. I am also grateful to Nigar Syed for her assistance with data curation, the Radiopharmacy for supplying yttrium-90, and the physicists of the Radiotherapy Unit for their help with the use of LINAC resources.

Furthermore, I would like to express my gratitude to the industry collaborators who have contributed to my research. Jessica Heritage and Lindsay Sears at Sarah Cannon Cancer

Institute provided valuable research resources and support that enabled me to conduct the clinical trials successfully. I am also thankful to Adam Neff and Daniel Parvin at MIM Software for providing their image analysis software and automated workflow support, which greatly facilitated the analysis of these datasets. Their expertise and contributions have been essential to the success of my project, and I am grateful for their assistance.

Finally, I am forever indebted do my family and friends for foundational support that was essential to the successful completion of this work. My parents, Amy and Dan Abbott, brother Aaron Abbott, grandmother Yvette Nissenbaum, and close friends Dan Harris, Bo Whitesman, and Edward Sanders each played a fundamental personal role in getting me into and completing this DPhil journey.

Abstract

Background: Yttrium-90 selective internal radiotherapy (^{90}Y SIRT) is a treatment aimed at improving tumour control within the liver, from which the disease burden is the most common cause of death. FOXFIRE, SIRFLOX, SARAH and other phase 3 clinical trials of SIRT indicated response in the liver but not increased overall survival. The present work aims to address this phenomenon and hypothesises that optimising treatment around absorbed dose to the liver would result in improved patient outcomes. In addition, the present work hypothesises that treatment planning could be further optimised by considering the factors of radiosensitivity, perfusion, and treatment paradigms to enhance uncomplicated tumour control in the liver and therefore overall survival.

Materials and Methods: Clonogenic assays of cancer cell lines were used to assess radiosensitivity from exposure to ^{90}Y SIRT and EBRT (LINAC and ^{137}Cs). Radiobiological parameters from the survival curves were adapted to a biological effective dose (BED) model useful to compare radiation response between ^{90}Y SIRT and EBRT. In a group of colorectal carcinoma (CRC) patients treated with ^{90}Y SIRT, tumour volumes were contoured and absorbed dose was measured to assess the dose-response relationship. An additional subcohort was analysed based on clinical imaging of perfusion in the liver from dynamic contrast enhanced magnetic resonance imaging (DCE MRI) and perfusion CT (pCT). Perfusion modelling parameter maps in the tumours were used to assess possible associations with dose deposition and response to ^{90}Y SIRT. Additional BED models were applied to a second cohort of ten hepatocellular carcinoma (HCC) patients that received both ^{90}Y SIRT and EBRT to assess tumour volumes, dose, and radiobiological endpoints. Finally, stereotactic ablative radiotherapy (SABR) treatments were planned considering prior ^{90}Y SIRT through radiobiological modelling.

Results: Radiation response from clonogenic assays of CRC cell lines yielded radiobiological fit parameters for ^{90}Y SIRT. These findings suggested greater resistance to ^{90}Y therapy than to either ^{137}Cs or LINAC exposures. A mixed statistical model combining these findings resulted in BED parameters for ^{90}Y SIRT. A dose-response relationship was demonstrated in the CRC patient cohort. Perfusion imaging from the subcohort generally revealed statistically significant relationships between perfusion parameters and dose or response for pCT but not for DCE MRI. In the HCC patient cohort, a methodology was demonstrated to combine doses from different LINAC and ^{90}Y SIRT treatments. Exploratory SABR plans, considering equivalent dose deposition from ^{90}Y SIRT, achieved treatment profiles comparable to those of SABR alone.

Conclusions: The clonogenic assay results extend the BED model and provide a framework for general consideration of ^{90}Y SIRT radiobiology. This work established a framework for such future analyses and identified several hypotheses which could have clinical application for additional radiotherapy in ^{90}Y SIRT patients. Biological response *in vitro* and in patients suggests there could be clinical utility for radiobiological modelling of ^{90}Y SIRT. Biological response to ^{90}Y SIRT is complex and future clinical trials are necessary to definitively appreciate the clinical response to radiation dose.

Dissemination

This thesis is based on the following original publications.

I. Master's dissertation supporting methodology of Section 2.3 starting on page 33

Abbott EM. A method towards patient-specific dosimetry of ^{90}Y SIRT in the treatment of liver metastases. *University of Oxford*. 2015.

II. Clonogenic assays and radiobiological analysis of colorectal cancer cell lines exposed to ^{90}Y SIRT as detailed in Chapter 3

Lee BQ*, **Abbott EM***, Able S, Thompson JM, Hill MA, Kartsonaki C, Vallis KA, Falzone N. Radiosensitivity of colorectal cancer to 90Y and the radiobiological implications for radioembolisation therapy. *Phys Med Biol*. 2019;64:135018. doi:10.1088/1361-6560/ab23c4

III. Colorectal cancer patient cohort that received ^{90}Y SIRT, relevant to Chapter 4

Abbott EM*, Falzone N*, Lee BQ, Kartsonaki C, Winter H, Greenhalgh TA, McGowan DR, Syed N, Denis-Bacelar AM, Boardman P, Sharma RA, Vallis KA. Impact of radiobiologically-informed dose prescription on increasing potential clinical benefit of yttrium-90 SIRT in colorectal cancer patients. *J Nucl Med*. 2020;jnumed.119.233650. doi:10.2967/jnumed.119.233650

IV. PERFORM clinical trial of perfusion imaging relevant to Section 4.5 on page 82

Abbott EM*, Winter H*, Kartsonaki C, Virdee PS, Irving B, Papiez B, Brown E, Weir G, Mills J, Anderson M, Boardman P, Falzone N, Vallis KA, Sharma RA. Perfusion CT in the FOXFIRE trial to study blood flow to liver metastases (PERFORM). August 5, 2011 ed. ClinicalTrials.gov Identifier: NCT01410760 US National Library of Medicine; 2023. (In preparation.)

V. Hepatocellular cancer patient cohort that received both EBRT and ^{90}Y SIRT, relevant to Chapter 5

Abbott EM, Young RS, Hale C, Mitchell K, Falzone N, Vallis KA, Kennedy A. Stereotactic inverse dose planning following yttrium-90 selective internal radiotherapy in hepatocellular cancer. *Adv Radiat Oncol*. 2020. doi:10.1016/j.adro.2020.11.002

Where applicable, joint first authorship is indicated with an asterisk (*).

Abbreviations

^{137}Cs	Caesium-137 (radioisotope)
^{166}Ho	Holmium-166 (radioisotope)
^{90}Y	Yttrium-90 (radioisotope)
$^{90}YCl_3$	Yttrium-90 chloride
^{99m}Tc-MAA	Metastable technetium-99 (radioisotope) macro-aggregated albumin
BED	Biological effective dose
BF	Blood flow (perfusion parameter)
BSA	Body surface area
BV	Blood volume (perfusion parameter)
BVH	BED volume histogram
CI	Confidence interval
CR	Complete Response
CRC	Colorectal carcinoma
CT	Computed tomography
D_{70}	minimum dose to 70% of the volume
DCE	Dynamic contrast-enhanced
DMEM	Dulbecco's modified Eagle's medium
DVH	Dose volume histogram
EBRT	External beam radiation therapy
EES	Extravascular extracellular space (perfusion modelling)
EQD	Equivalent dose by fractionation
EUD	Equivalent uniform dose
EUBED	Equivalent uniform biological effective dose
G	Lea-Catcheside protraction factor
Gy	Gray (unit)
HCC	Hepatocellular carcinoma
ICC	Intrahepatic cholangiocarcinoma
k_{ep}	Rate constant of backflux from the EES to the blood plasma
K^{trans}	Transfer constant (perfusion modelling)
LED	Local energy deposition
LET	Linear energy transfer
LDM	Local deposition method
LINAC	Linear accelerator
LQ	Linear quadratic model
MBq	Megabecquerels (unit)
MC	Monte Carlo
MIM	MIM software
MIRD	Medical internal radiation dose
MRI	Magnetic resonance imaging
MTT	Mean transit time (perfusion parameter)
MTS	Cell viability assay

MV	Megavolt (unit)
OAR	Organ at risk
OR	Odds ratio
OS	Overall survival
OSEM	Ordered subset expectation maximisation
PBS	Phosphate buffered saline
pCT	Perfusion computed tomography
PD	Progressive Disease
PET	Positron emission tomography
PR	Partial Response
PS	Permeability-surface area product (perfusion parameter)
RBE	Relative biological effectiveness
RE	Relative effectiveness
RECIST	Response Evaluation Criteria in Solid Tumours
RFA	Radiofrequency ablation
RILD	Radiation induced liver disease
RNT	Radionuclide therapy
RSD	Relative standard deviation
RTOG	Radiation Therapy Oncology Group
SABR	Stereotactic ablative radiation therapy
SBRT	Stereotactic body radiation therapy
SD	Stable Disease
SF	Surviving fraction
SIRT	Selective internal radiation therapy
SPECT	Single photon emission computed tomography
TACE	Trans-arterial chemoembolisation
TARE	Trans-arterial radioembolisation
$\mathbf{T_{phys}}$	Radioisotope physical half-life
$\mathbf{T_{rep}}$	Repair half-time
$\mathbf{v_e}$	Fractional volume (perfusion modelling)
vRECIST	Volumetric RECIST
WHO	World Health Organisation

Table of Contents

Table of Figures

Table of Tables

1 Introduction

1.1 Clinical background

With the ever-increasing incidence of primary and metastatic cancer in the liver, there is a growing demand for liver-directed therapies to control and cure malignant tumours. Several therapeutic options exist, including surgery, external beam radiotherapy, ablation, and embolisation techniques (*1*). Surgical resection of liver disease is associated with the highest cure rate. However, many patients are ineligible due to the size or location of tumours and this approach is highly invasive. Thermal ablative techniques including cryoablation, radiofrequency ablation (RFA), and microwave ablation may offer a survival advantage, but are typically paired with other liver-directed treatment (*2*). Radiation therapy using conventional external beam radiotherapy (EBRT) is challenging as liver parenchyma is relatively radiosensitive such that the risk of liver decompensation from radiation toxicity, also known as radiation induced liver disease (RILD), constrains deliverable doses (*3*). The advent of highly conformal radiotherapy through stereotactic ablative radiotherapy (SABR), also known as stereotactic body radiotherapy (SBRT), has allowed delivery of high doses to disease sites with marked success. However, due to the high doses delivered per fraction (typically 5 fractions of 10 Gy), patient alignment and breathing corrections are necessary to ensure the delivered dose is limited to well-defined tumours while avoiding normal liver.

Embolisation techniques involve the administration of microscopic beads—or microspheres—via catheterisation, which accumulate in the arteriolar side of the capillary bed. The microspheres are preferentially deposited in the arterially-supplied tumours as they become trapped in the abnormal, tortuous microvasculature. Chemoembolisation, also known as trans-arterial chemoembolisation (TACE), involves loading the

microspheres with chemotherapeutic agents for a more locally-delivered dose. Alternatively, the focus of this thesis involves microspheres labelled with therapeutic radionuclides. This approach is referred to as radioembolisation, trans-arterial radioembolisation (TARE), or selective internal radiation therapy (SIRT). Radionuclides that have been used in radioembolisation techniques include iodine-131, rhenium-186, and rhenium-188, among others (*4*). Notably, holmium-166 (^{166}Ho; QuiremSpheres®, Terumo Europe) is currently emerging due to its strong imaging properties. However, despite lacking good-quality gamma photons for imaging, the most widely adopted radionuclide is yttrium-90 (^{90}Y), which has several pragmatic advantages including short irradiation distance for protection of radiation workers and a half-life of 2.67 days (T_{phys} = 64.1 h). The ^{90}Y fully decays after treatment and only about 5% of the initial injected activity remains after 11 days. ^{90}Y is a nearly pure beta-emitter (β^- decay to zirconium-90 (^{90}Zr) with a decay energy of 2.28 MeV) with a small branching ratio of 1.4×10^{-8} of 2.186 MeV γ-rays (Figure 1.1-1), which can be imaged with positron emission tomography (PET) or single photon emission computed tomography (SPECT) scanners (*5*). PET imaging is acquired from the 0+ excited state of ^{90}Zr whereby 1.76 MeV emissions result in the 511 keV signal. While limited by its broad spectral band, SPECT imaging is acquired from bremsstrahlung emissions with a mean energy of 0.933 MeV. For this reason, ^{90}Y has been used in several other therapies: ^{90}Y-DOTOTOC, ^{90}Y-biotin (IART®), ^{90}Y-iritumomab tiuxetan (IT), ^{90}Y-lipidiol (Lipioca®, poppy seed oil).

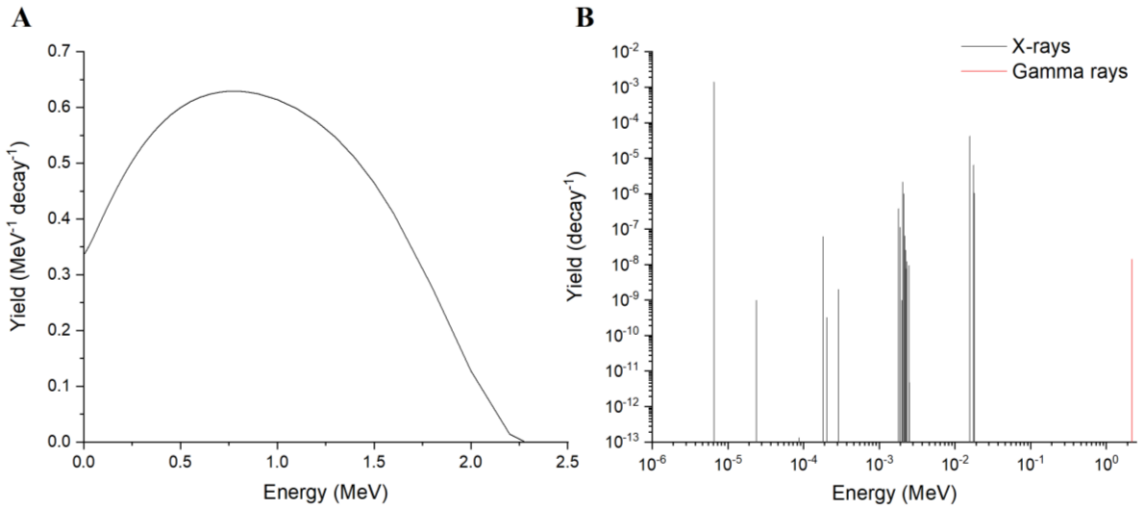

Figure 1.1-1 Emission spectra of ^{90}Y. The data for the radiation spectra of (A) betas (mean energy of 0.933 MeV) and (B) photons were acquired from the unabridged decay data in the MIRD-RADTABS software (MIRD tabulation, Ver. 2.2) (*5*).

SIRT with ^{90}Y is used in the SIR-Spheres® (Sirtex) and TheraSphere® (BTG) medical devices which vary mainly in their physical properties (Table 1.1-1). They are used for palliation, debulking, radiation segmentectomy, prior to liver surgery, patients with portal vein thrombosis, or sometimes paediatric settings (*6*).

Table 1.1-1 Comparison of SIRT products.

Product	SIR-Spheres®	TheraSphere®
Manufacturer	Sirtex Medical Ltd (North Sydney, Australia)	BTG plc (London, United Kingdom)
Sphere material	Resin	Glass
Sphere diameter (μm)	32.5±2.5 (range 20-60)	25 (range 20-30)
Specific gravity (g/mL)	1.6	3.6
Activity per sphere (Bq)	50 (range 40-80)	2500
Activity location	Surface	Embedded
Number of spheres per GBq (million)	20	0.4

SIRT was developed for used in the liver but has also been explored for application in kidneys in a porcine model (*7*). Gall bladder, lung, normal liver, and stomach are common off-target organs at risk (OAR) due to complications such as undesired shunting during administration. Targeted tissues include hepatocellular carcinoma (HCC), intrahepatic cholangiocarcinoma (ICC, also known as IHCC or bile duct cancer), and metastases from neuroendocrine, breast, colorectal carcinoma (CRC, also known as colon, rectal, or bowel cancer), pancreatic, melanoma, prostate, pancreatic acinar cell carcinoma (PACC), and renal cell carcinoma (RCC).

SIRT is delivered via a catheter which is inserted in the femoral artery, then fed through the aorta and into the hepatic artery (Figure 1.1-2). Different branches of the hepatic artery supply blood to the various liver lobes and the catheter is steered selectively among these to administer the dose. Radiopaque dye and fluoroscopy are utilised during SIRT administration to visualise blood flow and optimise catheter positioning. Several days prior to treatment, a workup session with metastable technetium-99 macro-aggregated albumin

(^{99m}Tc-MAA) is administered to identify gastric or pulmonary shunting which could lead to radiation pneumonitis or gastric ulceration if ignored. Undesired shunting is occluded with coils to redirect blood flow through the liver. The MAA particles of comparable size (10-60 μm) to SIRT microspheres disintegrate into smaller particles and are removed by the body through phagocytosis (*8*).

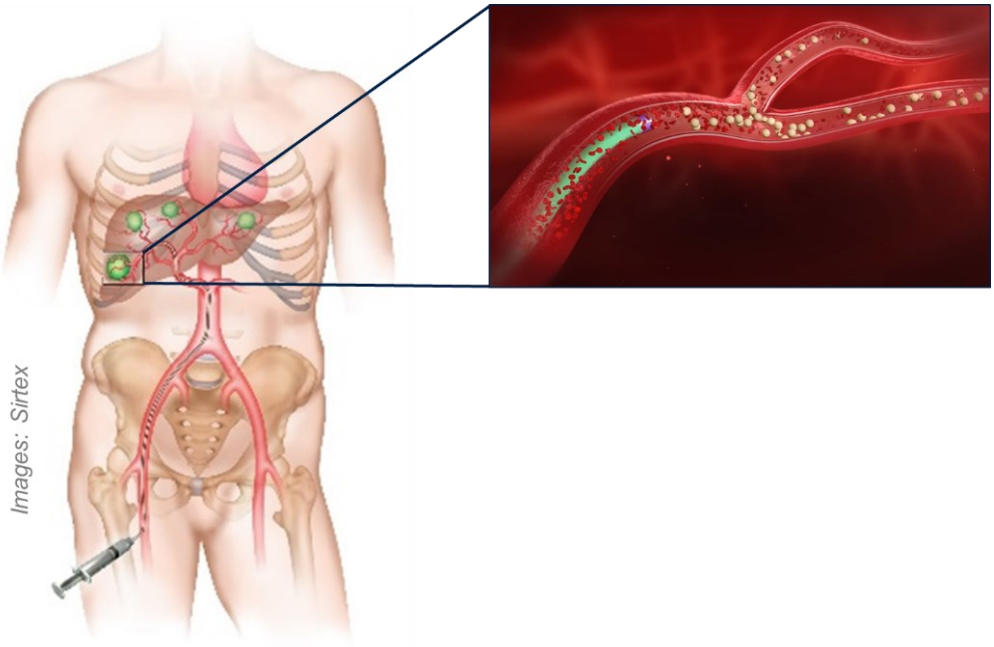

Figure 1.1-2 ^{90}Y SIRT delivery mechanism Catheterisation through the femoral artery is selectively steered into various branches of the hepatic artery where the ^{90}Y microspheres are injected and settle upstream of the tumours.

Tumour targeting by SIRT takes advantage of the embolisation of arterial blood to liver tumours. The microspheres embolise and remain in situ as evidenced by their presence in resected liver histology (*9*) and damage caused from irradiating the surrounding tumour tissue (Figure 1.1-3). Sometimes the tumours grow so large that the blood supply to the centre is insufficient. This results in tumours which remain in a chronic state of hypoxia, which decreases the efficacy of radiation due to the absence of the oxygen-enhancement effect. In addition, the poor vasculature in the central tumour and large intratumoural

pressure often develops necrotic cores and limits microsphere uptake preferentially to the tumour rim.

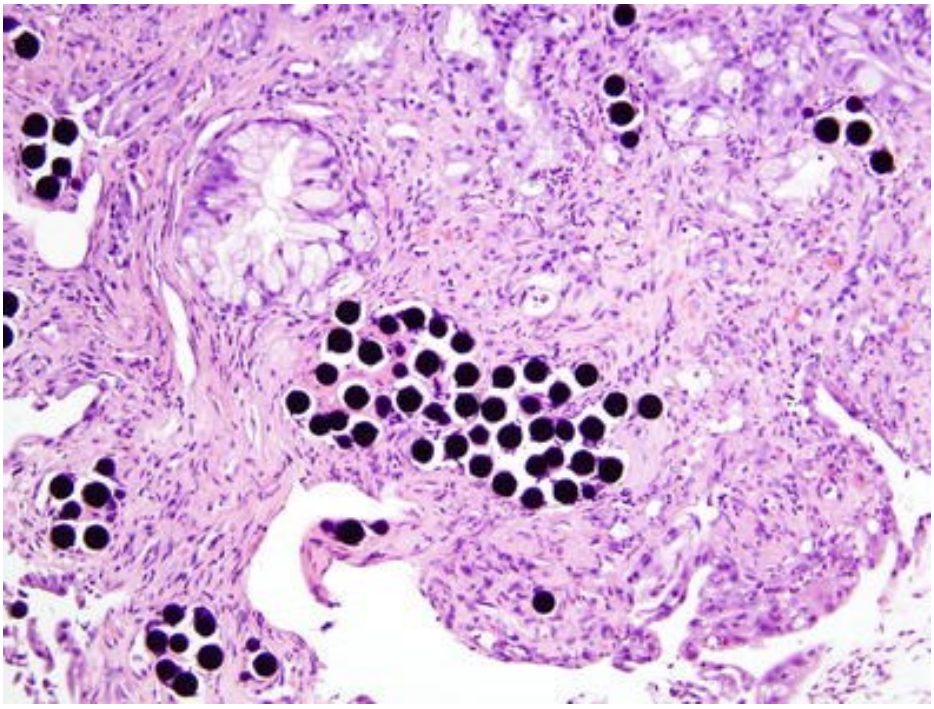

Figure 1.1-3 Post-mortem sample of ^{90}Y SIRT in situ. Histological findings demonstrated the black opaque microspheres in distinct clusters in damaged epithelium (*10*). Adapted from Vieth, M. and Montgomery, E. (2017) 'Medication-associated gastrointestinal tract injury', Virchows Archiv., 470(3), doi: 10.1007/s00428-017-2077-3

1.2 Optimisation opportunities

Use of ^{90}Y SIRT has continued to grow in the USA and in the UK since National Health Service (NHS) commissioning was recently extended. However, with the high mortality rates worldwide of primary cancers addressed by SIRT (Figure 1.2-1), there is opportunity to optimise its delivery in an impactful way (*11*). For example, colorectal carcinoma (CRC) accounts for about one in ten cancer cases worldwide. Due to metastasis from the portal venous blood from the bowel (Figure 1.2-2), about half of CRC patients present with or

develop metastases to the liver (*12*), whereby such a liver-directed therapy would be appropriate. There remains a need for optimisation of ^{90}Y SIRT through personalisation or patient selection.

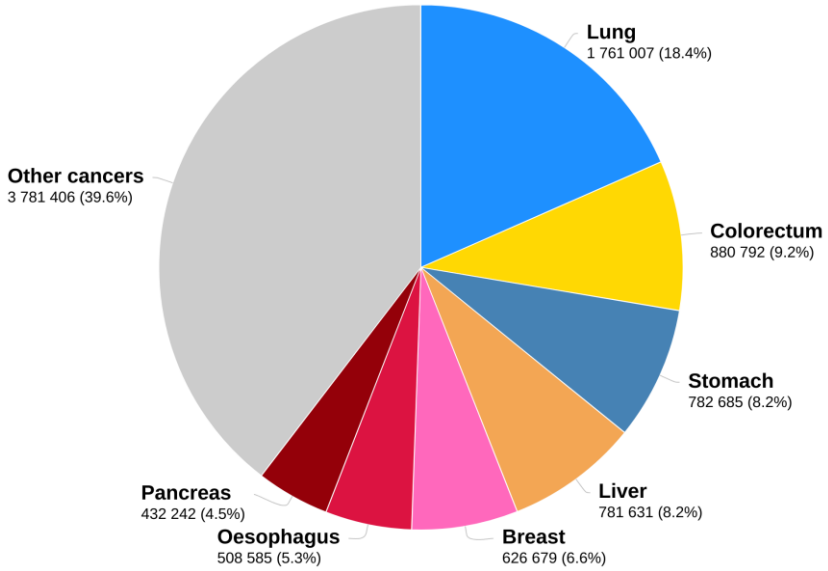

Figure 1.2-1 Estimated worldwide cancer mortality in 2018. Of the 9.6 million cancer deaths worldwide in 2018, CRC and HCC primaries investigated here comprised the second and fourth highest percentages including all ages and sexes (*11*). (Data source: Globocan 2018, Graph production: Global Cancer, http://gco.iarc.fr)

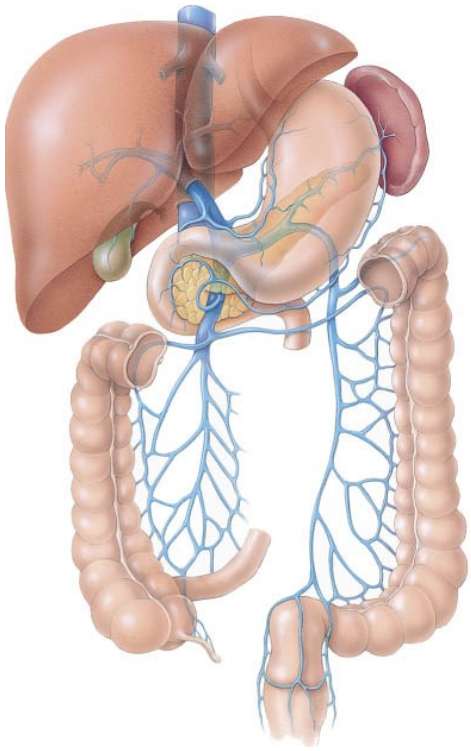

Figure 1.2-2 The hepatic portal venous system Blood draining from the bowels is first filtered through the liver before returning to the heart. CRC metastasises through the circulating tumour cells which settle in the capillary bed of the liver. (Image was sourced from http://www.pbi4u.ca/images/custom/Hepatic%20portal%20system.jpg)

SIRT has been investigated several phase III multicentre, prospective, open-label, randomised controlled trials. The SIRFLOX, FOXFIRE, and FOXFIRE-Global trials were aimed at evaluating the efficacy of SIRT in combination with FOLFOX chemotherapy against FOLFOX alone, the standard of care (*12–14*). The trials recruited a total of 1,103 patients with chemorefractory and unresectable colorectal cancer metastases confined to the liver. These trials collectively demonstrated an improvement in liver-specific disease control but did not show a clinically significant improvement in overall survival (OS). Some outcome predictors were identified excluding age or the presence of a Kras mutation and included the primary tumour site (left versus right colorectal primary) (*15*). The SARAH trial was a European study of 467 patients that evaluated OS and toxicity in HCC

patients receiving SIRT against the standard of care, sorafenib systemic therapy (*16*). It was found that SIRT offered no significant improvement in OS but was associated with a significantly better quality of life as measured by the European Organisation for Research and Treatment of Cancer (EORTC) quality of life questionnaire (QLQ-C30). As a result, questions have raised about the importance of these results to the future use of SIRT. For example, dose distribution considerations were not undertaken although dosimetry is highly predictive of response in conventional therapy settings.

While current consensus guidelines recommend SIRT as a treatment option for metastatic CRC, they do not require personalised dosimetry (*17–19*). Instead, activity prescription is based on simple parameters such as the disease burden in the liver and body surface area (BSA) estimation using a model based on patient weight and height. Although simple and convenient, these prescription approaches are more typical of systemic therapies. However, SIRT is selectively targeted in the liver and the deposited ^{90}Y can be measured to appreciate the distribution of the ^{90}Y microspheres in normal tissue and among individual tumours. Such physical measurements of dose have been the cornerstone of conventional EBRT, which has consequently achieved great success. In this way, several studies have demonstrated associations of absorbed radiation dose with the efficacy and toxicity of SIRT. SIRT dose was shown to correlate with tumour response based on response evaluation criteria in solid tumours (RECIST) 1.1 (*20*,*21*), volumetric RECIST (vRECIST) (*21–24*), and change in fluorodeoxyglucose (FDG) PET total lesion glycolysis (TLG) metabolism metrics (*25–28*).

Despite these successes, ^{90}Y SIRT dosimetry is inherently retrospective in nature as quantitative imaging of the ^{90}Y distribution can only be performed after the microspheres are placed, at which point they become permanently lodged and cannot be removed. Some prospective approaches are taken to aid in prediction of ^{90}Y SIRT accumulation. During

the workup phase for ^{90}Y SIRT, ^{99m}Tc-MAA is used to assess hepatopulmonary shunting from PET, SPECT, or planar scintigraphic imaging. However, despite studies that showed ^{99m}Tc-MAA imaging to predict response, it has generally proved to poorly predict ^{90}Y SIRT microsphere deposition (*29*,*30*).

The lack of quantitative and spatially-resolved tumour dosimetry for SIRT may result in inferior absorbed tumour dose. Consequently, the probability of achieving therapeutic response without toxicity may be reduced. Further adding to this issue, the biological response to ^{90}Y SIRT has been assumed from parameters observed in EBRT. This assumption is misplaced due to differences in the radiation quality, uniformity of coverage, and dose rate: 1-5 Gy/min for 6 megavolt (MV) linear accelerator (LINAC) versus 0.001-0.006 Gy/min for ^{90}Y SIRT (*9*,*31*,*32*). However, some studies have embraced radiobiological modelling from EBRT after applying a theoretical correction term, the Lea-Catcheside protraction factor, which is based on a first-principles derivation of the linear-quadratic model (see Section 8.4.1.2 on page 170) accounting for monoexponential radionuclide decay and cell damage repair functions (*33*). Among the earlier studies, Cremonesi et al. applied radiobiological parameters from EBRT to assess the merits of multi-cycle ^{90}Y SIRT treatment (*34*). They concluded from a radiobiologic argument that a multi-cycle approach could allow for the administration of higher activities, increasing tumour irradiation while limiting detrimental radiation effects on normal liver (*34*). Strigari et al. applied radiobiological parameters from EBRT experience to a cohort of HCC patients who received ^{90}Y SIRT and concluded that the radiobiologically-informed dosimetry could improve the therapeutic approach (*20*).

The appreciation of tissue radiation response on dose-response effect has been critical to the triumphs of EBRT. Dosimetry and radiobiologically-informed treatment planning, i.e. fractionation and external beam dose accumulation from prior radiation therapies, are

standardised across treatment centres. Yet, for radionuclide therapy (RNT), dosimetry and radiobiology are seldom even utilised in the clinic (*35*,*36*). While doses of activity in megabecquerels (MBq) for ^{90}Y SIRT are prescribed using the BSA method or by tables, absorbed doses in gray (Gy) have been shown to span from 50-200 Gy (*20*,*27*,*37*,*38*). Because a dose-response effect has been established in recent years for ^{90}Y SIRT (*20*,*27*,*38*), such deviations might be the key to further optimise treatment. In the wake of the recently reported phase III clinical trials, it has become apparent to many in the field that personalised dosimetry and radiobiological considerations could play an increased role in predicting treatment outcomes.

Additional personalised measures may further play a useful role for predicting outcome such as physiological endpoints. Perfusion imaging is a radiological measure of the vascularity and flow of blood throughout a tissue. Several perfusion imaging techniques exist, including perfusion computed tomography (pCT) and dynamic contrast-enhanced (DCE) magnetic resonance imaging (MRI) (*39*,*40*). These methods rely on change in signal, e.g. Hounsfield units from computed tomography (CT) attenuation, tracked over time as an intravenously injected bolus of dye passes through the liver. Perfusion models exist to describe the kinetics of the dye (*39*,*41*). Model parameters can be calculated on a voxel-wise basis to create maps of perfusion characteristics. Liver perfusion characteristics have shown to increase for tumours relative to normal tissue. Response to treatment has shown to decrease with normalisation of perfusion parameters (*39*). For these reasons, and because ^{90}Y SIRT is a vascularly-delivered treatment, perfusion imaging could be a predictor of microsphere deposition and tumour response (*42*). Moreover, the vascular system is responsible for distributing oxygen throughout the body. The presence of oxygen is highly implicated in tumour growth and the biological effectiveness of radiotherapy. Under normoxic conditions, hepatic tumours grow feeding off the oxygen-rich arterial

blood supply of the liver. As tumours grow, their interstitial pressure and abnormal vasculature can create hypoxic or intermittently hypoxic conditions which reduce activity of the tumour. But these also reduce the effectiveness of radiotherapy, which relies on reactive oxygen species to induce damage. Understanding the delivery of oxygen to liver tumours from vascular perfusion could inform methods to improve the effectiveness of ^{90}Y SIRT.

1.3 Radiobiology

Dosimetry for ^{90}Y SIRT has become increasingly integrated in the clinic in recent years (*43*). However, the incorporation of radiobiological modelling with parameters specific to ^{90}Y SIRT has not yet emerged in clinical practice. Radiobiological measures based on the linear-quadratic (LQ) model, such as biological effective dose (BED) and equivalent dose by fractionation (EQD), mandate a deep understanding of the underlying parameters with respect to protracted ^{90}Y exposure (*34*). While radiobiological measures for ^{90}Y SIRT are commonly modelled based on an α/β ratio, it has been recognised in the literature that a linear-only model is a reasonable simplification in the case of ^{90}Y SIRT with a low β-term (*44*). Several studies have assumed parameters based on EBRT experience for tumour and normal liver in the context of ^{90}Y SIRT (Table 1.3-1). The effect of protraction by exposure to caesium-137 (^{137}Cs) γ-rays of exponentially decreasing dose rate has been studied *in vitro* in the context of the Lea-Catcheside model (*45*,*46*). However, parameters inferred from EBRT do not account for potentially differing intrinsic radiosensitivity of cells to the clinically-relevant ^{90}Y β^- emissions (*47*). To address this shortcoming, Gholami et al. compared ^{90}Y to 6 MV photons from a LINAC using a colorimetric cell viability assay (MTS) (*46*). Their findings suggested that ≈56 Gy of ^{90}Y exposure over 8 days is radiobiologically as effective as ≈8 Gy from a single fraction of acute LINAC exposure.

Table 1.3-1 Summary of LQ and radiobiologically-relevant modelling parameters applied to ^{90}Y SIRT in the literature. The origin of each parameter used is referenced in brackets.

Paper	Tissue	α/β (Gy)	α (Gy^{-1})	β (Gy^{-2})	T_{rep} (h)	T_{phys} (h)	G_∞
Tumour							
(*38*)	Tumour	10	-	-	1.5	64.2	0.02283
(*48*)	Neuroendocrine tumours	2.6 (*49*)	-	-	2.8 (*49*)	64.2	0.04179
(*50*)	Tumour	10 (*20*,*51*)	0.3 (*51*)		1.5 (*34*)	64.2	
(*52*)		2-10	0.01-0.40		1 to 5		
(*20*)	HCC Tumour	10 (*34*)	0.001 and 0.005	0.0001 and 0.0005	1.5 (*53*)	64.2	0.02283
(*54*)	*In vivo* clinical conformal EBRT data for primary HCC and ICC	15.0	0.01	0.00066	-	-	-
(*34*)	Tumour	10	-	-	1.5	64	0.0229
(*55*)	Tumour exposed to IMRT	3 and 10	0.27-0.43				
(*56*)	Tumour	10	0.56	0.056	1.5	64.8	
(*57*)	Tumour	3, 5, 10 (*58*)	0.1, 0.35, 0.5	0.01-0.167	1.5		
(*59*)	Radiosensitive tumour	10	0.56	0.056	1.5	64.8	
(*60*)	HT29 and ^{137}Cs	4.9	0.205	0.041			
Normal Tissue							
(*32*)	Normal Liver from EBRT	2.5 (*53*)	-	-	2.5 (*20*)	64.2*	0.03777
(*61*)	Normal liver	2.5 (*20*)	-	-	2.5 (*20*)	64.2*	0.03777
(*61*)	Normal liver	2.5	-	-	2.5 (*20*)	64.2*	0.03777
(*20*)	Normal liver	2.5 Assumed by (*34*)	-	-	2.5 (*53*)	64.2	0.03748
(*34*)	Normal liver	2.5 (*53*)	-	-	2.5	64	0.0375
(*53*)	Normal liver	2.5	-	-	-	-	-
(*59*)	Bone Marrow	2.5	1.5	0.6	1.5	64.8	

* Walrand et al. has used before, although not defined in this paper

1.4 Combined external beam radiotherapy and selective internal radiotherapy

Inverse dose planning involves the utilisation of dosimetry from a prior radiotherapy treatment as a base dose for EBRT plans. This may prove advantageous, for example, if a patient who was treated with ^{90}Y SIRT presented with a new lesion on follow-up. However, there remains some uncertainty in the best method for doing this (*62*). An inverse dose planning study for ^{90}Y SIRT patients would ideally improve upon the ^{90}Y dosimetry through topping up undertreated areas with EBRT to produce dose volume histograms (DVH) more favourable than either method alone. The rationale for such an approach is that ^{90}Y results in relatively low dose to normal tissue, whereas EBRT is constrained by

dose to normal tissue. Conversely, ^{90}Y dosimetry is retrospective in nature whereas EBRT is prospective and precisely targeted. In this way, from a dosimetric perspective, one could take advantage of the synergies of each therapy to reliably achieve better tumour control without added toxicity risk (*62*). The consensus has been that ^{90}Y SIRT is better tolerated than EBRT owing to the lower off-target absorbed dose and capacity for damage repair during the protracted exposure period.

Several studies have investigated combinations of EBRT and multi-cycle treatments of RNT. In a patient treated with 18 GBq of iodine-131 metaiodobenzylguanidine (mIBG) therapy for a paraganglioma with a metastasis in the odontoid peg, Bodey et al. demonstrated improvement in the dose distribution of the combined therapy over the individual therapy alone (*63*). Cremonesi et al. investigated the potential of a multi-cycle ^{90}Y SIRT treatment and the combination of RNT with EBRT, concluding that "multi-cycle treatments would allow administering higher activities with increased tumour irradiation and preserved radiation effects on [normal liver]."(*34*,*62*) In this way, there may be opportunities to exploit the prospective targeting accuracy of SABR, with the safety of ^{90}Y SIRT from a dosimetric perspective, i.e. that the combination offers dose distributions suggestive of better patient outcomes.

1.5 Aims

The present work addresses the hypothesis that radiobiological measures can improve ^{90}Y SIRT treatment planning and its combination with EBRT. The radiation response of cells to ^{90}Y was assessed through several aims to inform radiobiological modelling in groups of SIRT patients.

The hypothesis of Chapter 3 was that radiation response of ^{90}Y SIRT differs from that of EBRT. To test this hypothesis, the aim was to assess sets of radiobiological parameters

from the LQ model using the clonogenic assay for CRC cell lines with differing radiosensitivities (DLD-1 and HT-29) among three radiation modalities, ^{137}Cs (0.662 MeV γ-rays, linear energy transfer (LET) = 0.8 keV/μm), clinical LINAC (6 MV x-rays, LET = 0.2 keV/μm), and ^{90}Y (0.933 MeV β^--particles). A further aim was to apply the measured LQ modelling parameters to a BED model which describes the relationship between ^{90}Y and EBRT doses. As such, a final aim was to utilise the BED model description of the change between ^{90}Y and EBRT doses to draw inferences on treatment schemes of EBRT, i.e. equivalent dose by 2 or 10 Gy fractions, and inferences on the radiosensitivity of other cell lines, including normal tissue and an HCC cell line (Hep3B).

The hypothesis addressed in Chapter 4 was that dose to individual CRC tumours from a ^{90}Y SIRT patient cohort was associated with vRECIST and volumetric response. A further aim was to apply the BED model derived in Chapter 3 to the absorbed ^{90}Y SIRT dose and assess the clinical implications of including radiobiologically-informed dosimetry analysis. A final aim was to test the hypothesis that perfusion imaging (DCE MRI or pCT) metrics from this cohort was associated with ^{90}Y SIRT dose deposition and response in individual tumours.

The goal of Chapter 5 was to provide the basis for a future clinical trial investigating the combination of ^{90}Y SIRT and subsequent SABR for curative intent. To address this goal, the aim was to apply radiobiological modelling from Chapter 3 to a retrospective cohort that received both ^{90}Y SIRT and EBRT treatments. An additional aim was to generate SABR plans informed by radiobiology in terms of equivalent dose to test the hypothesis that ^{90}Y SIRT followed by SABR, as informed by radiobiological modelling, will reduce doses to normal liver and organs at risk, while increasing doses to treatment targets.

2 Materials and Methods

To assess radiosensitivity of various cancers, several studies were undertaken *in vitro* from colony formation assays and in the clinical setting through the assessment of dose-response in cohorts of ^{90}Y SIRT patients.

2.1 *In vitro* studies

2.1.1 Cell culture

Two CRC cell lines (DLD-1 and HT-29) and one HCC cell line (Hep3B) were obtained from Dr Rebecca Carter (Department of Oncology, Oxford University). During their use, the cells were authenticated by American Type Culture Collection (ATCC, Manassas, Virginia, USA; references STRA4981, STRA7500, STRA9037) and regularly tested for mycoplasma contamination. The cells were cultured in Dulbecco's modified Eagle's medium (DMEM, Gibco, Thermo Fisher Scientific, Paisley, UK) supplemented with foetal calf serum (Merck, UK) at 10% by volume for DLD-1 and HT-29 and 15% for Hep3B. Additionally, DMEM was supplemented with penicillin-streptomycin-glutamine solution at 100 units mL^{-1}, 100 μg mL^{-1}, and 0.29 mg mL^{-1}, respectively (PSG; Gibco, Thermo Fisher Scientific, UK). Cells were incubated at 37 °C in 5% CO_2.

2.1.2 Clonogenic assays

Irradiated cells formed colonies in triplicate in Greiner® 6-well plates for 7 days (DLD-1) or 9 days (HT-29 and Hep3B), unless stated otherwise. Cell plating aimed to achieve a large and equivalent number of colonies (≈200) in each well (or dish) independent of absorbed dose to minimise experimental uncertainties. Colonies were fixed and stained with methylene blue in 50% ethanol. As defined, colonies comprised of ≥50 cells were counted using, unless stated otherwise, an automated colony counter (GelCount™, Oxford

Optronix Ltd, Abingdon, UK). All experiments with DLD-1 and HT-29 were performed in three biological repeats and experiments with Hep3B were completed in two biological repeats (Figure 2.1-1).

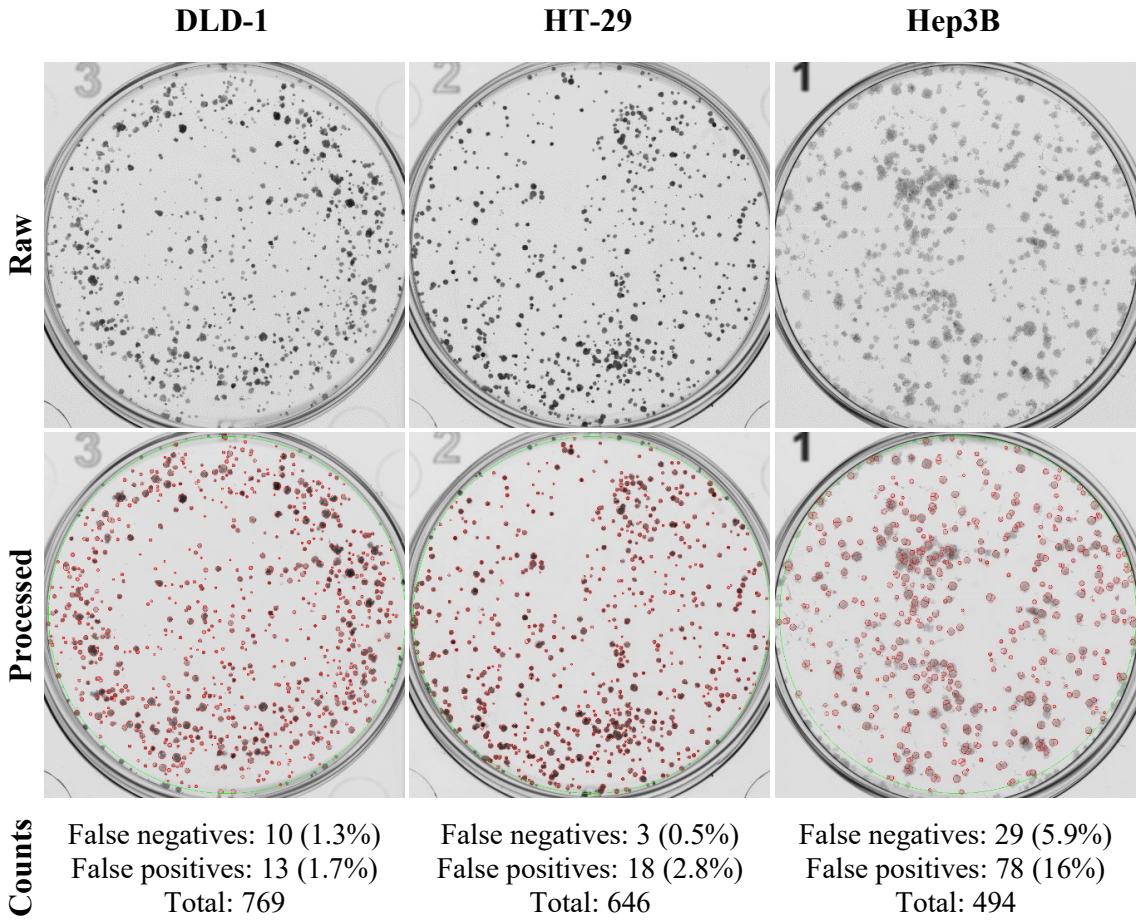

Figure 2.1-1 Example colony formation of cell lines used. The processed row illustrates the colonies identified (red) and counted within the dish boundary (green) using the GelCount™ automated colony counter. The false count rates from the DLD-1 and HT-29 cell lines for the optimised control dish were superior (<5%) to those rates for the Hep3B cell line (>5%).

2.1.2.1 Yttrium-90 β^- particles

2.1.2.1.1 Yttrium-90 radiopharmaceuticals

To irradiate the cells, ^{90}Y was added to a separate dish (referred to as 'Source') either as ^{90}Y-DOTA-TATE or yttrium-90 chloride ($^{90}YCl_3$). ^{90}Y-DOTA-TATE was provided from residual post-therapy aliquots by the radiopharmacy at the Churchill Hospital, Oxford at ≈0.05 MBq μL^{-1}. $^{90}YCl_3$ was purchased from Perkin Elmer (Massachusetts, USA) at ≈10 MBq μL^{-1}. Either of the formulations was applied to the Source dish subject to availability; $^{90}YCl_3$ only was used in experiments with Hep3B.

2.1.2.1.2 Experimental apparatus (ClonogenCity)

To simulate a source not internalised by cells as occurs in ^{90}Y SIRT treatments, an Perspex-shielded experimental box 'ClonogenCity' was designed to house stacks of dishes under ^{90}Y irradiation for clonogenic experiments. The Oxford University Department of Oncology Mechanical Workshop drafted and constructed three that were used in the experiments (Figure 2.1-2). Part of the design included movable posts to stabilise the stack and to accommodate variable sized dishes. The posts offered an advantage when dishes containing cells had to be changed to ibidi® µ-Dish (35 mm, low) due to edge effects (as detailed in Section 3.1.1 on page 45). In addition, a removable divider separating the four stacks allowed for shielding of beta radiation to prevent dose from each stack to enter neighbouring stacks. Optionally, the centre divider could be removed to accommodate dishes of large diameters (>90 mm).

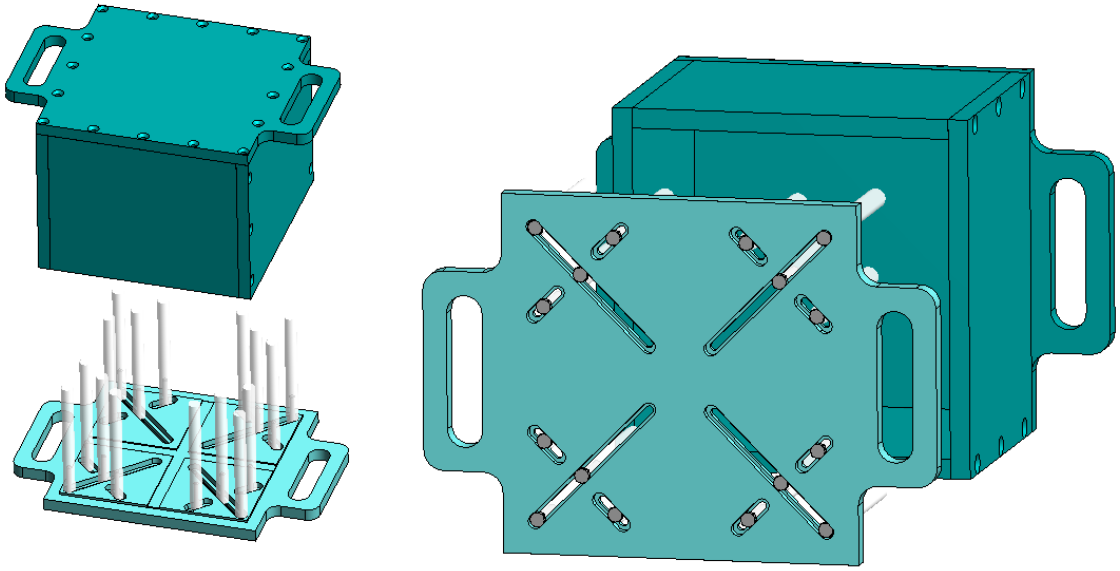

Figure 2.1-2 'ClonogenCity' container fabricated for use in cell experiments with ^{90}Y. All supporting posts (white, 10 mm diameter) were secured with threaded nylon screws of similar density. All walls (turquoise) were constructed from 10 mm Perspex sheets achieved complete shielding (total absorption of betas is achieved at 9.2 mm of plastic).(*64*) The removable divider separating each stack is not shown, but can be seen in Figure 2.1-4. Adapted from Lee et al. 2019.

Additional radiation protection procedures were in place to measure and minimise radiation dose received by the researcher using the apparatus. These included dose meters, a pipette shield (10 mm Perspex), and custom shielded tongs for loading of the ClonogenCity box (Figure 2.1-3).

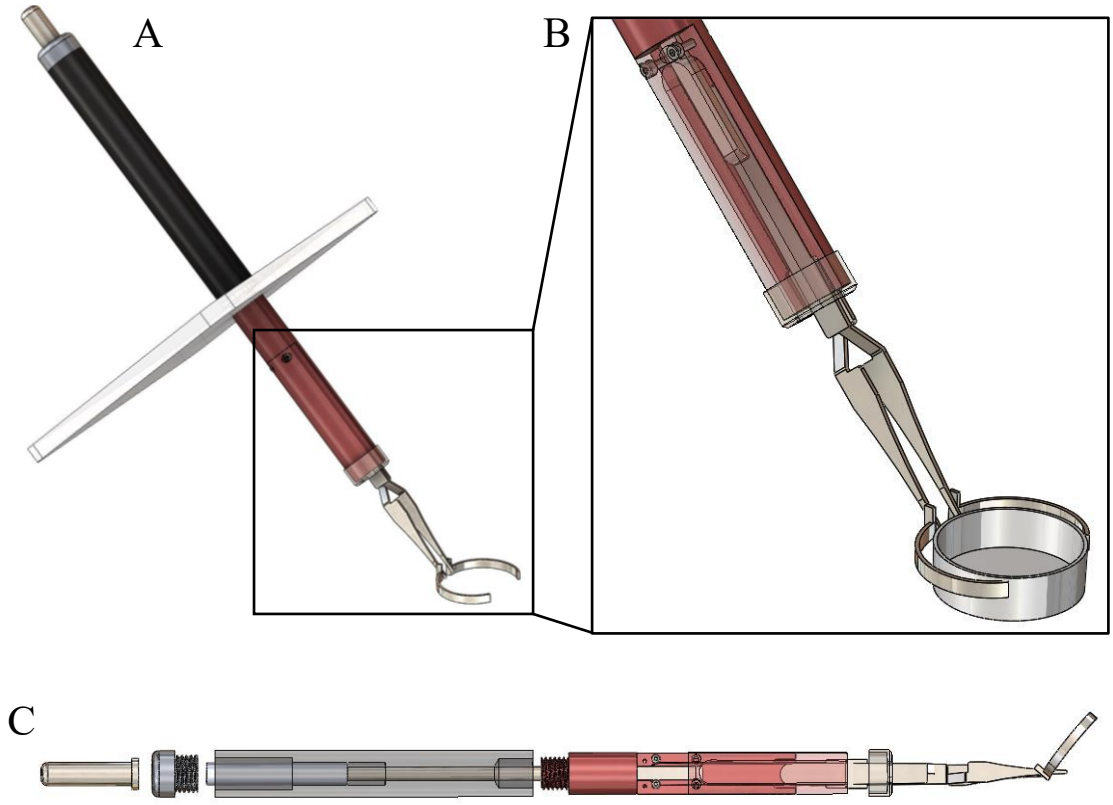

Figure 2.1-3 Additional radiation protection for use in handling ClonogenCity. (A) Custom dish tongs designed for radiation protection by distance and shielding (8 mm Perspex) for removal and placement of dishes in the presence of open ^{90}Y sources accompanying ClonogenCity experiments. (B) An expanded view illustrates the tips of the tongs were reverse-action tweezers modified with curved metal soldered to the end to enhance traction on the dishes. (C) The shaft assembly consisted of a plunger and metal sheath which actuated the tweezers.

2.1.2.1.3 Experimental setup

Adapted from the method by Howell et al. (*65*), cell culture dishes were stacked (Figure 2.1-4A) to avoid direct contact between radioactivity and cells and, therefore, cellular internalisation of ^{90}Y (as this is not the mechanism of action for ^{90}Y SIRT). This setup also allowed concurrent irradiation of cells at multiple cumulative doses. Some limitations of this setup include the millimetres of equivalent distance in tissue between the source and

exposed cells whereas an ^{90}Y microsphere, while not internalised into the cell, may be as near as tens of μm immediately adjacent to a tumour cell. In addition, while simulations (Figure 3.1-2) suggest that the energy spectrum of ^{90}Y beta emissions remains proportional across each of the dishes, this was extrapolated assumption for cells separated from the ^{90}Y source by only tens of μm. Nevertheless, this arrangement was successful at modelling dose deposited across several millimetres, which is especially reasonable for commonly observed tumours with preferential rim ^{90}Y distribution, if not also for other macroscopic clinically detectable tumours. ^{90}Y radiopharmaceuticals were diluted from stock with phosphate buffered saline (PBS, for HT-29 and DLD-1 experiments) or deionised water (H_2O, for Hep3B experiments) and loaded centrally in each stack in a standard Greiner® 35 mm cell culture dish labelled as 'Source'. Each stack consisted of ibidi® low 35 mm μ-dishes labelled as 'Control', '+2', '+1', '-1', and '-2' for cell plating within the central recess of their bases, i.e. onto the polymer coverslip, in 1.5 mL of culture medium. An empty Greiner® 35 mm dish labelled as 'Spacer' was placed immediately above the source dish to achieve the desired doses in dish '+1' and '+2' cells. Additionally, the 'Control' dish in the stack was placed away from the ^{90}Y immediately after a dish labelled as 'Shield' to shield the control dish. For DLD-1 and HT-29 experiments, the 'Shield' in each stack was a Greiner® 35 mm dish filled with 4.0 mL of PBS and placed above the '+2' dish. For Hep3B experiments, in each stack: '+2' was excluded to simplify assembly so that only the 'Spacer' and '+1' dishes were above the source; 'Shield' was placed below '-2' in an ibidi® low 35 mm μ-dish for improved stability; and PBS was replaced by a custom water equivalent plastic insert of fixed geometry to mitigate the possibility of evaporation. The use of the different dish types for cells versus ^{90}Y minimised differences between doses at the centre and edge of the cell growth area to achieve a nearly uniform radial dose distribution among the irradiated cells (Figure 3.1-4 on page 53).

The stacks were assembled with 10, 15, or 20 MBq of ^{90}Y inside Source dishes within three sets of supporting posts of a ClonogenCity (Figure 2.1-4B) and placed inside an incubator. Additional ibidi® control dishes were placed in the fourth set of supporting posts in the ClonogenCity and outside the ClonogenCity inside an incubator.

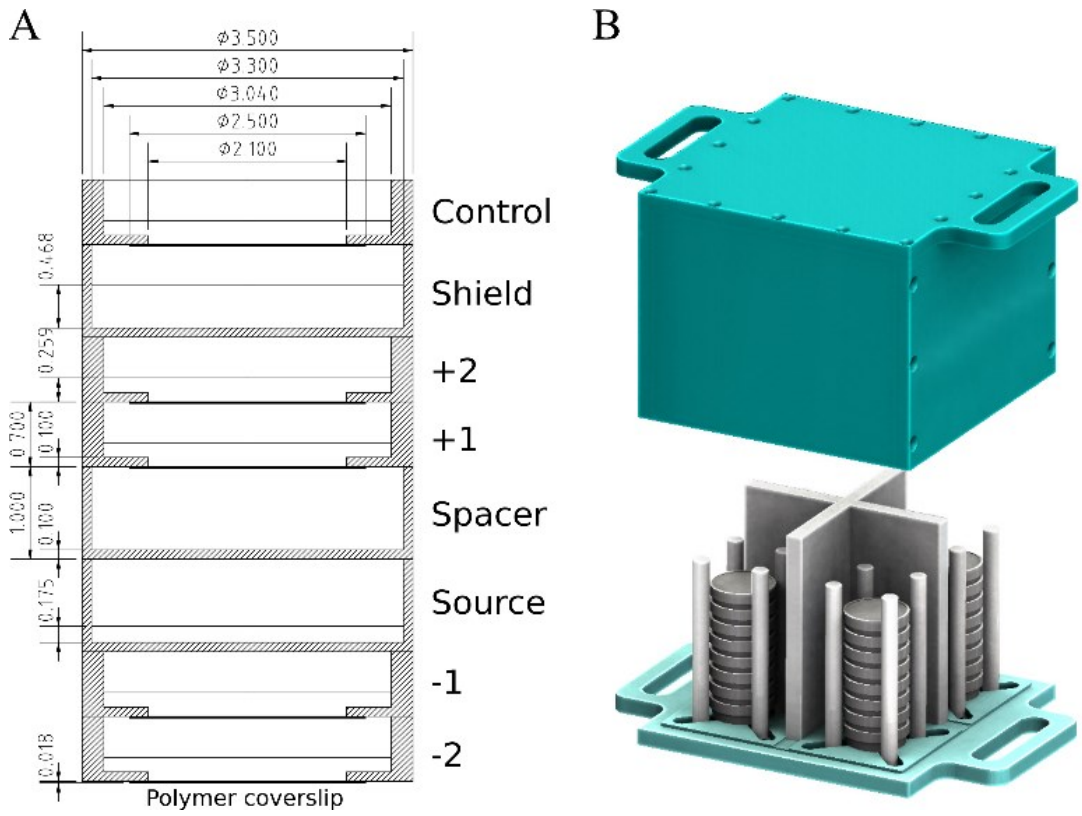

Figure 2.1-4 Schematic of ^{90}Y experimental setup (A) Stack of cell culture dishes as used in the irradiation of DLD-1 and HT-29 cells with externalised ^{90}Y radiopharmaceuticals. All dimensions are shown in cm. (B) Stacks loaded in ClonogenCity for placement in incubator. For a detailed description of ClonogenCity schematic, see Figure 2.1-2 on page 19. Adapted from Lee et al. 2019.

For experiments with DLD-1 and HT-29 (Figure 2.1-5), cells were plated at 4,000-20,000 cells per dish, exposed to ^{90}Y irradiation for 6 days, and then replated in triplicate in Greiner® 6-well plates at 3,000-5,000 cells per well. The radiation absorbed doses

delivered ranged from 0-32 Gy. Radiation dose was delivered at variable average dose rates ranging from 0-0.0037 Gy min^{-1}.

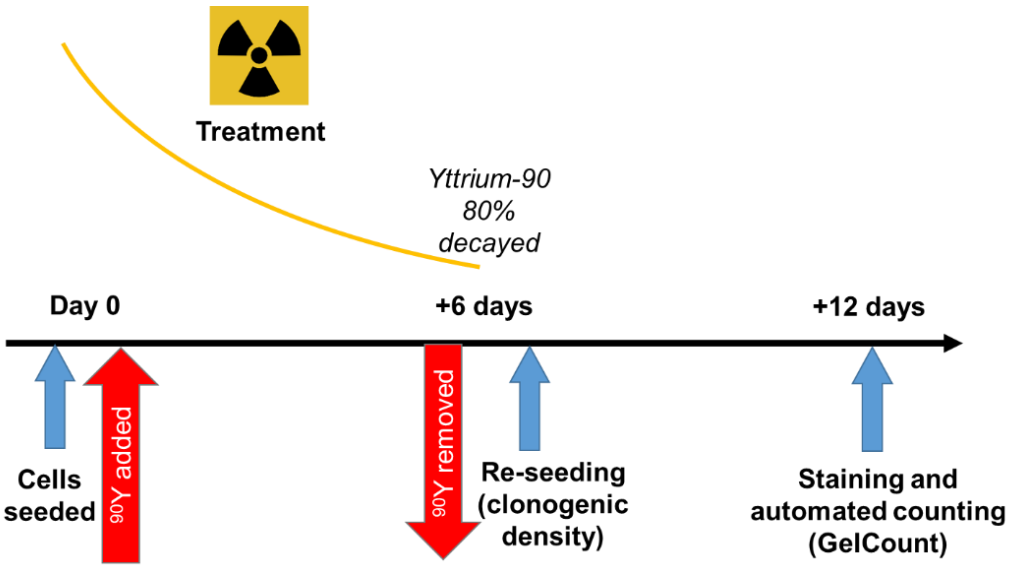

Figure 2.1-5 Clonogenic assay timeline for DLD-1 and HT-29 cells.

For experiments with Hep3B (Figure 2.1-6), three ClonogenCity boxes with triplicate stacks of cells were plated at 600-40,000 cells per well and allowed to form colonies during an 8-day exposure period. The cumulated doses delivered ranged from 0-32 Gy. Radiation dose was delivered at variable average dose rates ranging from 0–0.0028 Gy min^{-1}.

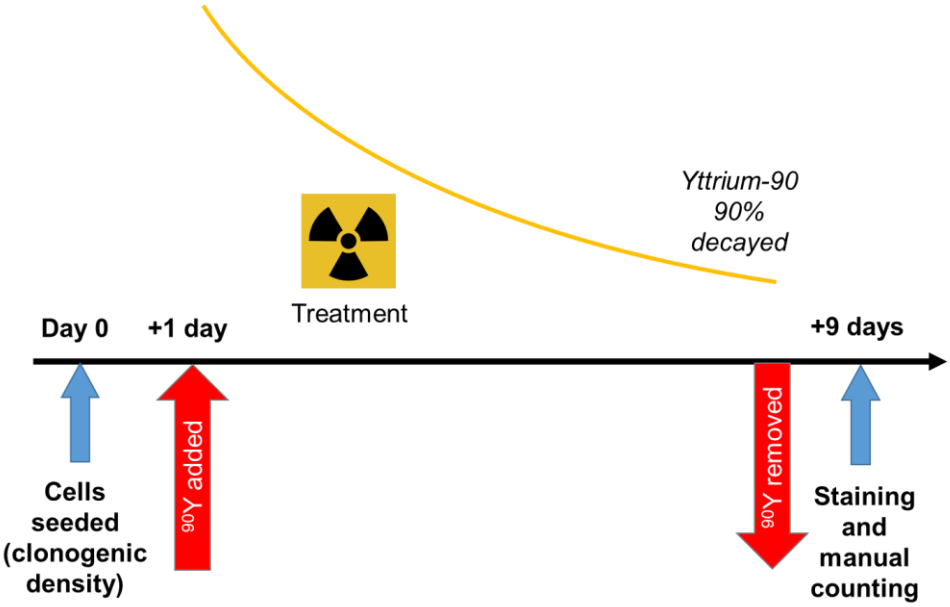

Figure 2.1-6 Clonogenic assay timeline for Hep3B cells.

Gholami et al found insignificant cell kill from exposure to ^{90}Y at a dose rate of 0.013–0.13 Gy h^{-1} compared to a higher dose rate of 0.077–0.77 Gy h^{-1}. If consistent with the Gholami et al findings, cell kill was expected since the methods here utilised dose rates of up to 0.222 Gy h^{-1} for DLD-1 and HT-29 or 0.168 Gy h^{-1} for Hep3B.

2.1.2.1.4 Monte Carlo modelling

The absorbed dose per ^{90}Y decay, known as the *S*-value (Gy MBq^{-1} d^{-1}), was calculated by the Monte Carlo (MC) method *in silico* using the PENELOPE-2014 code (package NEA-1525/022) (*66*) by simulating the energy deposition of ^{90}Y emissions in the stack geometry (Figure 2.1-4). The stack geometry included a cylindrical volume filling the base of each ibidi® dish to estimate absorbed dose to a cell monolayer. This simulated monolayer assumed a composition equivalent to water density (ρ = 1.0 g cm^{-3}) and a height of 15 µm as measured by confocal microscopy (see Table 3.1-3 on page 50). The cell culture medium, ^{90}Y, and PBS were assumed to be equivalent to water. Both Greiner® and ibidi® dishes were assumed to have the composition of polystyrene (ρ = 1.06 g cm^{-3}). The air

inside each dish was assumed to be at standard incubator conditions of 95% humidity and 5% CO_2 at 37 °C ($\rho = 1.276\times10^{-3}$ g cm^{-3}).

The beta and photon emission spectra of ^{90}Y (Figure 1.1-1 on page 3) from the medical internal radiation dose (MIRD) tabulation (*5*) were applied to each simulation using a total of 10^8 primaries. All primaries and secondaries were deposited locally when their energies reached <1 keV.

Media volumes were measured at the beginning and at the end of the exposure period. Since up to a third of the initial medium volume in each dish had evaporated, separate *S*-values were determined at the beginning ($S_{initial}$) and end (S_{final}) of the exposure period. All *S*-values in between $S_{initial}$ and S_{final} were interpolated linearly (see Figure 3.1-3 on page 52). The MIRD formulation (*67*) was applied to account for the evaporation effect in each dish and the final equation used for dose calculation (derived in 8.2.2 on page 162) is

$$D(T) = \frac{A_0}{\lambda}\left[\frac{S_{final} - S_{initial}}{\lambda T}\left(1 - (1+\lambda T)e^{-\lambda T}\right) + S_{initial}\left(1 - e^{-\lambda T}\right)\right]$$

where $D(T)$ is the radiation absorbed dose to cells exposed for duration T, with an initial ^{90}Y activity of A_0, a physical decay constant ($\lambda = \ln 2/T_{phys}$), and ^{90}Y physical half-life T_{phys} = 64.1 h.

2.1.2.1.5 Dose calibration and validation

To validate that MC-derived *S*-values matched the true ^{90}Y dose deposition, several calibration experiments were performed. Radiochromic films, which change in optical density upon exposure to ionising radiation, were cut into 8.2×9.7 mm rectangles from sheets of GAFchromic™ EBT3 film (Ashland Inc., Covington, Kentucky, USA) to fit centrally in the dishes normally containing cells (illustrated in Figure 3.1-5 on page 54). EBT3 was chosen due to its in-house availability and support for calibration of in vitro experiments.

To match the experimental exposure conditions, the films themselves were exposed to LINAC 6 MV x-rays to generate a calibration curve relating the optical density of the film to absorbed doses ranging from 0-10 Gy according to the AAPM TG-61 protocol (*68*) to inform the dose achieved from exposure to ^{90}Y (*46*).

The films were exposed to ^{90}Y *in situ* for 14-19 hours, but not submerged in medium due to the solubility of the films. Experiments were performed in duplicate for both ^{90}Y-DOTA-TATE and $^{90}YCl_3$. The films were scanned using an Epson Expression 10000 XL colour scanner in transmission mode 24 hours after being removed from irradiation conditions. Absolute doses were determined after subtracting the 'Control' dish measured doses from the cell-containing dish doses.

Using a modified geometry to reflect the dry conditions and the presence of films, absolute dose measurements were predicted using MC simulations as described above (Figure 3.1-5 on page 54). The material composition and density of the film was based on previously reported values (*69*).

2.1.2.2 Caesium-137 γ-rays

Cells were plated at 1,000-40,000 cells per well and allowed to adhere for ≈4 hours prior to the treatment delivery. A caesium-137 (^{137}Cs) irradiator (IBL637, CIS Bio international, France) previously calibrated using EBT3 film delivered 0.6 MV photons at 0.77 Gy min^{-1} with doses ranging from 0-10 Gy. The ^{137}Cs irradiator was calibrated for use with a single shelf and tissue culture plate centred in the exposure chamber. Using the equation $A/A_0 = e^{-\lambda T}$, the calibration was decay-corrected by a factor of 0.954 to account for the two years (T=2 years) which had elapsed since the ^{137}Cs source (T_{phys} = 30.09 years, $\lambda = 0.02304\ y^{-1}$) was originally calibrated.

2.1.2.3 Linear accelerator x-rays

Cells were plated at 1,000-10,000 cells per well and allowed to adhere for ≈4 hour prior to the treatment delivery. A Varian LINAC Clinac 2100 series delivered 6 MV photons at 6.6 Gy min^{-1} with doses ranging from 0-10 Gy. The LINAC was regularly maintained and calibrated for clinical use. The gantry using a 15×15 cm^2 field size was positioned at 180° so that the beam passed through the couch from underneath, followed by 1.5 cm of solid water to accommodate for the build-up effect so that the dose maximum was at the cell level, and finally 2 cm of solid water to absorb the backscatter dose.

2.1.3 Statistical analysis

A statistical regression based on the LQ model was used as it is widely applied in the clinic. The LQ model describes the surviving fraction of cells (SF) as a function of absorbed dose (D) by the equation $-\ln SF = \alpha D + \beta D^2$. The α term, directly proportional to dose, indicates lethal damage whereas the β term, proportional to dose squared, indicates sublethal damage. The R software package (version 3.3.3, R Core Team (2017)) and package `nlme` (Pinheiro et al. 2017) were used for statistical analysis. The α and β terms were estimated, separately for each cell line, by fitting a linear mixed-effects model using restricted maximum likelihood. To consider any dependence between replicates, a random intercept term was also included. Standard errors for each term were produced from the regression analysis and propagated to determine the error for α/β as derived in Section 8.5.1 on page 173. To assess whether the estimated α and β were significantly different from zero, Wald tests were used. The threshold for statistical significance was defined as $p < 0.05$.

2.2 Radiobiological modelling

To account for radiobiological phenomena such as damage repair half-time, models extended from the LQ equation were applied to several scenarios. These scenarios included corrections to absorbed dose accounting for cellular radiosensitivity and generation of isoeffect curves. The α and β parameters were taken from the output of statistical regression from Section 2.1.3 above and their errors propagated according to Section 8.5 on page 173 to account for statistical uncertainty.

2.2.1 Biological effective dose

Absorbed doses from various exposure conditions were adjusted for their biological effectiveness using the biological effective dose (BED) concept (*70*). Based on the LQ model, BED is given with the following relationship using LINAC as the reference radiation of choice,

$$BED = \frac{-\ln SF}{\alpha_{LINAC}}$$

$$= \frac{\alpha D + \beta D^2}{\alpha_{LINAC}}$$

where α and β are generic LQ model parameters for a specific tissue and α_{LINAC} is the α parameter when exposed to LINAC x-rays.

For various fractionation schedules of EBRT delivered by LINAC, this relationship can be reduced to the following by substituting in LINAC-specific fit parameters for n fractions of d Gy per fraction (see section 8.3.1 on page 163 for derivation).

$$BED = D\left(1 + \frac{D/n}{(\alpha/\beta)}\right)$$

Likewise, for ^{90}Y SIRT, this relationship may be given by application of the LQ model parameters for exposure to ^{90}Y.

$$BED = \frac{\alpha_{90Y} D + \beta_{90Y} D^2}{\alpha_{LINAC}}$$

2.2.1.1 Variation of parameters by treatment modality

Further radiobiology concepts are necessary to explain the differences between LQ model fit parameters of ^{90}Y and of LINAC. The protraction of dose delivery for ^{90}Y reduces the effectiveness by allowing damage repair to occur during the irradiation period. This phenomenon is accounted for by the Lea-Catcheside protraction factor, G (*71*). Additionally, differences in LET between ^{90}Y and LINAC may result in differing relative biological effectiveness (RBE). Collectively, these concepts can be applied to estimate the treatment effect for ^{90}Y SIRT based on existing knowledge from the better-characterised EBRT treatment effect. The following modified BED equation can be applied for ^{90}Y SIRT exposure (*72*),

$$BED = D_{90Y}\left(RBE_{max} + \frac{G_\infty \cdot D_{90Y}}{(\alpha/\beta)_{LINAC}}\right)$$

where D_{90Y} is the absorbed dose from ^{90}Y SIRT irradiation, the relative biological effectiveness (RBE) at zero dose is $RBE_{max} = \alpha_{90Y}/\alpha_{LINAC}$, and $G_\infty = \beta_{90Y}/\beta_{LINAC}$ is the Lea-Catcheside protraction factor for a fully decayed source (see equation (4) in section 8.3.1 on page 163). G_∞ can be estimated (see derivation in Section 8.4.1.2 below) as

$$G_\infty = \frac{T_{rep}}{T_{rep} + T_{phys}} \qquad \textbf{(1)}$$

for a source with half-life T_{phys} and for tissue with a damage repair half-time T_{rep}.

This modified BED approach assumes that the intrinsic sublethal damage component for ^{90}Y SIRT and LINAC are equivalent and that the quadratic component of the LQ model as modified by the Lea-Catcheside factor (i.e. $G\beta$) can explain variation due to dose rate

effects. As such, for LINAC, $G = 1$ (see Section 8.4.1.1 on page 169 for derivation), while for ^{90}Y SIRT, $G < 1$ supressing the quadratic component of the survival curve.

A further generalised BED model can be applied for both fractionated EBRT and multi-cycle ^{90}Y

$$BED = D\left(RBE_{max} + G_{\infty}\frac{D/n}{(\alpha/\beta)}\right) \quad (2)$$

where n is the number of fractions or cycles. For EBRT, $RBE_{max} = 1$ and $G_{\infty} = 1$.

2.2.1.2 Parameter and model selection

The parameters chosen for clinical application are applied from results of CRC clonogenics assays (Table 3.3-1 on page 63). These are the main values used for patient analysis in Chapter 4. However, Chapter 0 with HCC utilises the simplified parameters from Table 3.3-2 on page 66, owing to the limited standard of evidence from *in vitro* experiments and large relative uncertainties of the fit terms.

For the *in vitro* assay, cells which were exposed to ^{90}Y of a partially decayed source must not adopt the G_{∞} estimation above. For this scenario of a finite exposure for duration T, the general Lea-Catcheside protraction factor (G_T) is described by the full mechanistic explanation outlined in Section 8.4.1 on page 167.

2.2.2 Comparison of effect between treatment modalities

The LQ model may be extended to directly appreciate the differences in biological effect between treatment modalities. However, the parameters must match the context of the delivered radiation. For example, if a radiation source has a low dose rate, then low dose rate effects, such as hypersensitivity and LET, must be captured to allow for direct comparison with the reference radiation source.

2.2.2.1 Relative Biological Effectiveness (RBE) determination

Relative biological effectiveness (RBE) is defined as the proportion of dose necessary to achieve the same effect for a given reference radiation modality (in this case, LINAC).

$$RBE = \frac{D_{LINAC}}{D_{90Y}}$$

RBE can be derived directly from the LQ model and is given by the following equation as derived in Section 8.3.4 on page 166.

$$RBE = \frac{\beta_{90Y}}{\beta_{EBRT}} \cdot \frac{\alpha_{EBRT} - \sqrt{{\alpha_{EBRT}}^2 - 4\beta_{EBRT} \ln SF}}{\alpha_{90Y} - \sqrt{{\alpha_{90Y}}^2 - 4\beta_{90Y} \ln SF}}$$

While this equation assumes fixed values for α and β, this may not be true if LET changes as the source decays.

2.2.2.2 Equivalent Dose (EQD)

To describe the equivalence (or isoeffect) between ^{90}Y SIRT and fractionated EBRT regimens, the general concept of equivalent dose (EQD) to fractionated EBRT may be used (*73*). EQD is given by the following equation (see Section 8.3.3 on page 1658.3.3 below for derivation), which is also adapted from the LQ model.

$$EQD = \frac{BED}{1 + \frac{d}{(\alpha/\beta)_{LINAC}}}$$

The EQD concept can be derived from individual fit parameters.

2.2.3 Clinical endpoints

The radiobiological modelling above is useful for conceptualising the variation of effects between ^{90}Y SIRT and EBRT but falls short of describing an application of the LQ model in terms of treatment planning.

2.2.3.1 Equivalent Uniform Dose (EUD)

Target doses for EBRT treatment are given as constraints based on clinical experience using doses prescribed to a uniform treatment volume. For example, treatment planning may be optimised (across several fractions) to achieve 21 Gy in a liver tumour while limiting normal liver tissue dose to 12 Gy. Treatment planning involves clinical imaging such as CT and since volumes are made from a cluster of voxels, each of which has its own dose value, the volumes are made from a distribution of doses. However, for ^{90}Y SIRT, doses are rarely uniform due to the uptake pattern of the microspheres. As such, there is a clinical mandate for a standard description of the dose distribution in terms of a single value by which any treatment may be administered in terms of equal effect.

Several methods exist to consolidate a dose distribution into a single value to describe effect including the Kutcher and Burman method (*74*) which results in an effective volume and the volume-weighted dose method (*75*) which results in an effective dose, i.e. equivalent uniform dose (EUD). Consistent with both of these methods is the generalised EUD equation (*76*)

$$EUD_a(d) = \left(\frac{1}{n}\sum_{i=1}^{n} {d_i}^a\right)^{1/a}$$

which has the parameter a that accounts for volume dependence, i.e. varies whether an organ is parallel or serial, and the parameter d_i for the dose in each voxel i over all n voxels. A special case of the generalised EUD where $a \to 1$ is effectively the arithmetic mean dose (hereafter referred to as 'average' dose).

2.2.3.2 Equivalent Uniform Biological Effective Dose (EUBED)

Finally, the equivalent uniform biological effective dose (EUBED) method was used to summarise doses based on survival fraction expected in each voxel (SF_i) using LQ model radiosensitivity parameters (*77*),

$$EUBED = -\frac{1}{\alpha}\ln\left(\frac{\sum_i e^{-\alpha \times BED_i}}{n}\right) = -\frac{1}{\alpha}\ln\left(\frac{\sum_i SF_i}{n}\right)$$

where BED_i is the BED at each voxel.

2.3 Clinical studies

2.3.1 Patient selection

Two retrospective studies were conducted of patients with hepatic tumours treated with ^{90}Y resin microspheres (SIR-Spheres®, Sirtex Medical Limited, North Sydney, Australia). All patients had inoperable and chemorefractory tumours. For inclusion in the studies, all patients met the eligibility criteria: >18 years of age, stable liver enzymes, had follow-up imaging, no previous SIRT, no contraindications from angiography, world health organisation (WHO) performance status >2, and no bony metastases. Informed consent was provided by all patients prior to treatment.

2.3.1.1 CRC cohort

In the first clinical study (Chapter 4), 23 patients, referred to hereafter as "the CRC cohort," with primary CRC (96 secondary liver lesions) were treated at the Churchill Hospital (Oxford, UK) between November 2014 and October 2015. Further patient characteristics at baseline are provided in Table 4.1-1 on page 70. Institutional review board (University of Oxford, PID 12277) and Health Research Authority (HRA) ethics (IRAS 214611) approvals were obtained for use of the clinical data for research purposes. Additionally, a

subcohort of ten patients were selected from the PERFORM cohort for analysis of perfusion parameters against dose and volumetric response in Section 0.

2.3.1.2 HCC cohort

In the second clinical study (Chapter 5), 10 patients—referred to hereafter as 'the HCC cohort'—with primary liver cancer were treated with EBRT at the Sarah Cannon Cancer Center (Nashville, USA) between June 2014 and July 2018. Further patient characteristics at baseline are provided in Table 4.1-1 on page 70.

2.3.2 ^{90}Y microsphere treatment

To assess the lung shunt percentage and vascular distribution in the liver, ^{99m}Tc-MAA was injected prior to SIRT. Angiography to map blood flow through the liver was performed under intermittent fluoroscopic visualisation. Blood flow through the liver was redirected using coil embolisation to optimise delivery of the SIRT microspheres. Resin microspheres loaded with ^{90}Y were injected into the liver using a catheter guided through selected branches of the hepatic artery. For the CRC cohort, the ^{90}Y activity, corrected for decay between the time of preparation in the radiopharmacy to the time of administration (range 847-2185 MBq), was determined according to a modified BSA method as used in the FOXFIRE trial (*12*) with activity reductions for patients with a lung shunt >10%. For the HCC cohort, the ^{90}Y administered activity (range 1.546-2.461 GBq) was determined according to the BSA method.

2.3.3 Medical image analysis

2.3.3.1 Acquisition

For the CRC cohort (Figure 2.3-1), baseline triple-phase contrast-enhanced CT images (GE LightSpeed VCT) and T2-weighted fat-saturated magnetic resonance (MR) images

(GE Signa 3T) were acquired 11-48 days prior to SIRT treatment. Repeat CT and MR images were acquired 8-10 weeks after treatment to assess response on follow-up. SPECT and CT hybrid (SPECT/CT) images (GE Discovery D670 dual-headed gamma camera) to visualise deposition of the SIRT treatment microspheres were acquired one day immediately after treatment. The SPECT images were acquired with a dual-headed gamma camera using a 50-150 keV energy window and a medium-energy general-purpose collimator (128×128 matrix, 90 views, 20 seconds per view). The SPECT images were reconstructed using Xeleris (version 3·0, GE Healthcare, Haifa, Israel) with the default ordered subset expectation maximization (OSEM) settings (2 iterations, 10 subsets) and CT attenuation correction. DCE MRI and pCT were acquired at 1 and 3 months following ^{90}Y SIRT.

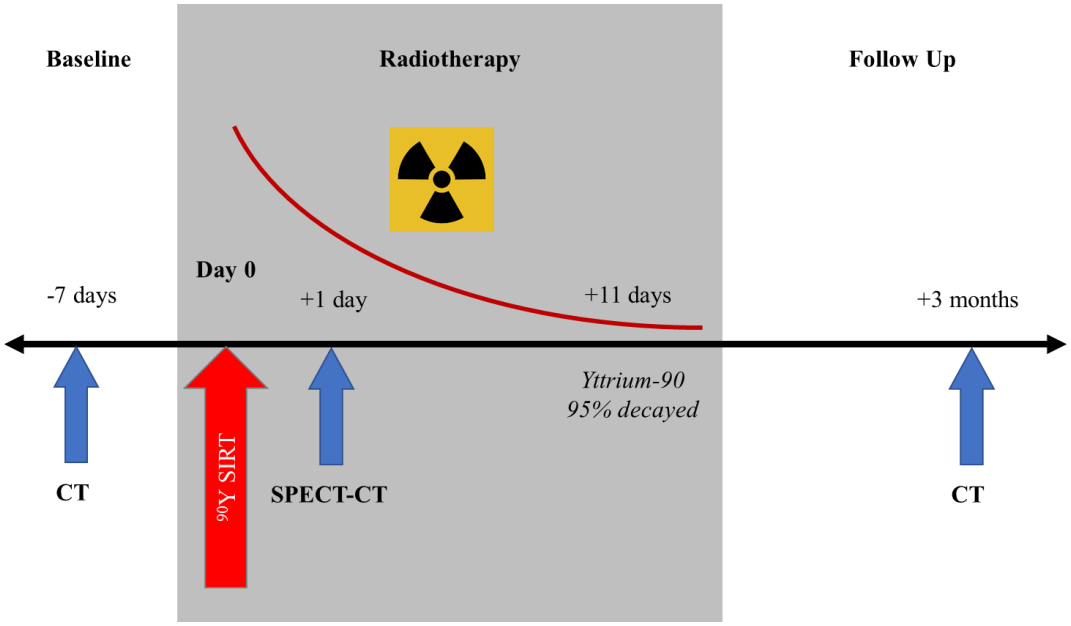

Figure 2.3-1 Treatment timeline for CRC cohort which received ^{90}Y SIRT.

For the HCC cohort (Figure 2.3-2), CT images (Siemens SOMATOM Definition AS, GE Optima CT660, or GE LightSpeed RT16) were acquired at baseline. CT hybrid imaging from either positron emission tomography (PET) (GE Discovery 710) or SPECT (GE

Infinia) was acquired for each patient on the same day as the SIRT treatment. PET and SPECT images were used in the same applications for the subsequent dosimetry analysis. PET images were reconstructed using 3D ordinary Poisson OSEM with time-of-flight, resolution recovery, and an all-pass filter according to the recommended guidelines from the QUEST phantom study (*78*). SPECT imaging was performed with a medium energy low penetration collimator adopting the reconstruction parameters recommended in (*79*) using 2×64 projections obtained over 360°. Following their recommendations, voxelised signal in the background compensation energy window of 310-410 keV was scaled by a factor of 0.53 and subtracted from the imaging energy window of 90-125 keV. Attenuation correction based on CT imaging was performed with a mean energy of 107 keV using a bilinear fit curve. Follow-up images were acquired at 6 weeks, 3 months, and 6 months after treatment. Additional CT imaging was acquired for EBRT treatment planning 3 months before SIRT, and in two cases following SIRT.

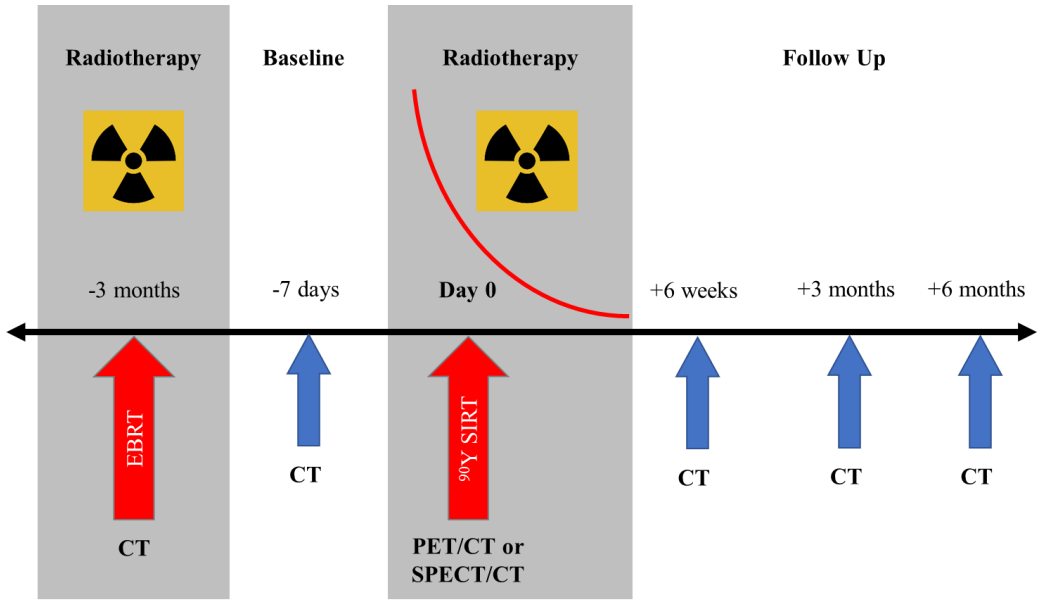

Figure 2.3-2 Treatment timeline for HCC cohort that received ^{90}Y SIRT and EBRT.

2.3.3.2 Coregistration

All patient images were manually registered to the post-SIRT PET/CT or SPECT/CT allowing for translation and rotation in all dimensions, i.e. rigid coregistration. For the CRC cohort, rigid coregistration was performed using HERMES HybridViewer software (version 2·6F, HERMES Medical Solutions AB, Stockholm, Sweden). For the HCC cohort, rigid coregistration and an additional deformable registration method were performed in the MIM platform (version 6.9, MIM Software Inc., Cleveland, USA).[1] The deformable registration allowed for the voxel-wise accumulation of doses from EBRT and ^{90}Y SIRT using a proprietary hybrid of intensity-based and contour-matching algorithms in MIM.

2.3.3.3 Segmentation

To facilitate dose (Section 2.3.4 below) and response (Section 2.3.5 below) measurement, volumes of interest for whole liver and tumour were segmented across all time points. Normal liver segmentation was performed to include voxels which were in the whole liver volume but not in the tumour volume. Segmented contours from the SIRT treatment CT were transferred to the corresponding SPECT or PET image for extraction of data.

For the CRC cohort, the MR images at baseline and follow-up were used to inform segmentation of tumour tissue on the contemporaneous CT images due to their superior soft tissue contrast. Total tumour tissue was contoured in HERMES and individual lesions were separated in a custom script developed in MATLAB® (Mathworks, Natick, Massachusetts, USA). The separation uses the `bwconncomp` function of the MATLAB

[1] MIM was the preferred software for coregistration and segmentation tasks but was only used in the CRC cohort for dosimetry cross-validation. MIM was not used in the coregistration and segmentation analysis of the CRC cohort because the license was only available after the CRC cohort was already fully analysed in HERMES.

Image Processing Toolbox which performs connected-component labelling of distinct regions in a mask image by checking for connectivity to adjacent voxels assuming an 18-connected neighbourhood.

For the HCC cohort, tumour contours were defined using MIM with independent labels rather than separated post-assessment. Additional contours were defined for all ^{90}Y SIRT and EBRT treatment images with associated dosimetry. Organs at risk (OARs) were defined manually in MIM. Tumour contours were cropped to necessarily remain inside the liver contour while OAR contours were cropped to remain outside the liver contour.

All contours from segmentation from coregistered images were validated by oncologist Tessa A. Greenhalgh (Oxford University Hospitals NHS Foundation Trust, Oxford, UK) and radiologist Robert S. Young (Radiology Alliance, Nashville, USA) for the CRC and HCC cohorts respectively.

2.3.4 Dosimetry

2.3.4.1 Colorectal carcinoma cohort ^{90}Y-microsphere dosimetry

For the CRC cohort, ^{90}Y SIRT absorbed dose in each voxel (D_i) was calculated using the local deposition method (LDM), also referred to as the local energy deposition (LED) method, with a known activity

$$D_i = \tilde{A}_i \times S$$

where S is the absorbed dose per unit cumulated activity, i.e. dose per decay, and $\tilde{A}_i$ is the cumulated activity (MBq h), i.e. total number of decays.

The cumulated activity was determined by equating the injected activity (A_0) accumulated for full decay ($\tilde{A}$) to the total counts from each voxel (c_i) of the SPECT (or PET) image within the entire liver volume ($\sum_i c_i$).

$$\tilde{A}_i = \frac{A_0}{\lambda} \frac{c_i}{\sum_i c_i}$$

This assumes that the entire prescribed amount of radiopharmaceutical was injected in the liver, though sometimes radioactivity can remain within the intravenous lines from the syringe, e.g. if not rinsed. In this case, the cumulated activity calculations would overestimate the deposited dose.

Since ^{90}Y remains *in situ* during the SIRT irradiation period, the cumulated activity assumed physical decay only, i.e. no redistribution. As the half-life of ^{90}Y (T_{phys} = 64.1 hours) is significantly longer than the administration time of SIRT (<1 hour), immediate deposition of the microspheres was assumed. The prescribed activity as measured by radiopharmacy staff was corrected for any decay before the ^{90}Y was administered to the patient using the equation $A/A_0 = e^{-\lambda T}$.

The ^{90}Y *S*-value (6.225 Gy MBq^{-1} h^{-1}) was determined by adding integrating the energies from the ^{90}Y emission spectra. The radiation spectra of ^{90}Y (Figure 1.1-1) were acquired from the unabridged decay data in the MIRD-RADTABS software (MIRD tabulation, Ver. 2.2) (*5*). Dosimetry was validated by comparing dose calculations with MIM SurePlan™ LiverY90, demonstrating <5% difference in calculated doses.

According to Figure 4 of the QUEST study, even when using ^{90}Y PET with superior spatial resolution, the activity recovery for ^{90}Y was only 20-40% for a 1 mL sized lesion (*78*). Further degrading the activity recovery, Siman et al identified SPECT recovery of about 25% for a 27 mL sphere at the 2 iterations and 10 subsets OSEM reconstruction settings used here (*79*). While PET-based dosimetry of ^{90}Y is superior, at the time of the study, it was not routine at the Churchill hospital to perform PET/CT following SIRT. Only SPECT was performed for this cohort of patients. This resulted in some limitations for performing dosimetry in small lesions without partial volume correction and scatter correction, which were not included in this cohort. Partial volume effects were addressed by separately analysing tumors >10 mL and <10 mL.

2.3.4.2 Hepatocellular carcinoma cohort ^{90}Y-microsphere dosimetry

For the HCC cohort, the ^{90}Y dose was calculated according to the LDM based on the MIRD Pamphlet No. 17 schema as detailed in the MIM white paper (*80*) by first determining a calibration factor as the total injected activity divided by the total counts in the body contour (hereafter referred to as 'body-based'). An additional dose method (hereafter referred to as 'liver-based') determined a calibration factor as the total injected activity less the percentage outside the liver divided by the total in the liver contour. The ^{90}Y PET or SPECT image was then scaled by the calibration factor and divided by the voxel volume such that the resultant image had units of Bq mL^{-1}. This resultant image was then scaled by the *S*-value of 4.794×10^{-5} Gy Bq^{-1} mL to convert the image to absorbed dose in Gy. Absorbed doses were further validated using the liver-based method (similarly applied in the CRC cohort) in comparison to the default MIM body-based method for HCC.

2.3.4.3 Hepatocellular carcinoma cohort external beam radiotherapy dosimetry

Patients from the HCC cohort received 18-21 Gy EBRT to liver tumours in 6-7 fractions of 3 Gy per fraction (except one patient who received 5 fractions of 10 Gy). Additionally, to achieve inverse dose planning informed by the ^{90}Y SIRT dosimetry, two radiotherapy dose files (RTdose) from MIM were converted into compatible radiotherapy plan files (RTplan) using Velocity (Varian Medical Systems Inc., Palo Alto, California, USA) for inverse dose planning in Eclipse software (Varian Medical Systems Inc., Palo Alto, California, USA). The RTplans from ^{90}Y SIRT treatment were used as 'Base dose' for EBRT optimisation. Each patient was planned to achieve a uniform dose of 50 Gy (5×10 Gy) to the PTV, while sparing 700 mL of unirradiated normal liver.

2.3.4.3.1 Patient Selection

Two hepatocellular carcinoma (HCC) patients were treated with radiotherapy at the Sarah Cannon Cancer Center (Nashville, TN). Both patients received 7 fractions of 3 Gy of palliative EBRT followed by ^{90}Y SIRT. Neither patient was eligible for SABR prior to ^{90}Y SIRT owing to the extent of their disease burden.

2.3.4.3.2 Dosimetry

^{90}Y SIRT dosimetry was performed using a custom workflow in MIM Software. The doses were determined using the total positron emission tomography signal inside the body contour, without lung-shunt correction. To intercompare radiation doses from the different modalities, biological effective dose (BED) was calculated in terms of LINAC using the model $BED = D\left(RBE_{max} + G\frac{D/n}{\alpha/\beta}\right)$ adopted from Lee et al.(*81*) Model parameters are listed in Table 2.3-1 below.

Table 2.3-1 BED modelling parameters.

Parameter (units)	SABR		^{90}Y SIRT		Description
	HCC tumour	***Normal liver***	***HCC tumour***	***Normal liver***	
D (Gy)	variable	variable	variable	variable	*Physical absorbed dose*
RBE_{max} (unitless)	1	1	0.6	0.6	*Relative biological effectiveness to reference radiation*
G (unitless)	1	1	0	0	*Lea-Catcheside protraction factor*
α/β (Gy)	17	3	17	3	*Radiosensitivity*
n (unitless)	variable	variable	1	1	*Number of fractions*

The custom workflow also calculated EQD for variable fractionation schedules using the equation $EQD = \frac{BED}{RE}$, where RE is the relative effect expression for the desired fractionation scheme.

2.3.4.3.3 Treatment planning

^{90}Y SIRT dosimetry was made SABR-compatible through radiobiological conversion to EQD. SABR was planned to treat the tumour uniformly with 5 fractions of 10 Gy. Two groups of radiotherapy planning were assessed to appreciate the value of combined therapy:

Plan I. ^{90}Y SIRT followed by SABR

Plan II. SABR alone

Dose volume histograms (DVH) were plotted from the voxelised data to convert doses from normal liver, targeted tumours, and right kidney—a common OAR—for comparison of the quality of the plans.

2.3.4.4 Dose volume histograms and biological effective dose

The resultant voxelised dose distributions in each tissue were summarised using cumulative dose-volume histograms (DVHs). BEDs and BED histograms (BVHs) were also derived from the calculated absorbed doses according to Section 2.2.1 on page 28. For the HCC cohort, BVHs for the EBRT and ^{90}Y SIRT treatments were summed, and in the process the geometrical distribution within the tumour was neglected. However, to appreciate total absorbed dose, the deformable co-registration of doses (described in Section 2.3.3.2 on page 37) allowed for estimation of voxelised summation of BEDs from each treatment.

2.3.5 Response

Treatment response was assessed based on the relative change in tumour volume from baseline ($V_{baseline}$) compared to volume at follow-up ($V_{followup}$). Tumour volume change was defined as $\left(\frac{V_{followup}}{V_{baseline}} - 1\right) \times 100\%$, such that no change in volume yields 0% and a reduction in volume yields <0%. In addition, vRECIST was used to assess response (*82*). Under vRECIST, complete response (CR) is defined as the radiological disappearance of tumour, partial response (PR) as the reduction in tumour volume by at least 65%, progressive disease (PD) as the increase in tumour volume by at least 73%, and stable disease (SD) as neither PR nor PD (Table 2.3-2).

Table 2.3-2 vRECIST definitions of response

Response	vRECIST Category	Change in Tumour volume
R	CR	-100%
	PR	If CR not met, ≤ -65%
NR	PD	≥ 73%,
	SD	If PR or PD not met

An additional assessment of response was performed for perfusion imaging based on time-resolved models. The pCT data were collected using the CT Perfusion 4D commercial software (GE Medical Systems, Buc, France) and fit to the convolution model, as detailed in the software user manual (*83*). Parameters included blood flow (BF), mean transit time (MTT), blood volume (BV=BF×MTT), and permeability-surface area product (PS). The DCE MRI data were collected from segmentation performed in ITK-SNAP and fitted using an in-house DCE MRI analysis and visualisation software, PkView developed as part of (*84*) and (*85*). DCE MRI was modelled according to the Tofts model (*41*). Parameters included the transfer constant (K^{trans}), fractional volume (v_e) of the

extravascular extracellular space (EES), and the rate constant of backflux from the EES to the blood plasma ($k_{ep}=K^{trans}/v_e$). The mean for each of these parameters was evaluated at baseline. Changes in the mean were evaluated as the difference between baseline and one- or three-months follow-up parameters.

2.3.6 Statistical analysis

Summary dose metrics were calculated for each contour to use as explanatory variables in regression analysis in the R software package (*86*). These summary dose metrics included the mean (arithmetic) and median (50^{th} quantile per cent) as measures of central tendency, standard deviation and relative standard deviation (RSD) as measures of heterogeneity, and D_{70} (30^{th} quantile per cent dose, i.e. minimum dose to 70% of the volume) as a measure of dose predictive of response, reported by (*87*). BED values were also used in the regressions using the same summary dose metrics.

Linear regression was used to estimate the association between individual tumour dose and its relative change in volume. To estimate the relationship between dose and vRECIST response, logistic regression was used. The slopes with intercepts and odds ratios (ORs) were obtained for linear and logistic regressions, respectively, as a measure of the dose-response relationships. All regressions accounted for the fact that multiple tumours could belong to the same patient by fitting using generalised estimating equations. Tumours < 1 mL were excluded as the spatial resolution of bremsstrahlung SPECT was limited. The regressions were also performed for each patient with the tumours grouped by individual patient. The threshold for statistical significance was defined as $p < 0.05$.

3 Radiobiology of ^{90}Y microsphere radiotherapy *in vitro*

The foundation of this thesis is the hypothesis that the underlying radiobiology of ^{90}Y SIRT can help to explain treatment response in patients. This chapter aims to identify the key radiobiological factors to consider when modelling the radiobiological response of tumour cells to ^{90}Y SIRT.

3.1 Experimental setup

3.1.1 Stack design for irradiation

Early trials of the apparatus used a stack composed entirely of standard 35 mm diameter Greiner dishes, but Monte Carlo simulations indicated that there was significant falloff of dose within the centre of the dish resulting in edge doses <50% of the central doses. The final stack design retained a Greiner dish for the source but replaced the cell culture Greiner dishes with ibidi dishes. This substitution allowed cells to grow within the smaller central area to absorb radiation from the source beyond the radius where cells grew and reduced edge doses to within 15% of the central doses (Figure 3.1-1).

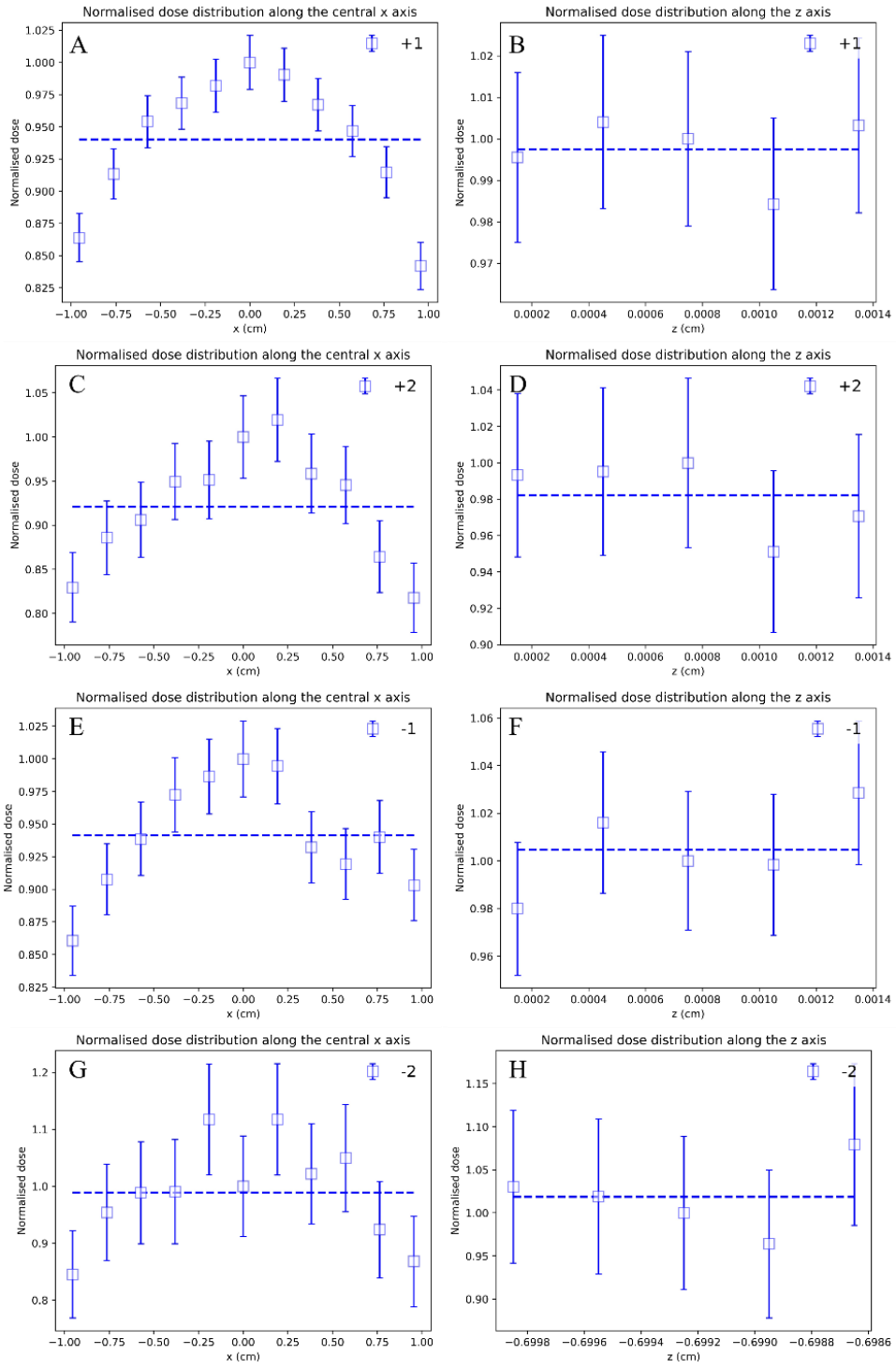

Figure 3.1-1 Quantification of edge effects from PENELOPE simulations. (A, C, E, G) Dose deposition profiles along the diameter indicated that ±1.05 cm from the centre of the ibidi dishes resulted in radial inhomogeneities of <15% dose deposition in the monolayers from each stack position (-2 to +2). (B, D, F, H) Depth dose deposition profiles indicated that

doses absorbed doses did not deviate significantly across the thickness of the monolayer. Adapted from Lee et al. 2019.

Furthermore, the addition of a spacer above the source dish substantially reduced the monolayer absorbed dose per initial activity (≈70% decrease), resulting in +1 and -1 dishes having absorbed radiation dose values within the same order of magnitude (Table 3.1-1). Dishes with more similar dose values were useful for populating survival curves. The even spacing across the range of absorbed doses meant intermediate doses were measured instead of interpolated. Later experiments excluded the +3 and -3 dishes as these required additional experiment burden but did not contribute with much added value as absorbed doses were nearly zero and the control and -2 dishes already measured survival in the low dose range.

Table 3.1-1 Comparison of calculated monolayer dose for the stack geometry with and without a spacer after 6-day exposure per MBq of initial activity.

Dish position	Absorbed dose per initial activity (Gy/MBq)		
	Without spacer	With spacer	Percent difference (%)
+3	0.133	0.0394	-70.4
+2	0.905	0.328	-63.8
+1	4.84	1.54	-68.2
-1	0.695	0.697	+0.3
-2	0.0820	0.0812	-1.0
-3	0.00284	0.00285	+0.4

3.1.2 Monte Carlo dose modelling

The Monte Carlo (MC) modelling resulted in *S*-values which were used as a weighting factor to scale the total accumulated activity (total decays) of the source into absorbed dose

(Gy) for each monolayer according to the stack geometry. The energies deposited from both ^{90}Y radiopharmaceuticals were tracked for each decay (Figure 3.1-2) and integrated according to their probabilities to yield the *S*-values summarised in Table 3.1-2 used for dosimetry purposes. Several effects were revealed that contributed to the complexity of the dosimetry and these are described and considered in the following subsections. Precipitation effects observed in $^{90}YCl_3$ and ^{90}Y-DOTA-TATE meant that the distribution of ^{90}Y varied among the source dishes, so different *S*-values were determined for each.

Table 3.1-2 Initial condition *S*-values for calculating absorbed doses in each cell culture dish. Adapted from Lee et al. 2019.

	$S_{initial}$-value (Gy MBq^{-1} d^{-1})	
Stack position	**$^{90}YCl_3$**	**^{90}Y-DOTA-TATE**
+2	0.0626	0.0840
+1	0.379	0.473
-1	0.314	0.243
-2	0.0301	0.0206

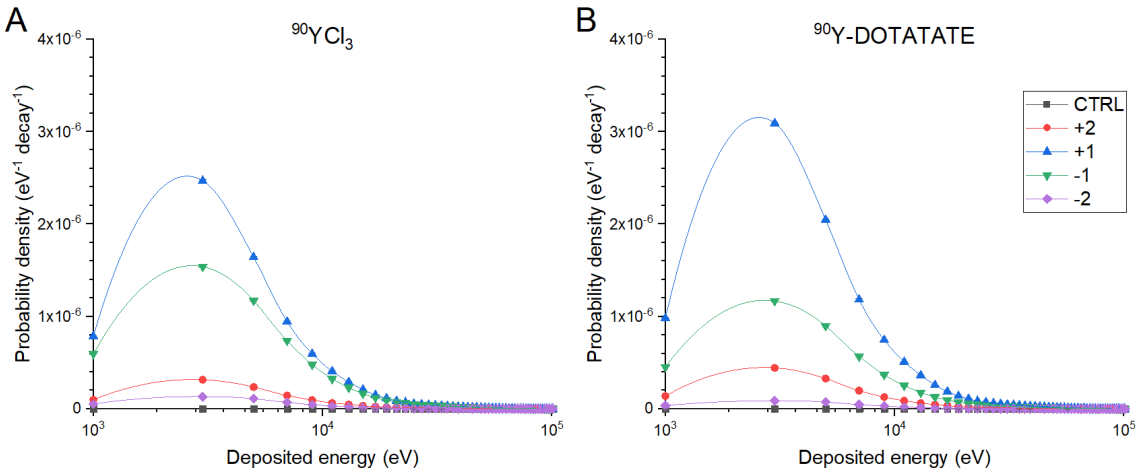

Figure 3.1-2 Spectra at baseline for $^{90}YCl_3$ and ^{90}Y-DOTA-TATE simulations. The spectra revealed proportional energy deposition among the monolayers of each dish. Error bars indicating statistical uncertainty at 3σ were smaller than the symbols. Results between symbols were interpolated with splines.

3.1.2.1 Culture medium depth

For the MC simulation geometry, the surface of the culture medium of each dish did not account for a meniscus. Medium volume was converted to depth measurements based on the cylindrical geometry of the dishes as in Figure 2.1-4A. Some liquid on the culture dish walls was occasionally observed. This was likely due to the handling of the dishes when placed into the ClonogenCity boxes which caused the medium to adhere to the walls and overcome cohesive forces by capillary action.

3.1.2.2 Cell height modelling

For determination of the height of cells in the monolayer, colony dimensions were measured for one cell line (HT-29) by immunostaining and confocal microscopy in Table 3.1-3. Cell height varied with cell area, i.e. packing density.

Table 3.1-3 Colony dimensions for the HT-29 Cell heights were estimated to be between 10-20 µm (15 µm was chosen as the median value). Adapted from Lee et al. 2019.

Sample	**1**	**2**
Cell line	HT29	HT29
Cells plated	10,000	50,000
Colony formation	3 days	3 days
Colony area	13,000 μm^2	17,000 μm^2
Cell count	≈50	≈70
Cell area (area/count)	260 μm^2/cell	240 μm^2/cell
Cell height	16 µm	15 µm
Cell volume (area×height)	4,160 μm^3/cell	3600 μm^3/cell
Image	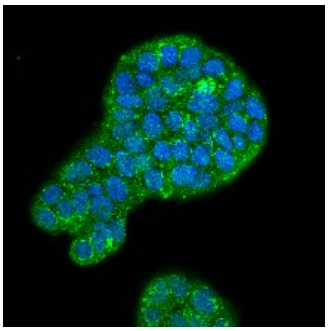	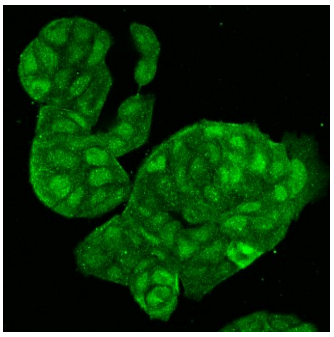
Stain	Actin (green) and DNA (DAPI, blue)	Actin (green) only

The single cell line tested (HT-29) and variation of height with packing density is arguably a limitation of the height determined by MC simulation. However, varying the monolayer height resulted in insignificant changes in the *S*-values, due to the small differences involved, as suggested by Figure 3.1-1B, D, F, and H. Because of these insignificant variations in *S*-values with cell height, these experiments were limited to the single cell line.

3.1.2.3 Evaporation effects

Due to evaporation, the volume of the culture medium added to the cell-containing dishes used within the ClonogenCity setup was found to diminish from the initial 1.5 mL in each dish to vary around 1 mL after 6 days of incubation. It was hypothesised that this reduction in volume would result in an increase in the energy absorbed per ^{90}Y decay due to attenuation of the β particles. Accurate measurement of absorbed dose to the monolayer was critical to enable acquisition of reliable α and β fit parameters of the survival curves. Owing to the difficulties of measuring evaporation rate throughout the experiment, the volume of the culture medium was measured before and after the 6-day exposure. As evaporation effects are known to be linear with constant surface area, this assumption was adopted for cylindrical dishes, and two *S*-values were calculated based on the initial and final culture medium volume. *S*-value as a function of time assumed linear curves for use in dosimetry of the dishes (Figure 3.1-3). The assumed linear *S*-value as a function of exposure time manifests in the equation in Section 0 above for all the dishes.

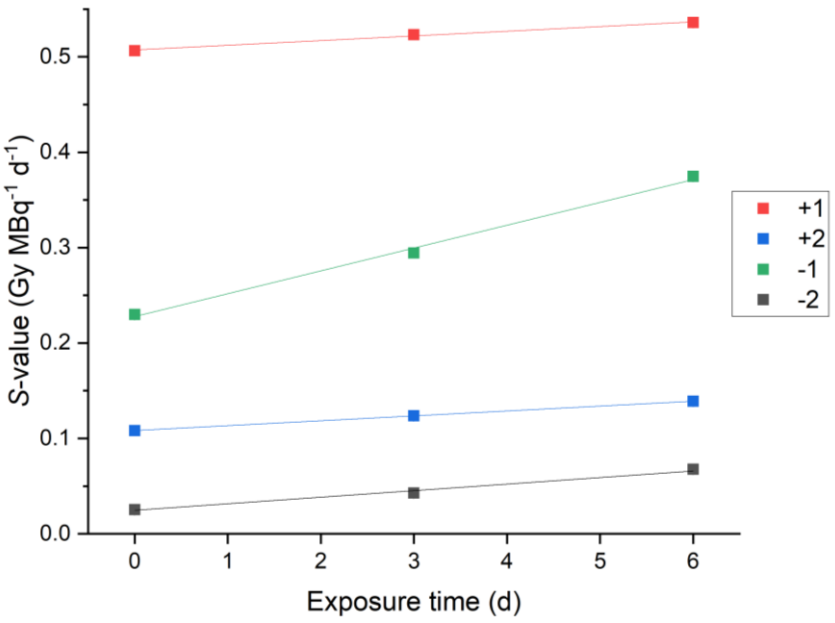

Figure 3.1-3 Example $S(t)$ curves from a single stack of dishes in ClonogenCity. Evaporation modelling assumed that the *S*-values varied linearly with exposure time. The *S*-values at the mid-point of the exposure time (3 days) assumed that half the evaporated medium volume had evaporated and illustrated that geometrical variation maintained linearity in the *S*-values.

3.1.2.4 Edge effects

Ibidi dishes are commonly used in cell imaging due to their ability to decrease edge effects caused by the meniscus of the medium. Using these dishes also helped to minimise edge effects from ^{90}Y radiation, as illustrated by Figure 3.1-4.

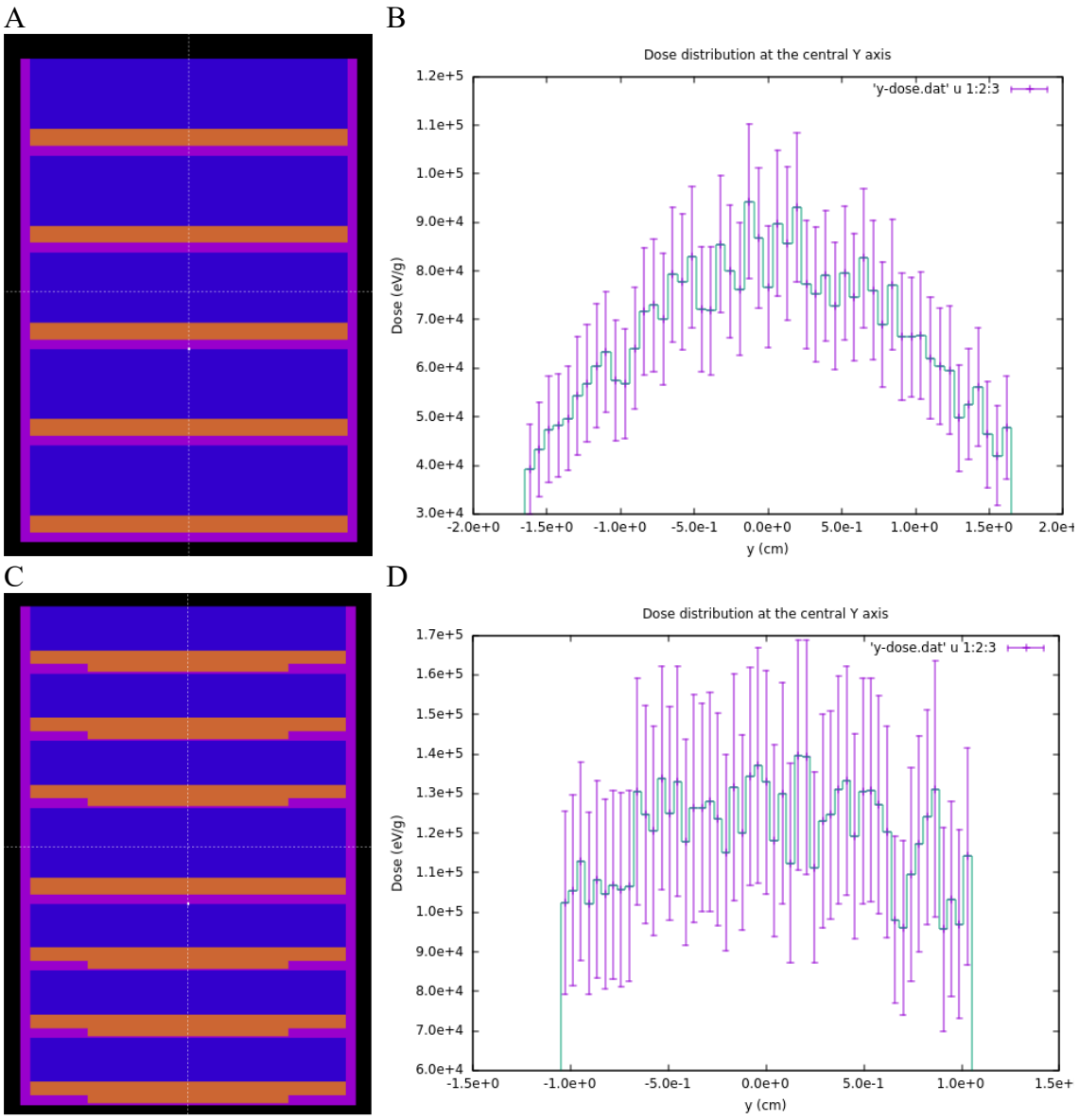

Figure 3.1-4 Dose falloff at the cell dish edge was reduced by changing dish geometry. (A) The original MC geometry (source in middle) with only the standard 35 mm diameter culture dishes by Greiner demonstrated large non-uniformity across the radius of the monolayer according to (B) the MC dose profile for cells in the +1 dish. (C) The MC geometry for cells grown in ibidi dishes illustrated (D) a more homogeneous radial dose distribution profile for cells in +1 dish.

3.1.3 Calibration and validation

Hypothetical ^{90}Y concentration gradients with the source homogeneously distributed in the bottom 25%, 50%, 75%, and 100% were assumed for PENELOPE simulations because

dense microscopic precipitations were observed. The relative doses to cells in each dish from simulation results were compared against doses measured using the EBT3 radiochromic film in the modified stack in dry conditions using $^{90}YCl_3$ and ^{90}Y-DOTA-TATE radiopharmaceuticals (Figure 3.1-5). This comparison demonstrated that dishes above the source were affected differently from dishes below the source. This was presumed to be a function of the dosimetry. Dishes below the source were sensitive to the gradient of the source such that simulation results disagreed with film doses, implying ^{90}Y was concentrated at the bottom 25% and 75% of the source dish for $^{90}YCl_3$ and ^{90}Y-DOTA-TATE, respectively.

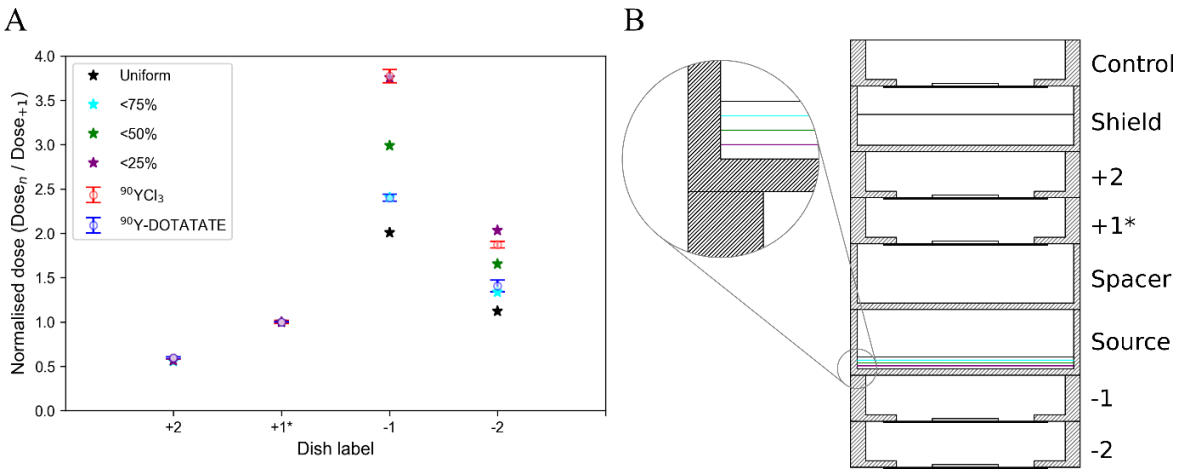

Figure 3.1-5 Validation results comparing relative dose distribution from radiochromic film with MC simulation (A) Doses were normalised relative to stack position +1 (*). Error bars from duplicate experiments represent standard deviation. (B) Stack geometry used for the calibration with coloured lines representing different dose distributions in the source dish. Adapted from Lee et al. 2019.

Several observations supported this conclusion. Firstly, the MC simulation assuming uniform distribution produced survival curves that split into two apparent distinct curves as a function of their positioning above or below the source dishes (Figure 3.1-6). Calibration experiments measured doses using radiochromic films measured doses and

these disagreed with MC simulations that assumed a uniform distribution of source. Titration and microscopy of cold yttrium demonstrated precipitation in PBS, in which the source was mixed. Phosphate (PO_4^{3-}) is a large component of PBS and PO_4^{3-} precipitation of Y^{3+} is known to chemistry with a solubility product on the order of 10^{-25} (insoluble) (*88*). There was also the possibility that the charged surface of the sterilised dishes could affect ^{90}Y concentration gradient, but this was rejected when it was not possible to demonstrate the phenomenon in calibration experiments with untreated dishes.

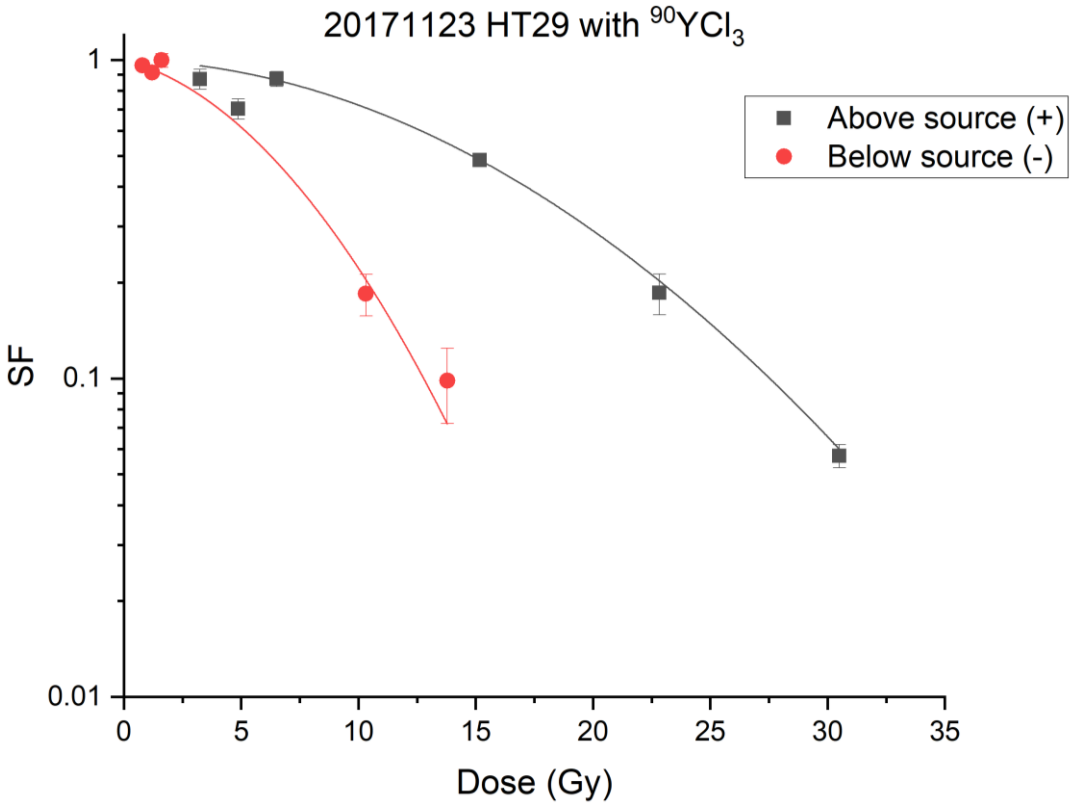

Figure 3.1-6 Example experiment demonstrating separation of the survival curve. Using *S*-values derived assuming uniform distribution, dishes below the source exhibited an apparently higher radiosensitivity than those above the source.

Although these findings did not definitely prove precipitation was the cause of the unexpected survival curve, the working hypothesis of precipitation was carried forward. Further evidence was revealed that the distribution of doses was due to precipitation of the

radiopharmaceuticals with the solvent. The discrepancy between the sources $^{90}YCl_3$ and ^{90}Y-DOTA-TATE also explained their differing gradients, occupying the bottom 25% and 75% of the source dish, respectively. Because DOTA-TATE is a chelator, the ^{90}Y here was less likely to be free of the counterion, whereas $^{90}YCl_3$ freely dissociates in solution of H_2O and was shown not to precipitate with in the case of non-radioactive YCl_3. The mixture with PBS stock resulted in precipitation observable at concentrations down to 0.2 µg/mL of YCl_3, which was in the upper range of concentration of the ^{90}Y sources, suggesting that precipitation effects could be involved. The final calibration experiments of absolute absorbed doses confirmed those predicted by the MC modelling adjusted for precipitation effects (Figure 3.1-7). Agreement within 10% difference was measured for each dish. These bottom 75% and 25% source distributions were applied to dosimetry for subsequent ^{90}Y dose-survival plots.

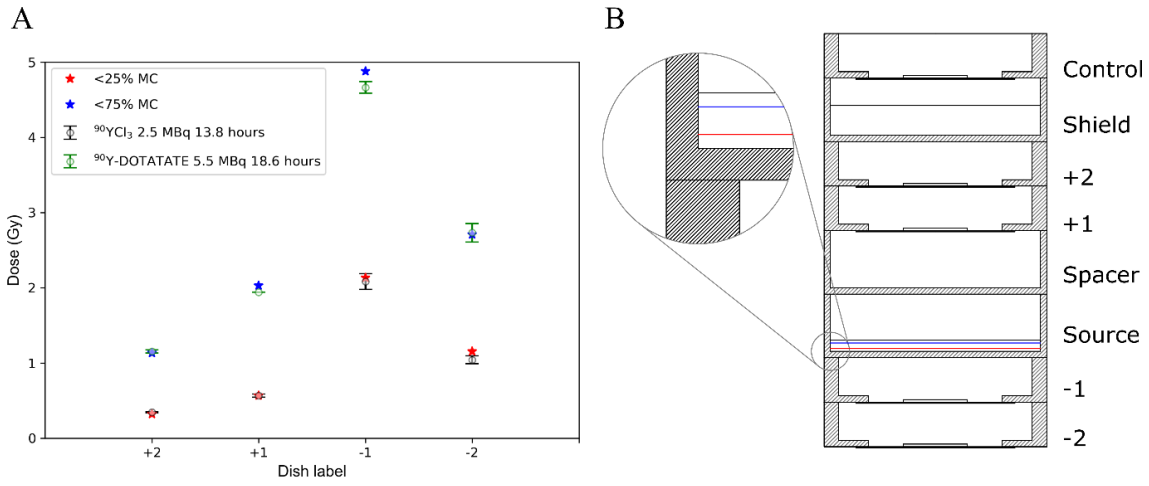

Figure 3.1-7 Validation from absolute doses using radiochromic film. (A) Absolute doses in each dish were predicted for each radiopharmaceutical formulation against radiochromic film measurements. (B) These predictions were based on the gradient of ^{90}Y in the source dish which varied according to the precipitation effects of each source. The presence of the film in the calibration experiments did not affect the dosimetry. The MC simulations

were run to predict deposited dose in different geometries for either the validation or cell experiments. Adapted from Lee et al. 2019.

3.2 Clonogenic assay radiosensitivity characterisation

All cell lines formed colonies in 7-9 days. HT-29 and DLD-1 cell lines formed discrete colonies and took up methylene blue stain with strong affinity. Hep3B had poorer uptake of methylene blue stain and had diffuse colonies (Figure 2.1-1), making colony quantification challenging. These issues were exacerbated for dishes exposed to higher doses of ionising radiation. Consequently, the GelCount™ device had greater difficulty in enumerating colonies for Hep3B and therefore generation of the cell survival curve was unreliable, even after optimisation of treatment parameters. The GelCount™ was used in lieu of manual counting in need of a consistent and objective methodology capable of counting thousands of colonies at a time. While the cell lines used did not always form visually easily distinguishable colonies, optimised thresholds set in the GelCount™ software were applied per each cell line.

3.2.1 Dose-survival curves

The experimentally-derived surviving fractions for DLD-1 and HT-29 are shown with the regression analysis in Figure 3.2-1. These results include a comparison of survival curves generated after cells were exposed to LINAC x-rays, ^{137}Cs γ-rays, and ^{90}Y β^- emissions. The large variation of the ^{90}Y values was likely due to the variety of sources of error. For example, pipetting radioactivity to irradiate colony-forming cells is an error prone process compared to irradiating with ^{137}Cs for less than an hour. Despite nearly an order of magnitude difference in source dose rates, the close agreement of LINAC and ^{137}Cs curves can be attributed to the acute exposure conditions which do not allow for damage repair

processes in the cell to take place. Table 3.2-1 summarises the fit parameters of the LQ model regression analysis. The fit parameters for both cell lines were generally in agreement with prior studies (*89*,*90*). Of the cell lines, HT-29 was less radiosensitive to the LINAC and ^{137}Cs with an α-value five times smaller and an α/β-ratio around ten times smaller compared to DLD-1. This indicates that HT-29 is more typical of a late-responding tissue, while DLD-1 is early-responding.

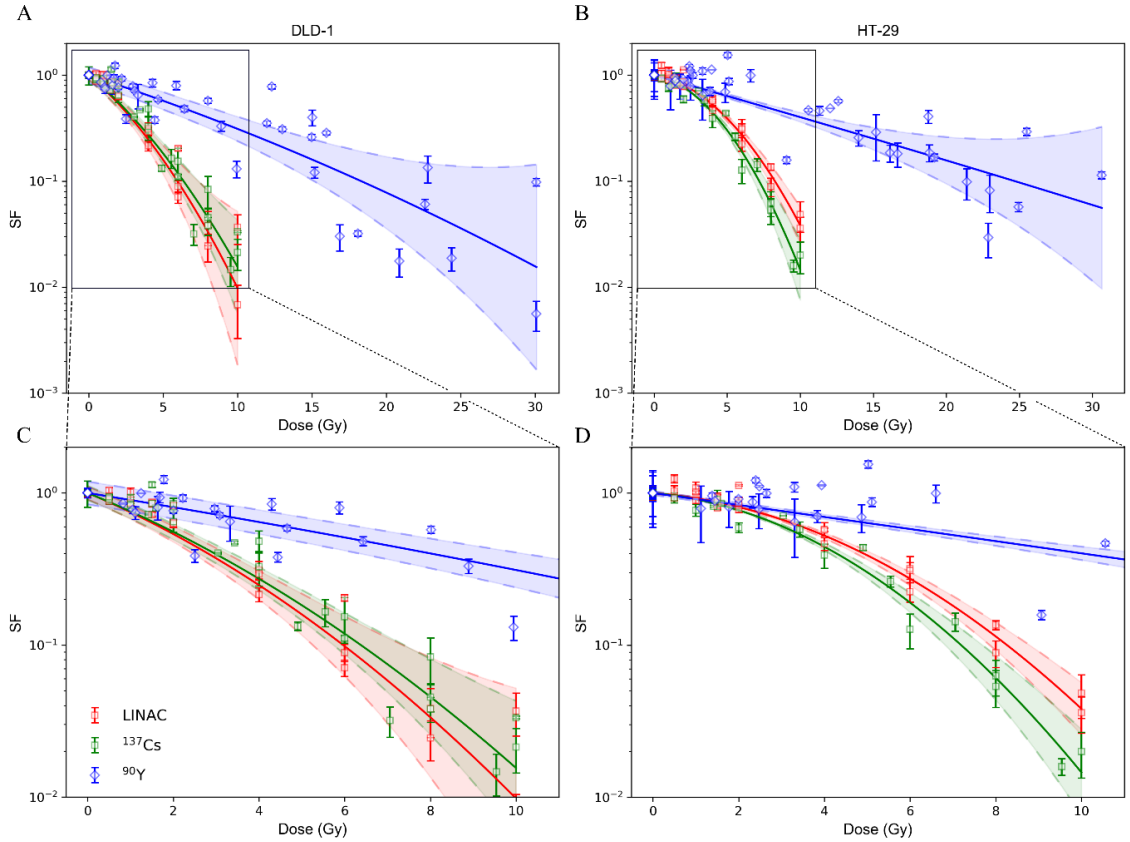

Figure 3.2-1 Survival curves as a function of absorbed dose from LINAC, ^{137}Cs, and ^{90}Y sources to CRC cell lines. (A) DLD-1 and (B) HT-29. Best fit lines from the regression analysis and 95% confidence bands are plotted with each curve. (C and D) An expanded view for the respective cell lines demonstrates the parameter fit values at the lower dose range. CRC. Adapted from Lee et al. 2019.

Table 3.2-1 Fit parameters from the regression analysis of CRC cell lines in Figure 3.2-1.

Cell line	Radiation source	α (Gy^{-1})	β (Gy^{-2})	α/β (Gy)
DLD-1	LINAC	0.273 [0.187 – 0.359]	0.0189 [0.00970 – 0.0282]	14.4 [3.15 – 25.7]
	^{137}Cs	0.264 [0.198 – 0.330]	0.0153 [0.00833 – 0.0222]	17.3 [5.37 – 29.1]
	^{90}Y	0.106 [0.075 – 0.137]	0.00109 [-0.000122 – 0.00230]	97.0 [36.8 – 231]
	^{90}Y†	0.129 [0.114 – 0.144]	0	N/A
HT-29	LINAC	0.050 [0.008 – 0.092]	0.0276 [0.0230 – 0.0323]	1.81 [0.0247 – 3.60]
	^{137}Cs	0.056 [0.00343 – 0.109]	0.0367 [0.0304 – 0.0429]	1.54 [-0.122 – 3.19]
	^{90}Y	0.090 [0.063 – 0.116]	0.000141 [-0.000969 – 0.00125]	637 [-4517 – 5792]
	^{90}Y†	0.0897 [0.0792 – 0.100]	0	N/A

†Fit using only the linear α component since β from the standard LQM is consistent with zero.

Adapted from Lee et al. 2019.

Generally, for both cell lines, the results for ^{137}Cs and LINAC were in close agreement with each other. However, the survival curves following exposure of both cell lines to ^{90}Y were markedly different compared to those for ^{137}Cs and LINAC. Attributable to damage repair during the protracted exposure, the findings agree with results for ^{90}Y experiments which were previously reported (*46*). These demonstrated α-values which varied depending on the cell line. For DLD-1, the α-value for ^{90}Y was approximately half that of ^{137}Cs and LINAC, whereas for HT-29, the α-value was approximately double. The 95% CI for the HT-29 α-value overlaps with the ^{137}Cs and LINAC 95% CI, while this is not true for DLD-1. The β-value for both cell lines was consistent with zero, which is contained in the confidence interval of the fit parameter.

Survival results for only ^{137}Cs were obtained for the HCC cell line Hep3B. Figure 3.2-2 illustrates the survival curve from ^{137}Cs experiments. This showed good agreement with previously published data. Although ^{90}Y results were absent, conclusions drawn from the

experience with CRC cell lines were applied to the Hep3B results with ^{137}Cs as an example of how to infer ^{90}Y radiobiological response for any given cell line. In particular, the assumption that ^{137}Cs and LINAC share the same LQ modelling parameters and that for ^{90}Y BED calculations $RBE_{max} \approx 0.6$ and $G_{\infty} \approx 0$ were applied (Table 3.2-2). This exercise served to demonstrate how results from more widely-available survival data from ^{137}Cs might be used to assume biological effective doses from LINAC and ^{90}Y SIRT using the RBE_{max}-based BED model. While this approach represents a starting point for more general BED modelling of ^{90}Y, this assumption has not been extensively tested and further evidence is necessary.

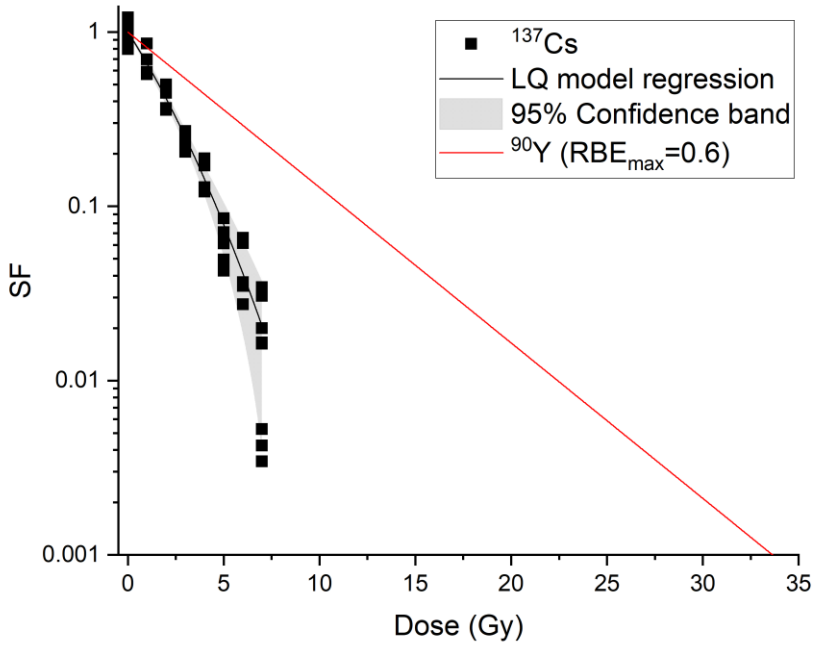

Figure 3.2-2 Survival curve of Hep3B cells exposed to ^{137}Cs with assumed ^{90}Y dose-response.

Survival for each well in triplicate for two biological repeats were fitted using the linear quadratic model with resultant fit values reported in Table 3.2-2. The expected ^{90}Y response curve was inferred from the assumed application of the RBE_{max} value derived from the CRC modelling results.

Table 3.2-2 The ^{137}Cs survival curve fit parameters from Hep3B experiments. Assumed working hypothesis parameters were derived for LINAC and ^{90}Y according to conclusions of the CRC results. The assumptions made were based that LINAC responds similarly to ^{137}Cs and ^{90}Y has an RBE_{max} of approximately 0.6 while the β-term is nearly zero.

Radiation source	α (Gy^{-1})	β (Gy^{-2})	α/β (Gy)
^{137}Cs	0.394	0.0229	17.2
LINAC	≈0.394	≈0.0229	≈17.2
^{90}Y	≈0.25	≈0	#N/A

≈ approximate value assumed from modelling parameters

3.2.2 Radiosensitivity parameters

The parameters RBE_{max} and G_∞ for the general BED model, equation (2), were derived from the survival curve fits of ^{90}Y and LINAC exposure. RBE_{max} was determined as the ratio of the α-parameters such that $RBE_{max} = \frac{\alpha_{90Y}}{\alpha_{LINAC}}$. G_∞ was determined from equation (1) using a T_{rep}-value calculated implicitly from G_T in equation (4), the full Lea-Catcheside formalism (Figure 3.1-1A). G_T was determined as the ratio of the β-parameters such that $G_T = \beta_{90Y}/\beta_{EBRT}$ and T was the 6-day exposure time. The value of G_T is constant for physiological half-times for repair (T_{rep}), i.e. <5 hours, see Figure 3.1-1B. The resulting parameters are summarised in Table 3.2-4.

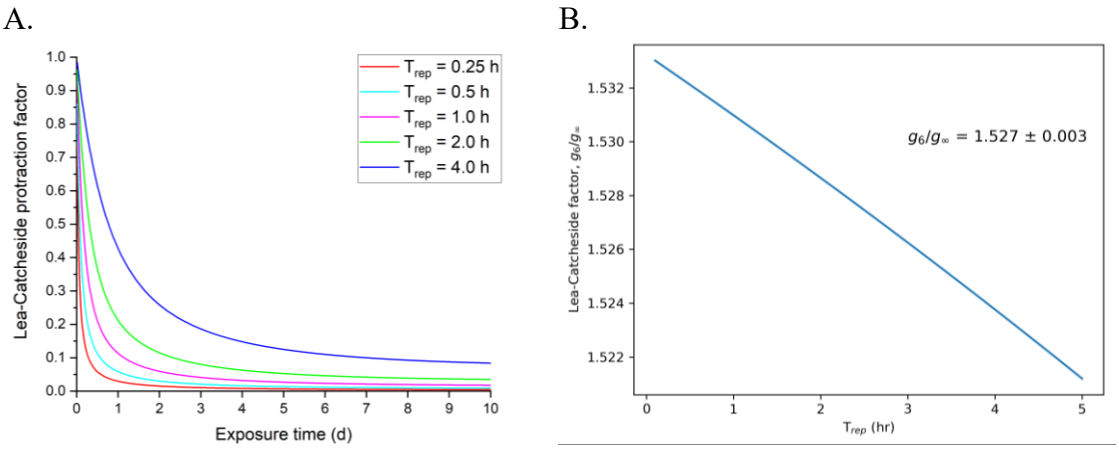

Figure 3.2-3 Implications of the Lea-Catcheside factor. (A) The Lea-Catcheside factor used to implicitly derive repair time. (B) Correction factor for the experimentally-derived Lea-Catcheside factor as a function of physiologically relevant repair times (T_{rep}<5 h)

Table 3.2-3 Derived parameters from experiments with CRC cell lines. Fit results were corrected for application to BED model.

Cell line	RBE_{max} ($\alpha_{90Y}/\alpha_{EBRT}$)	G_6 (β_{90Y}/β_{EBRT})	T_{rep} (h)	G_∞	$\alpha_{90Y}/G_\infty\beta_{EBRT}$ (Gy)
DLD-1	0.388 [0.221–0.555]	0.0577 [-0.0123–0.1277]	2.51 [-0.67–5.69]	0.0377 [-0.0102–0.0856]	148 [-56.3–353]
HT-29	1.800 [0.198–3.402]	0.0051 [-0.0351–0.0453]	0.21 [-1.48–1.90]	0.0033 [-0.0230–0.0296]	979 [-6911–8861]
Mixed model	0.554 [0.145–0.963]	0.0300 [-0.0117–0.0718]	1.28 [1.27–1.29]	0.0196 [0.0195–0.0198]	226 [-129–582]

The correction for exposure duration resulted in G-values which were about 35% smaller for both cell lines. This correction also inflated the α/β-ratios, which were already very high and potentially meaningless due to the confidence interval for the β parameter containing zero. The T_{rep} values varied from meaningless negative values up to 6 hours, and HT-29 was considerably lower with a 12.6 min repair half-time. As these values were derived from the β terms, which were not statistically significantly different from zero

(p>0.05), these repair times should not be taken too seriously. Final radiosensitivity parameter estimates correcting for the effects and including a mixed model (average of both cell lines) are summarised in Table 3.2-4.

Table 3.2-4 Estimated CRC radiosensitivity parameters for radiobiological modelling. These parameters have the correction factor of $\boldsymbol{G_\infty/G_6}$ incorporated on the β term for to correct for deviations resulting from 6-day versus indefinite exposure.

Cell line	Radiation source	α (Gy^{-1})	β (Gy^{-2})	α/β (Gy)
DLD-1	EBRT	0.273 [0.187 – 0.359]	0.0189 [0.00970 – 0.0282]	14.4 [3.15 – 25.7]
	^{90}Y	0.106 [0.075 – 0.137]	0.000716 [-0.00008 – 0.00151]	148 [-56.3 – 353]
HT-29	EBRT	0.050 [0.008 – 0.092]	0.0276 [0.0230 – 0.0323]	1.81 [0.0247 – 3.60]
	^{90}Y	0.090 [0.063 – 0.116]	0.000092 [-0.001018 – 0.001201]	979 [-6911 – 8861]
Mixed model	EBRT	0.176 [0.0092 – 0.256]	0.0219 [0.0136 – 0.0304]	8.02 [1.39 – 14.6]
	^{90}Y	0.0977 [0.075 – 0.12]	0.00043 [-0.00015 – 0.001]	226 [-129 – 582]

3.3 Radiobiological modelling

The parameters derived from survival curves and corrected for finite exposure of experimental conditions were applied to radiobiological models with various clinical applications.

3.3.1 Biological effective dose

BED models were adapted to the general BED equation (2) from Table 3.2-2 and Table 3.2-4. To summarise these results for application in the context of clinical data, the

parameters have been substituted into the general BED model in Table 3.3-1 below. For CRC and HCC cell lines, α/β-ratios of 8.02 and 17.2 Gy respectively were used. For general tumour and normal liver, α/β-ratios of 10 and 3 Gy respectively were used. A comparison between ^{90}Y absorbed dose and BED is shown in Figure 3.3-1, which illustrates this model through BED isodose curves. The BED model applied throughout this work, which accounts for variations in the α-term using the RBE_{max} concept, was compared in Figure 3.3-1 against the literature-based model, which corrects only for protraction effects.

Variation exists between the two models. The model previously used in literature assumes that BED, using EBRT as the reference radiation source, is always greater than physical dose absorbed from ^{90}Y. The mixed-model derived parameter results from Table 3.2-3 suggest that this assumption is unfounded because the 95% confidence interval for $RBE_{max} < 1$. The model employed here allows for BED to be less than physical dose through use of the RBE_{max} concept. For example, from a physical dose of 48.3 Gy of ^{90}Y, the conventional model used in literature yields a BED of 54.9 Gy. However, for the same dose, the model with the RBE_{max} term yields a BED of 32.5 Gy. This result implies that BED from the conventional methods is inflated.

Table 3.3-1 BED models based on results from *in vitro* work. (D is the absorbed dose from ^{90}Y SIRT, and n is the number of fractions delivered). Notably, these values match across modality, varying only with RBE_{max} and G-correction as mentioned previously.

Tissue	$BED_{^{90}Y}$ (Gy)	BED_{EBRT} (Gy)
CRC	$D\left(0.555 + \frac{D/n}{409\ \text{Gy}}\right)$	$D\left(1 + \frac{D/n}{8.02\ \text{Gy}}\right)$
HCC	$0.6D$	$D\left(1 + \frac{D/n}{17.2\ \text{Gy}}\right)$
General Tumour	$0.6D$	$D\left(1 + \frac{D/n}{10\ \text{Gy}}\right)$
Normal Liver	$0.6D$	$D\left(1 + \frac{D/n}{3\ \text{Gy}}\right)$

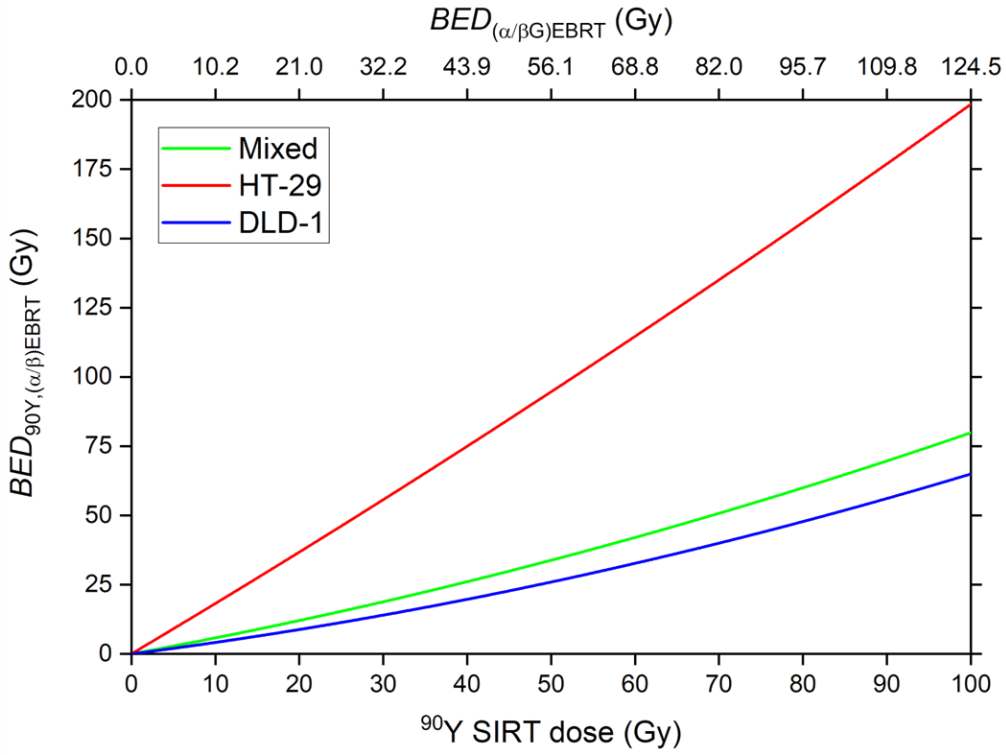

Figure 3.3-1 BED as a function of dose for each of the CRC cell lines and mixed model. The top BED axis includes representative values if the RBE_{max} correction were not made.

As demonstrated, the β-term was nearly zero. Thus, the HCC model, without ^{90}Y results, assumes that the α/β-ratio approaches infinity. Consequently, the expression for BED is reduced to a scalar of the absorbed dose (RBE_{max}). This same assumption was made and

applied for the other tissue types as results are challenging to acquire without clonogenic data. The assumption may not hold if the β-term demonstrably contributed to cell kill. Owing to the low contribution of the second term for ^{90}Y BED and the variability of α/β for EBRT, the following Table 3.3-2 has been made to summarise and simplify the findings of this work for application in patient data.

Table 3.3-2 Simplified BED models based on *in vitro* results. Proposed BED models listed in Table 3.3-2 were simplified to emphasise the important radiobiological findings in ^{90}Y clonogenic fit parameters of $RBE_{max} < 1$ and $\alpha/\beta \to \infty$. In this way, BED from ^{90}Y is always less than of EBRT and the quadratic component does not contribute to the model. D is the absorbed dose from ^{90}Y SIRT, and n is the number of fractions delivered.

Tissue	$\mathbf{BED_{^{90}Y}}$ (Gy)	$\mathbf{BED_{EBRT}}$ (Gy)
CRC	$0.6D$	$D\left(1+\frac{D/n}{8\ \mathrm{Gy}}\right)$
HCC	$0.6D$	$D\left(1+\frac{D/n}{17\ \mathrm{Gy}}\right)$
General Tumour	$0.6D$	$D\left(1+\frac{D/n}{10\ \mathrm{Gy}}\right)$
Normal Tissue	$0.6D$	$D\left(1+\frac{D/n}{3\ \mathrm{Gy}}\right)$

3.3.2 Equivalent dose to fractionated external beam radiotherapy

EQD was assessed based on the relationships defined in the appendix 8.3.3 below. Figure 3.3-2 below was based on the modelling parameters of Table 3.2-4. Since experimental doses only went up to 32 Gy, physical doses were extrapolated from the measured parameters to 100 Gy. On a Gy-by-Gy basis, this analysis demonstrates ^{90}Y SIRT would be less effective at inducing cell kill than LINAC. This deviates from the previous literature which assumes the opposite in the absence of experimental data.

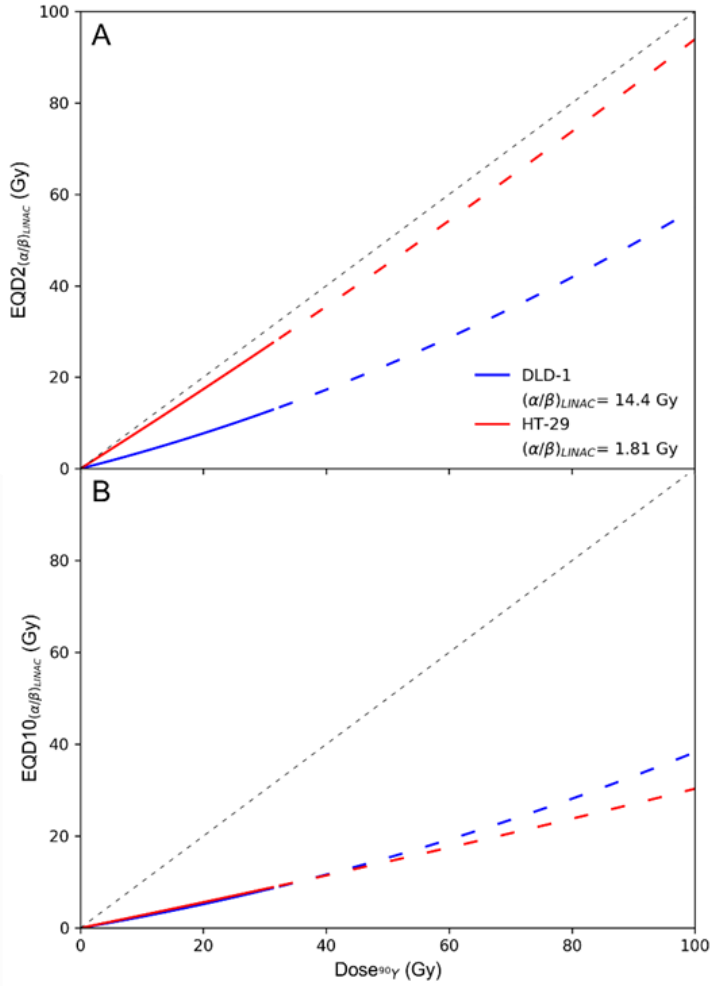

Figure 3.3-2 Isodose relationship between ^{90}Y absorbed dose and equivalent dose for fractionated EBRT treatment in (A) 2 Gy and (B) 10 Gy per fraction. Adapted from Lee et al. 2019.

3.4 Summary

This chapter explored the radiation response of tumour cell lines from CRC (DLD-1 and HT-29) and HCC (Hep3B) to irradiation from ^{90}Y SIRT compared to EBRT (6 MV LINAC and ^{137}Cs) using the clonogenic assay. A methodology for the ^{90}Y clonogenic assay was designed and validated in a custom experimental setup. Radiosensitivity parameters were derived from survival curves and applied to BED and EQD radiobiological models with the aim of describing ^{90}Y SIRT radiobiology in the clinic.

4 Assessment of biologically-informed dose response in colorectal cancer ^{90}Y microsphere patients

Continuing with the general aim of explaining treatment dynamics of ^{90}Y SIRT with radiobiology, the *in vitro* results from Chapter 3 were utilised to assess dose-response in a CRC patient cohort. Prior radiobiological modelling of SIRT assumed parameters from mathematical models but was not informed by the results of empirically-derived radiosensitivity to ^{90}Y. This patient cohort provided an opportunity to demonstrate the dose-response relationship of ^{90}Y SIRT while taking into account its radiobiological effects.

4.1 Patients

Of the 23 CRC patients included, characteristics at baseline were noted and are summarised in Table 4.1-1. No patient suffered from liver decompensation and, with only one patient presenting with pain and nausea post-treatment, ^{90}Y SIRT was generally well-tolerated. The median OS was 10.5 months from the time of treatment (Figure 4.1-1).

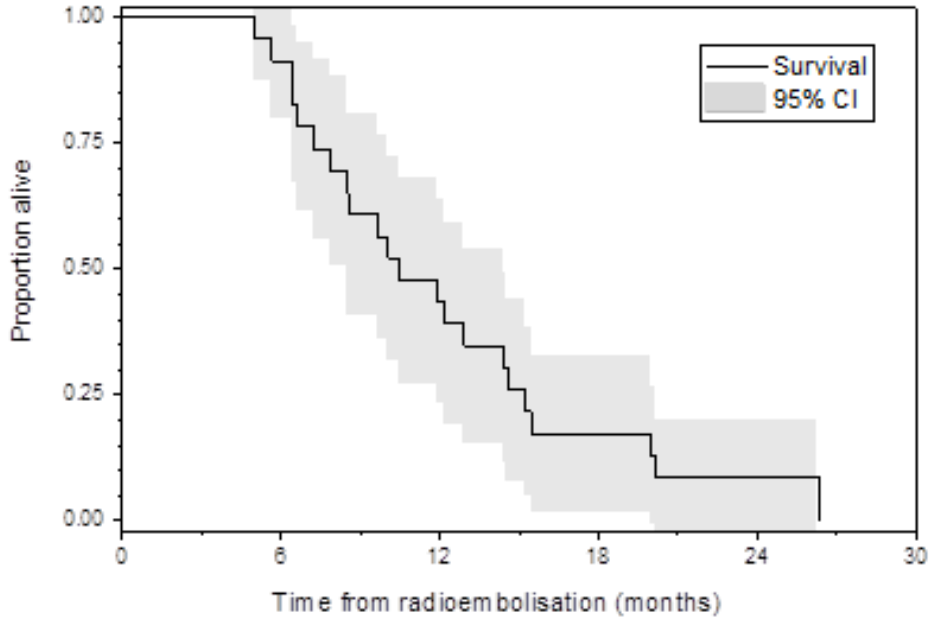

Figure 4.1-1 Survival curve of CRC patient cohort. Median OS was 10.5 months following radioembolisation with one patient censored as alive. Adopted from Abbott et al. 2020. (*91*)

Table 4.1-1 Patient characteristics at baseline (n = 23).

Characteristic	**N (%)** or **mean ± standard deviation**
Gender/Sex	
Male	14 (61%)
Female	9 (39%)
Age (y)	63±11
Primary site	
Colon	10 (43%)
Rectum	12 (52%)
Caecal	1 (4%)
Baseline individual tumour volume (mL)	107±284
[a]Baseline tumour burden (%)	20±16
<25%	17 (74%)
25-50%	5 (22%)
>50%	1 (4%)
[b]Baseline total tumour volume (mL)	436±471
Extrahepatic metastases	
Lung	12 (52%)
Bone	0 (0%)
Mediastinal	2 (9%)
Lymph node	7 (30%)
Prior systemic therapies	
1 line	2 (9%)
2 lines	13 (57%)
3 lines	8 (35%)
Prior EBRT	2 (9%)
Hepatectomy	7 (30%)
RAS mutation	7 (30%)
SIRT treatment	
Coil embolisation	22 (96%)
Number of tumours	96
Number of tumours considered per patient	4.0±2.4
Administered activity (MBq)	1469±428

[a]Percentage (%) tumour volume of the whole liver, including tumour

[b]Sum volume of the baseline CT tumour contours

4.2 Volumetry

Of the 94 tumours evaluated, measured volumes at baseline ranged from 0.3 to 2114 mL. However, for dosimetric analyses, only tumours >1 mL were considered. Figure 4.2-1 illustrates the baseline tumour volume against percentage change in volume post-^{90}Y SIRT. Linear regression did not demonstrate a statistically significant relationship (p=0.19).

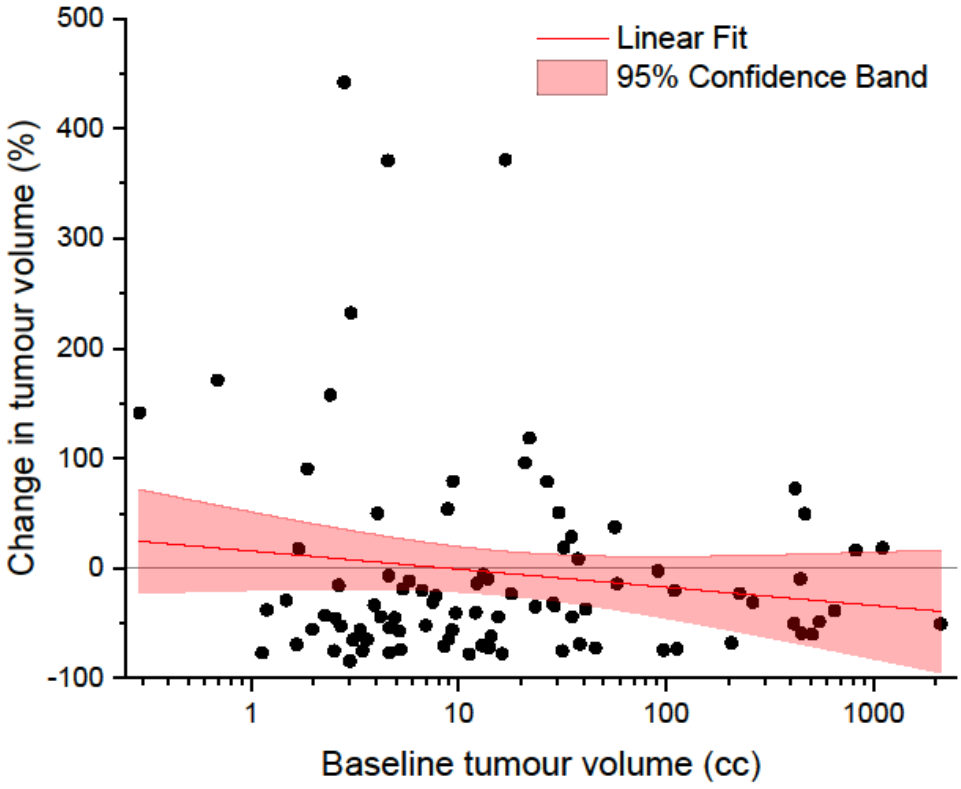

Figure 4.2-1 No relationship between baseline tumour volume and change in volume at 3 months. The 24 tumour datapoints above the black horizontal line, a minority out of 96 total, indicate individual tumours which progressed in volume. The points below represent that a majority of tumours decreased in volume post-treatment. Adopted from Abbott et al. 2020. (*91*)

4.3 Dose-response

For tumours greater than 1 mL, the measured mean absorbed radiation dose ranged from 2.2 – 84.8 Gy. The mean of mean doses was 35.5 ± 9.4 Gy. The median of mean doses was 32.9 Gy (interquartile range, 23.3 – 46.8). For normal liver, the measured mean doses ranged from 15.4 – 41.3 Gy. The mean of mean doses was 26.4 ± 6.8 Gy. The median of mean doses was 24.9 Gy (interquartile range, 22.3 – 30.6).

Linear regression showed an association of mean absorbed tumour dose with percentage change in tumour volume at 3-months from baseline (Figure 4.3-1). Mean, median, and D_{70} dose metrics were each statistically significantly correlated with tumour volume reduction by 1.8% ($p < 0.005$, Figure 4.3-1), 1.8% ($p < 0.005$), and 1.5% ($p < 0.01$) per Gy, respectively. None of the tumours increased in volume after receiving threshold mean, median, and D_{70} doses of greater than 48.3 (Figure 4.3-1), 48.8, and 41.8 Gy, respectively. Dose heterogeneity in tumours, as measured by relative standard deviation (RSD), was not statistically significantly correlated with percentage change in tumour volume ($p > 0.5$). However, it is possible that the partial volume effect and low resolution of the SPECT-based dosimetry relative to the true radiopharmaceutical distribution has impacted the measurement of dose heterogeneity. Blurring from the effect produces artificially low variance in dose signal across voxels, as can been observed when comparing to PET imaging or microdosimetric models.

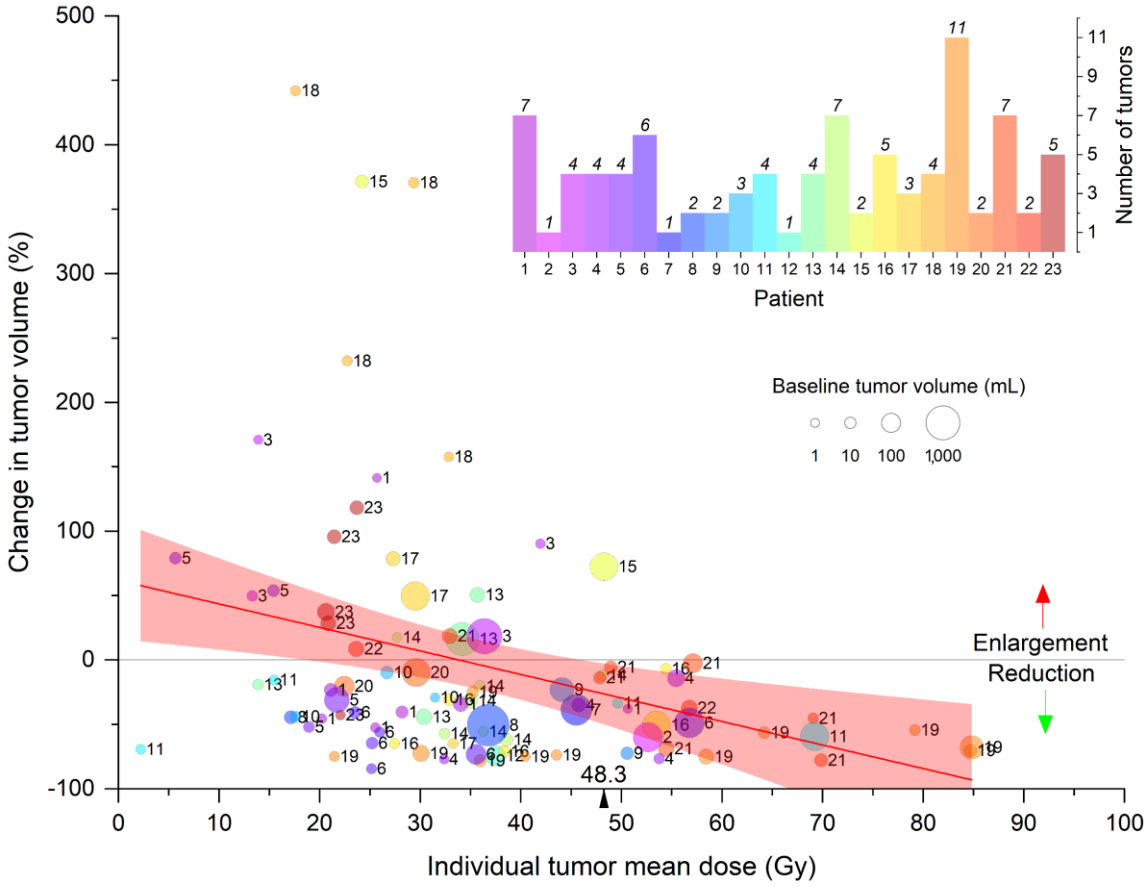

Figure 4.3-1 Dose-response in individual CRC tumours Each tumour is numbered and colour-coded according to the patient from which it was measured (key in upper right quadrant). Percentage change in tumour volume was measured at 3-months followup relative to the baseline imaging. Baseline imaging was used to indicate tumour volume, based on the size of the circle drawn. The red linear regression fit line and corresponding 95% confidence band (95% CI 0.7–3.0%, p<0.005, R^2=0.102) shows a reduction in tumour volume of 1.8% per Gy of absorbed dose. All tumours receiving >48.3 Gy of mean dose reduced in volume, as indicated by the grey horizontal line and the tick on the x-axis. Adapted from Abbott et al. 2020. (*91*)

Individual tumours from each patient were assessed against vRECIST response criteria (Figure 4.3-2). PD was demonstrated in 23% of tumours, while SD and PR were demonstrated in 63% and 23% of tumours respectively.

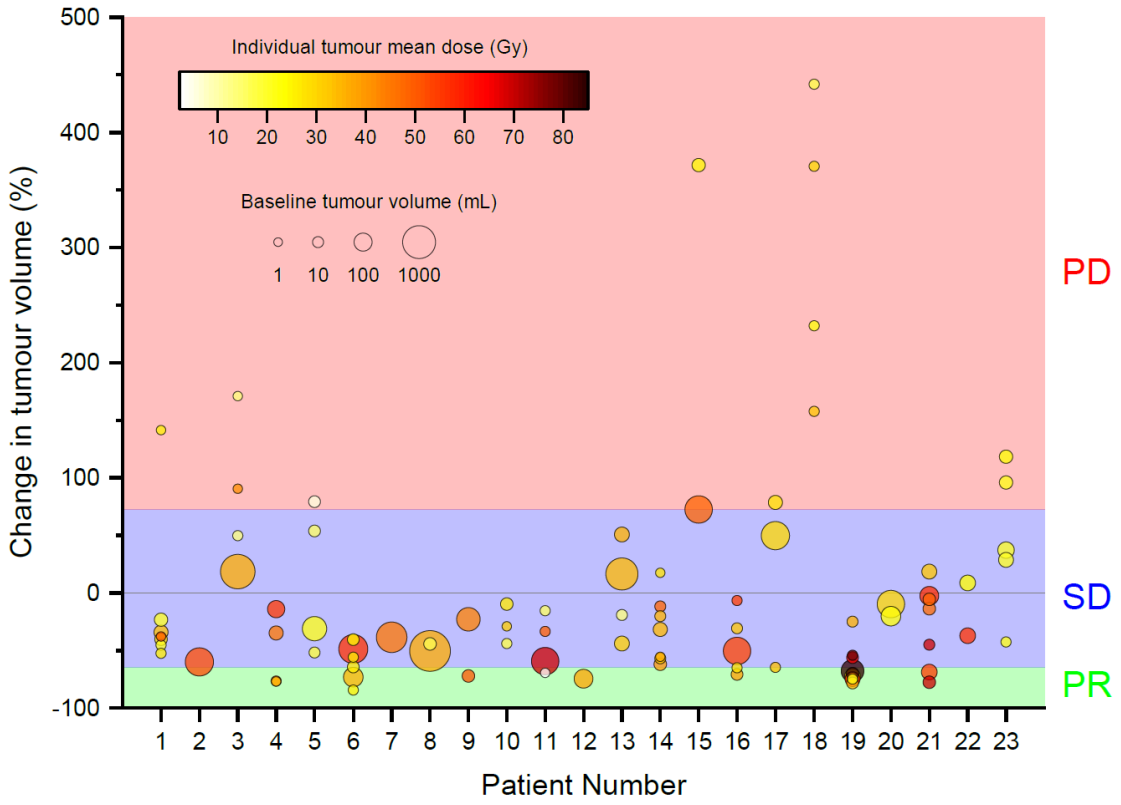

Figure 4.3-2 Tumour responses per patient, at three months followup relative to baseline. Baseline tumour volume is indicated by the size of the circle and the colour indicates tumour mean dose. The background colouring indicates the category of vRECIST response based on % change in tumour volume. Tumours that reduced by ≥65% were PR, increased by ≥73% were PD, and otherwise were SD. Relative change in tumour volume was typically consistent within each patient, however the discrete nature of vRECIST categorisation failed to capture this in borderline cases such as patients 6 and 19. Continuous measures of response like volumetry may be favourable. Adopted from Abbott et al. 2020. (*91*)

No patient had CR and the majority of patients achieved mixed response across all their tumours (Figure 4.3-3, Figure 4.3-4, and Figure 4.3-5). Patients 15 and 18 (Figure 4.3-6) had tumours that were exclusively all designated as PD. Mean, median, and D_{70} tumour doses were associated with PR (compared to SD and PD) with ORs of 1.09 ($p < 0.05$),

1.09 ($p < 0.01$), and 1.10 ($p < 0.0001$) respectively. RSD was not statistically significantly correlated with vRECIST response ($p > 0.5$).

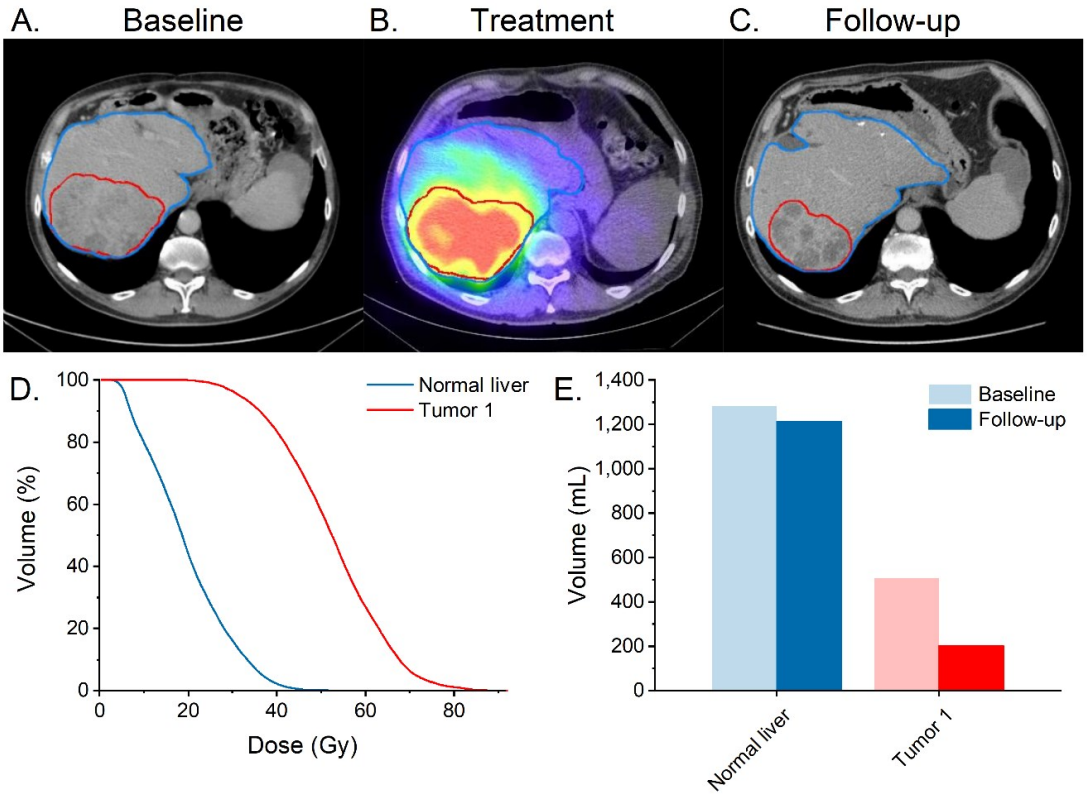

Figure 4.3-3 Best response sample case. Patient 2 (male, 75 y, 1.78 m^2 BSA) had a low rectal cancer *in situ* at the site of a polypectomy and lung metastases. Prior to ^{90}Y SIRT, he was given three courses of chemotherapy, had a hepatic resection, and underwent coil embolisation to achieve a 16.8% lung shunt. (A) His baseline CT was obtained 15 d prior to ^{90}Y SIRT treatment, which was delivered with 1562 MBq of administered activity. (B) The SPECT/CT revealed an ideal deposition of the microspheres in relation to tumour tissue. There was little deposition in normal liver and no adverse effects. (C) Although extrahepatic disease remained, the follow-up CT imaging 80 d after ^{90}Y SIRT demonstrated response in the liver. (D) The distribution of doses to normal liver and tumour were summarised as DVHs, which demonstrated considerably higher doses achieved in tumour tissue compared to normal liver. (E) Tumour volumes at follow-up demonstrated a substantial reduction in tumour volume compared to baseline. Adopted from Abbott et al. 2020. (*91*)

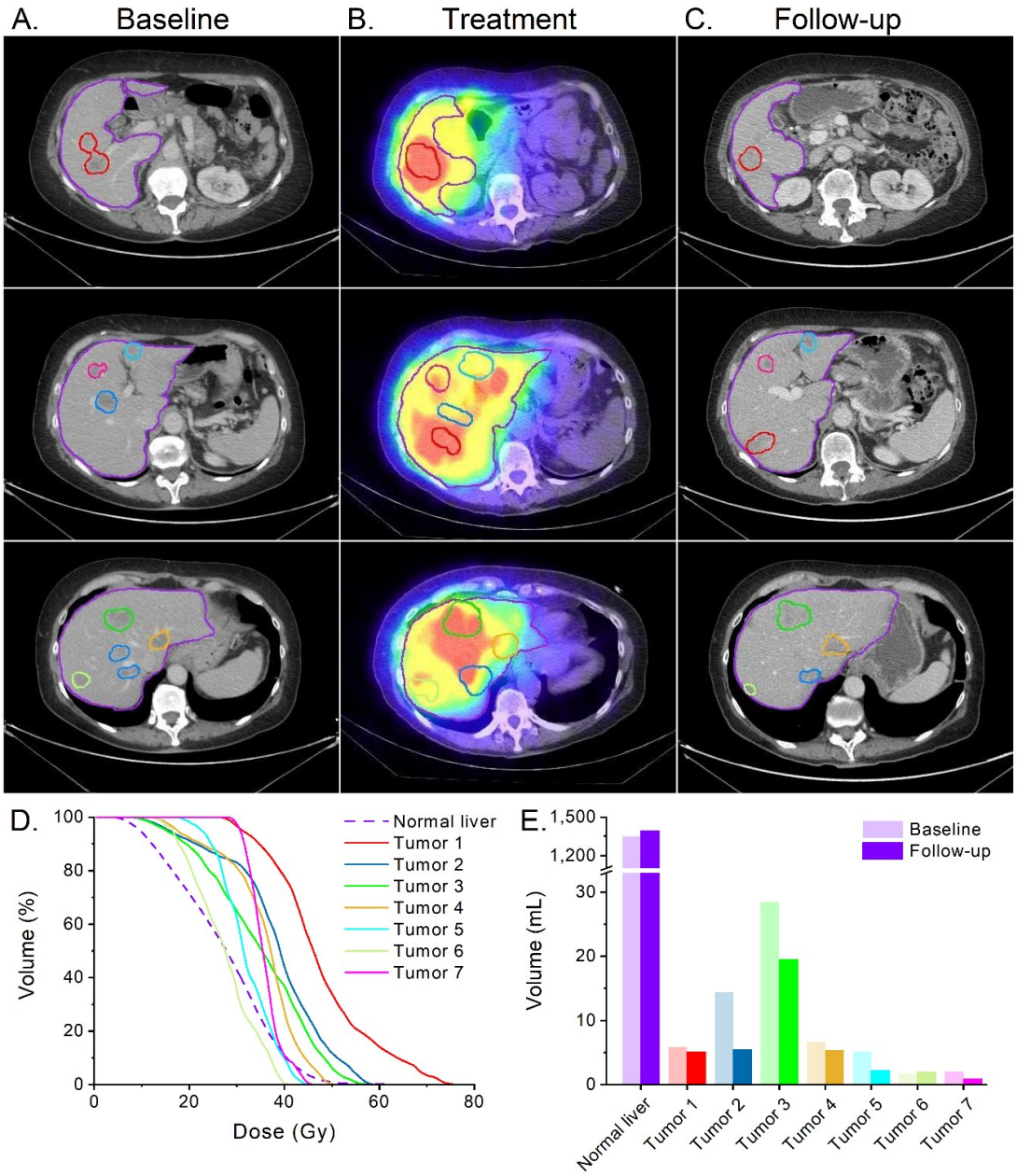

Figure 4.3-4 Mixed response sample case. Patient 14 (female, 66 y, 1.70 m^2) presented with a descending/sigmoid colon adenocarcinoma with ovarian and lung metastases. Surgical resection of the primary tumour was performed, and three courses of chemotherapy were administered. Prior to ^{90}Y SIRT, coil embolisation was performed prevent shunting to lungs. To visualise all the tumours, three cross-sections per CT scan were selected and stacked for comparison across the timepoints. (A) The baseline CT was obtained 27 d prior to ^{90}Y SIRT treatment with 939 MBq of administered activity. (B) Following ^{90}Y SIRT, the patient reported pain and nausea. SPECT/CT revealed mixed uptake of the

microspheres to the tumours. (C) A follow-up CT scan 74 d after ^{90}Y SIRT demonstrated partial response in some of the tumours, and one tumour showed progression. (D) According to the distribution of doses in the summary DVHs, this tumour had uniform doses but the absorbed dose was lower than that for normal liver in some areas. (E) Tumour volumes at follow-up demonstrated variable response compared to baseline. Adopted from Abbott et al. 2020. (*91*)

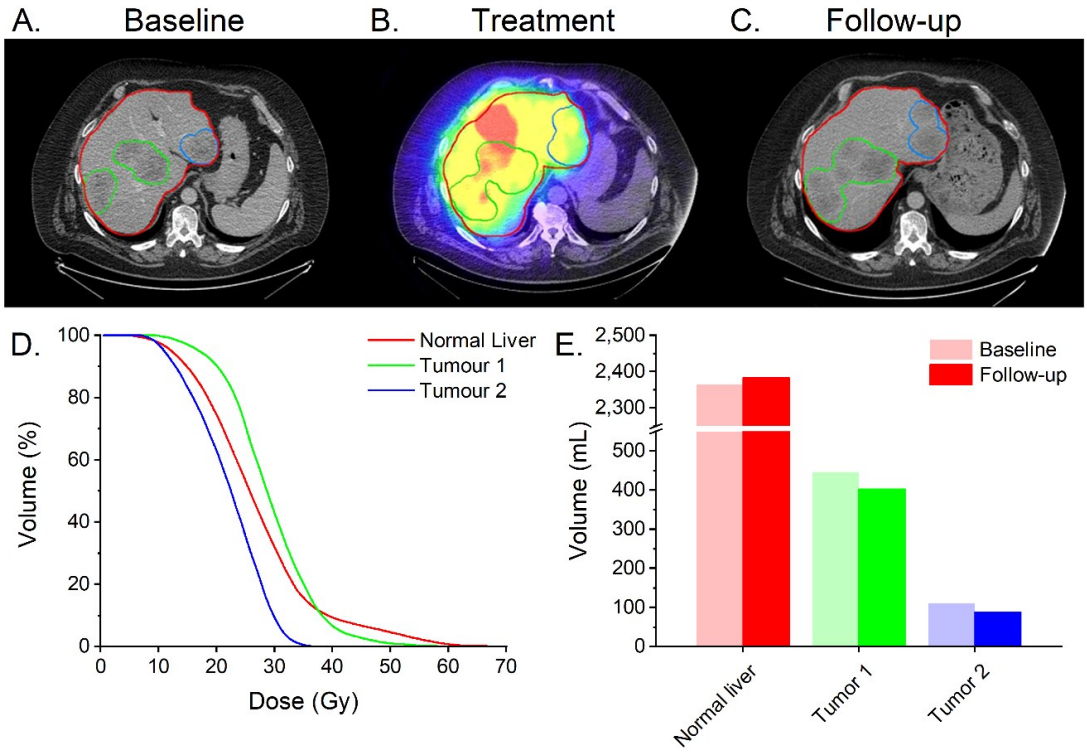

Figure 4.3-5 No response sample case. Patient 20 (male, 63 y, 2.74 m^2 BSA) had a resected rectal carcinoma with a Ras mutation, which was associated with mediastinal lymph node metastases. Prior to ^{90}Y SIRT, the patient received one course of chemotherapy and underwent coil embolisation to reduce shunting to the lungs to 4.7% of volume of injectate. (A) The baseline CT was obtained 13 d prior to ^{90}Y SIRT treatment with 1863 MBq of administered activity. (B) Following ^{90}Y SIRT, SPECT/CT revealed a suboptimal distribution of microspheres with no clear association of radioactivity with delineated tumours. No adverse events were reported. (C) A follow-up CT 74 d after ^{90}Y SIRT demonstrated insignificant change in tumour volumes. (D) The distribution of doses summarised in DVHs, which revealed that normal liver and tumours received comparable radiation absorbed doses. The dose values were generally lower compared to Patient 2 (Figure 4.3-3) and Patient 14 (Figure 4.3-4). (E) Tumour volumes at follow-up demonstrated stable disease compared to baseline. Adopted from Abbott et al. 2020. (*91*)

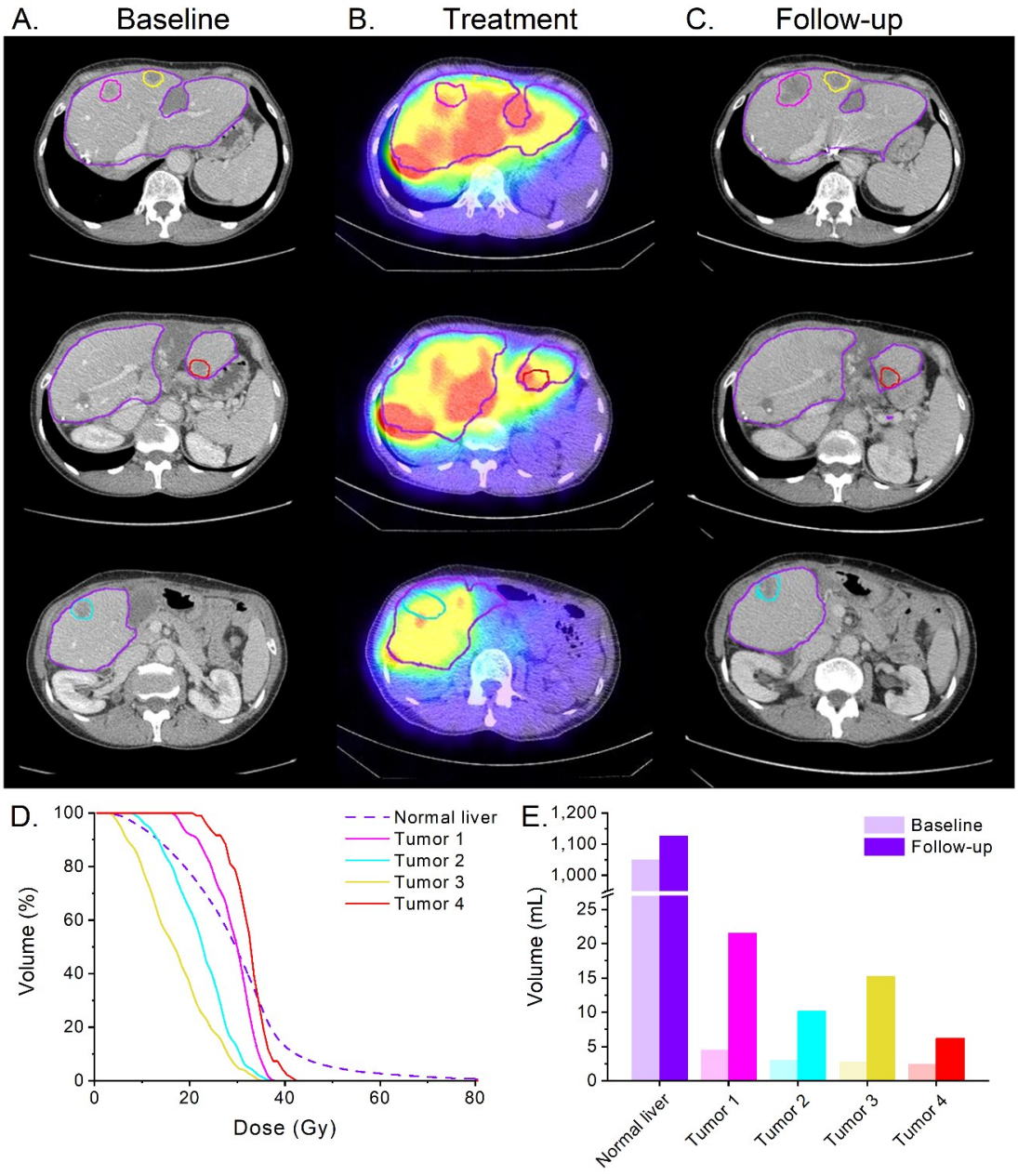

Figure 4.3-6 Worst-outcome sample case Patient 18 (female, 66 y, 1.53 m^2 BSA) underwent resection of a rectal carcinoma. Prior to ^{90}Y SIRT, two courses of chemotherapy were administered, and the patient underwent coil embolisation to abolish shunting to lungs. To visualise all the tumours, three cross-sections per CT scan were selected and stacked for comparison across the timepoints. (A) A baseline CT was obtained 13 d prior to ^{90}Y SIRT treatment, which was delivered with 847 MBq of administered activity. (B) Following ^{90}Y SIRT, SPECT/CT revealed a suboptimal distribution of microspheres with no clear association of radioactivity with delineated tumours. The denser tissue in the anterior of

the left lobe seen in the top row which seems to get a large dose from ^{90}Y is gall bladder. As the subsequent row of images suggests, dose was not specific to gall bladder. As illustrated by the bleed-through of large ^{90}Y dose on the posterior of the right lobe, which is not probable from escape of the microspheres from the liver, the poor resolution of the SPECT imaging likely resulted in signal in the gall bladder from ^{90}Y within the liver on an adjacent transaxial slice. No adverse events were reported. (C) A follow-up CT scan 77 d after ^{90}Y SIRT demonstrated that the volume of all tumours had increased. (D) According to the distribution of doses in the summary DVHs, the tumours did not receive higher uniform doses from ^{90}Y SIRT than normal liver. (E) Tumours at follow-up were all more than double in volume compared to baseline. Adopted from Abbott et al. 2020. (*91*)

4.4 Biological effective dose

Voxelised doses were transformed to voxelised BEDs for each patient. BED was calculated according to the model of CRC response to ^{90}Y shown in Table 3.3-1. This model accounted for a distribution of radiosensitivities as the modelling parameters were derived from a statistical mixed model including two cell lines with differing radiosensitivities.

The median of the 96 tumours evaluated for mean, median, and D_{70} BEDs was 21.0 Gy (range 1.24 – 67.7 Gy), 20.9 Gy (range 1.22 – 65.3 Gy), and 17.4 Gy (range 1.13 – 55.5 Gy), respectively. Using linear regression, the percentage change in volume of each tumour was statistically significantly correlated with these BED metrics ($p < 0.01$, $p < 0.005$, and $p < 0.01$, respectively). RSD from individual tumour BEDs was not statistically significantly associated with change in tumour volume ($p = 0.5$).

Individual patient vRECIST response was assessed using logistic regression with PD against PR and SD as a measure of response. Mean, median, and D_{70} BED metrics were statistically significantly associated vRECIST response with ORs of 1.10 ($p < 0.01$), 1.10

($p < 0.01$), and 1.09 ($p < 0.0001$), respectively. RSD from BEDs was not statistically significantly associated with vRECIST response ($p > 0.5$).

4.5 Perfusion

Ten of the 23 patients (43%) had perfusion imaging. Patients were imaged with pCT at baseline (median 8 days and range 1-20 days prior to ^{90}Y SIRT) and again at one-month (median 29 days and range 24-36 days following ^{90}Y SIRT, excluding one patient that did not have a post-treatment scan) and at three-months (median 69 days and range 60-85 days) following ^{90}Y SIRT. Patients were imaged with DCE MRI at baseline (median 11 days and range 6-20 days) prior to ^{90}Y SIRT and again at one-month (median 31 days and range 29-41 days) following ^{90}Y SIRT and three-months (median 70 days and range 66-80 days) following ^{90}Y SIRT, excluding one patient that did not have a post-treatment scan.

Contours for the inferior vena cava, aorta, normal liver, and tumours were created by oncologist Helen Winter. The contrast-enhanced signal within each contour was plotted against time to demonstrate the perfusion of the bolus injected into the bloodstream as it passed through the liver. Examples of the resultant signal enhancement curves are given for pCT in Figure 4.5-1D and for DCE MRI in Figure 4.5-2. After processing in the respective perfusion software, parameter maps were generated, as demonstrated with an example for pCT in Figure 4.5-1E and F and for DCE MRI in Figure 4.5-3.

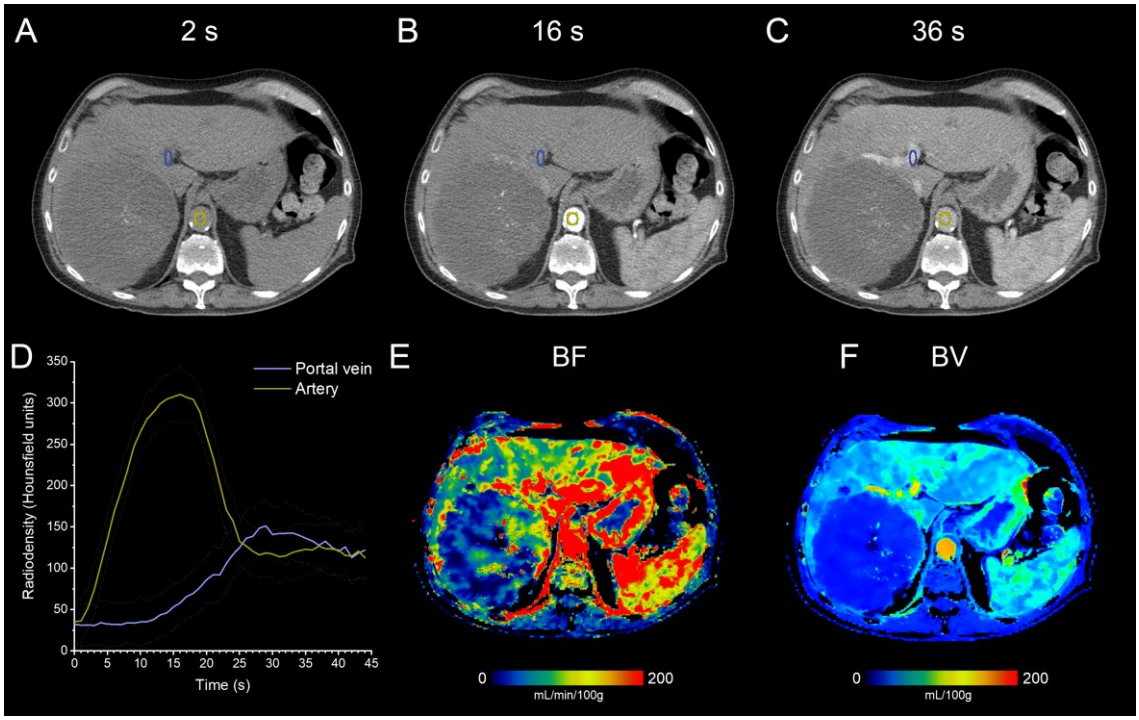

Figure 4.5-1 Perfusion CT analysis sample case. Patient 3 had pCT imaging acquired at three-months following ^{90}Y SIRT. A bolus of contrast was injected into the patient and CT images were collected every second to visualise as it permeated through the liver with (A) pre-enhancement at 2 seconds, (B) maximum arterial enhancement at 16 seconds, and (C) maximum portal vein enhancement at 29 seconds post-injection. The final pre-enhancing image was selected at 2 seconds post-injection. The contours were defined for artery and portal vein, the liver and tumours. (D) The contours were used to generate the respective signal enhancement curves. Standard deviations from the voxels in the contours were acquired and plotted as the dashed line for each timepoint. Each voxel was fitted to the time-dependent model as detailed in the GE liver perfusion manual (*83*). Fit parameters for each voxel resulted in 3D parameter maps such as the 2D transaxial cross sections for (E) blood flow (BF) and (F) blood volume (BV). The mean transit time (MTT) map (not shown) was created and related to (E) and (F) by the relationship MTT = BV/BF. Both of these maps highlight a clear distinction between perfusion in the large tumour in the right lobe (dark blue) and the surrounding normal liver tissue, which is better vascularised. The distribution of tumour perfusion parameter values was summarised by the average in the

contour and used for the subsequent analysis in comparison to dosimetry and other pCT imaging timepoints along the treatment timeline for the patient.

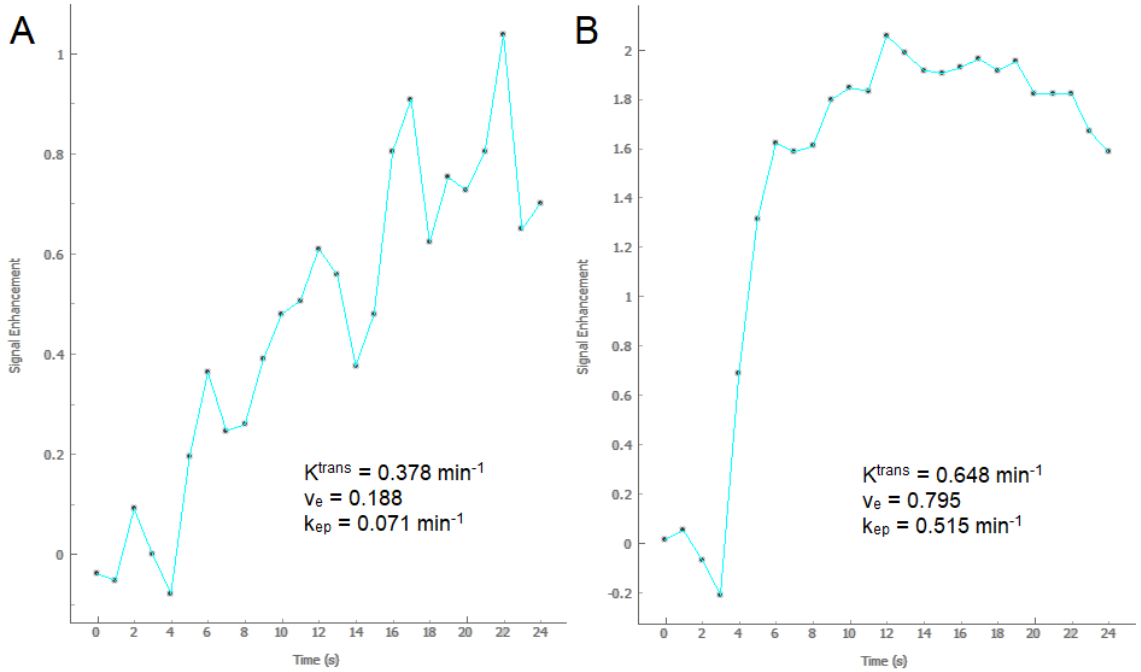

Figure 4.5-2 Dynamic contrast-enhanced MRI perfusion analysis sample case. Exemplar signal enhancement curves for individual voxels with (A) low- and (B) high-enhancement were generated from contours defined in ITK-SNAP, as seen in Figure 4.5-3. The resulting model parameters K^{trans}, v_e, and k_{ep} varied by a factor of 1.7, 4.2, and 7.3 respectively between low- and high-enhancing voxels.

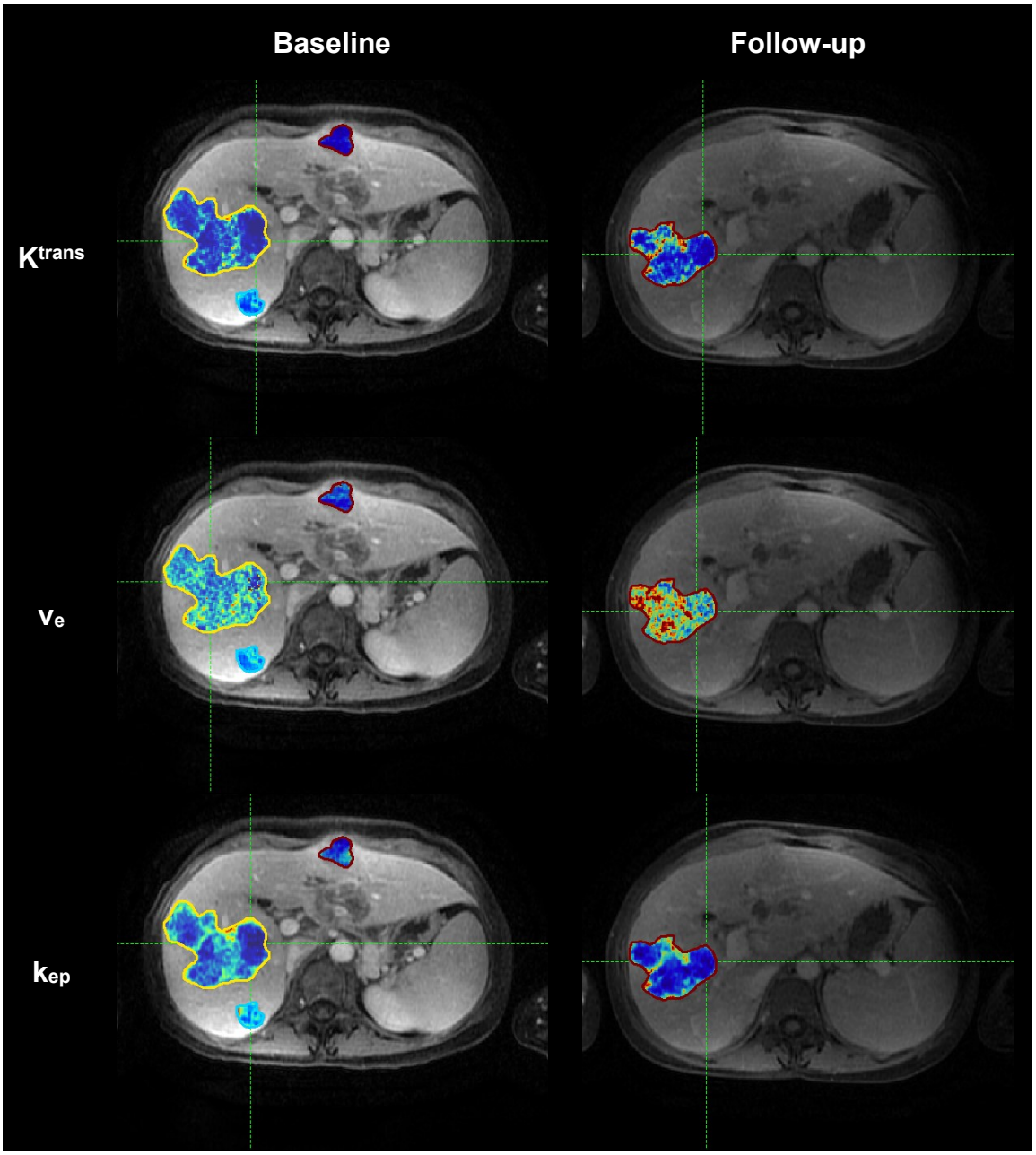

Figure 4.5-3 Dynamic contrast-enhanced MRI sample case parameter maps. Voxelised maps are shown within the tumour contours for DCE MRI modelling fit parameter values K^{trans}, v_e, and k_{ep}. Change from baseline to 3-month follow-up of the perfusion within the large tumour volume is apparent. The increase (reddening) of v_e indicates that the tumour EES has increased perfusion, possibly a consequence of treatment. The increase in K^{trans} along the boundary between the right anterior and left posterior halves of the large tumour indicate that the volume transfer between the blood plasma and EES increased, which

could indicate increased vascularisation following treatment. The tumour contours were used to extract parameters based on mean value.

Linear regressions were performed to test several of the hypothesised relationships and quantify the effect size. In general, statistically significant associations were identified for relationships with either average ^{90}Y tumour dose or volumetric response. Notably, correlations were found only for pCT with the exception of baseline DCE MRI k_{ep} against volumetric response at three-months. All quoted metrics were reduced to averages across all tumour voxels for the comparisons as follows.

In Figure 4.5-4, statistically significant associations of baseline perfusion parameters were found with dose in only BF and MTT with slopes of 0.056 Gy/(mL/min/100g) ($p<0.001$) and -2.776 Gy/s ($p<0.001$) respectively. Additionally, baseline DCE MRI k_{ep} was associated with volumetric response at three months at 46.5% volume per min^{-1} ($p<0.05$).

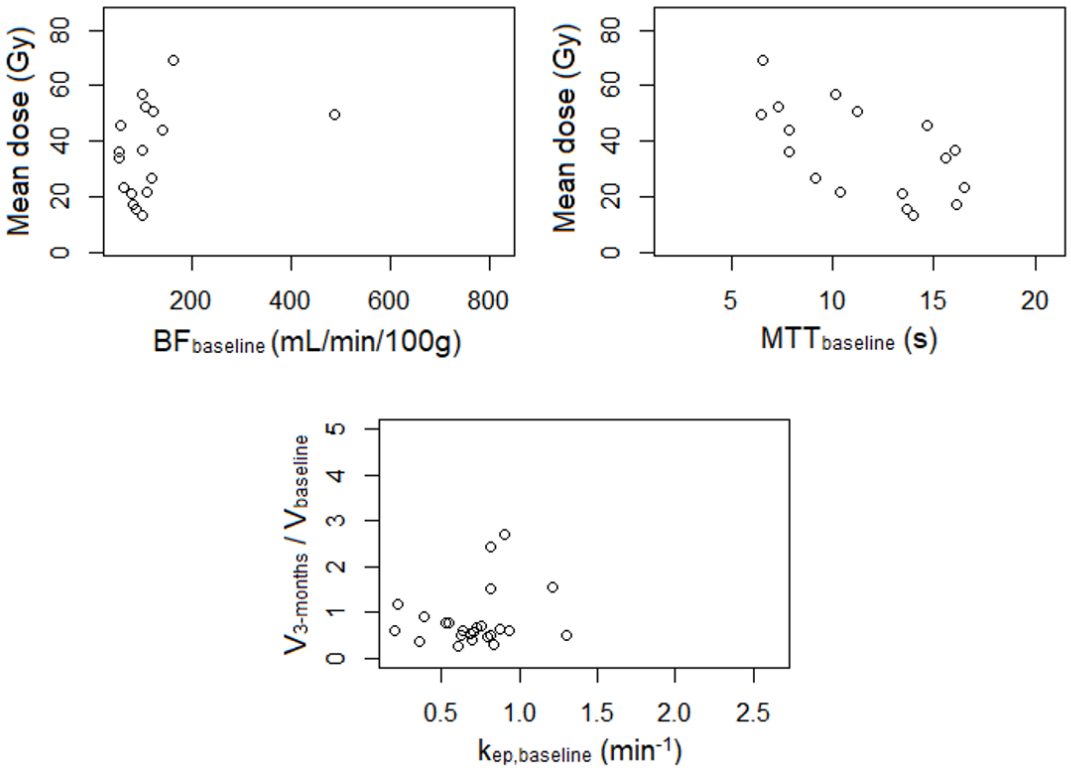

Figure 4.5-4 Assessment of various baseline perfusion imaging metrics as an explanatory variable of mean dose deposition in tumours and volumetric response at 3-months follow-up. Statistically significant relationships between baseline perfusion metrics and dose or volumetric response were derived, despite variation in the data, such as an outlier in baseline BF in the first plot.

As demonstrated in Figure 4.5-5, change in baseline perfusion at one-month follow-up for BF, PS, and MTT was statistically significantly associated with dose with slopes of -0.083 Gy/(mL/min/100g) ($p=0.006$), 0.933 Gy/(mL/min/100g) ($p<0.001$), and 1.640 Gy/s ($p<0.001$), respectively. Likewise, volumetric response at one-month follow-up was statistically significantly associated only for PS where tumours decreased in volume by 1.9%/(mL/min/100g) ($p=0.004$).

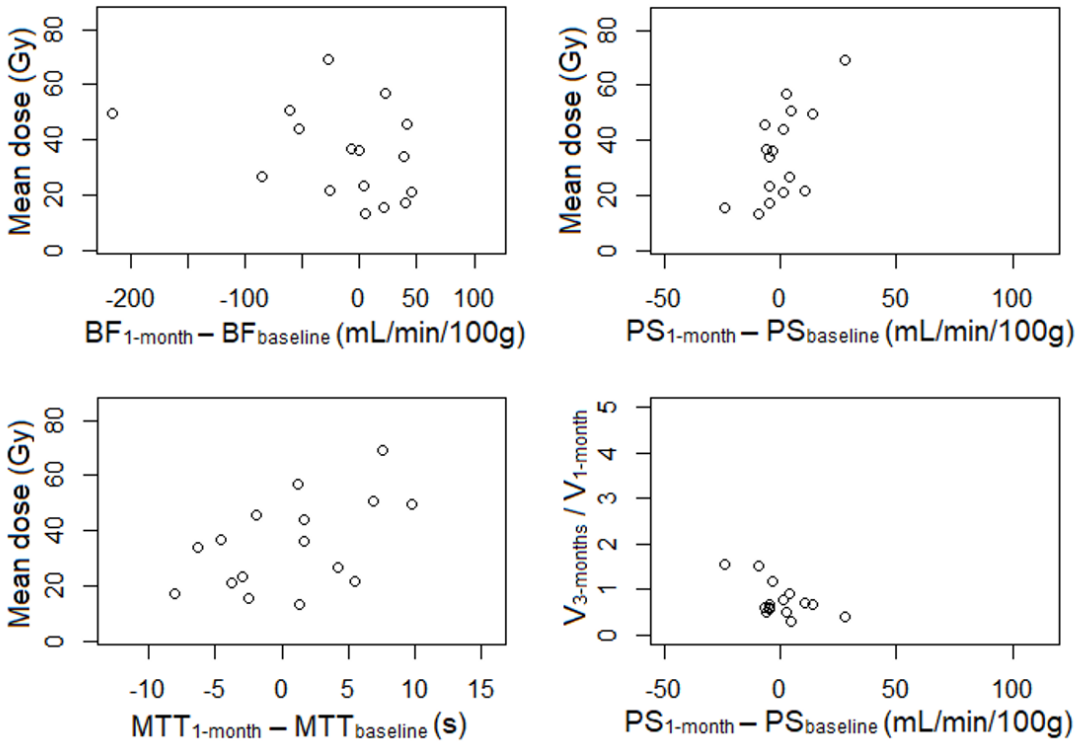

Figure 4.5-5 Assessment of change at one-month follow-up from baseline from various pCT metrics against deposited mean dose to tumours and volumetric response at three-months follow-up.

As demonstrated in Figure 4.5-6, change in baseline perfusion at three-months follow-up for BV, BF, PS, and MTT was statistically significantly associated with dose with slopes of 2.090 Gy/(mL/100g) ($p<0.001$), -0.065 Gy/(mL/min/100g) ($p=0.001$), 0.185 Gy/(mL/min/100g) ($p=0.021$), and 1.742 Gy/s ($p<0.001$), respectively. Moreover, change in BV at three-months was associated with volumetric response whereby the slope demonstrated a tumour volume reduction of 3.9%/(mL/100g) ($p=0.015$).

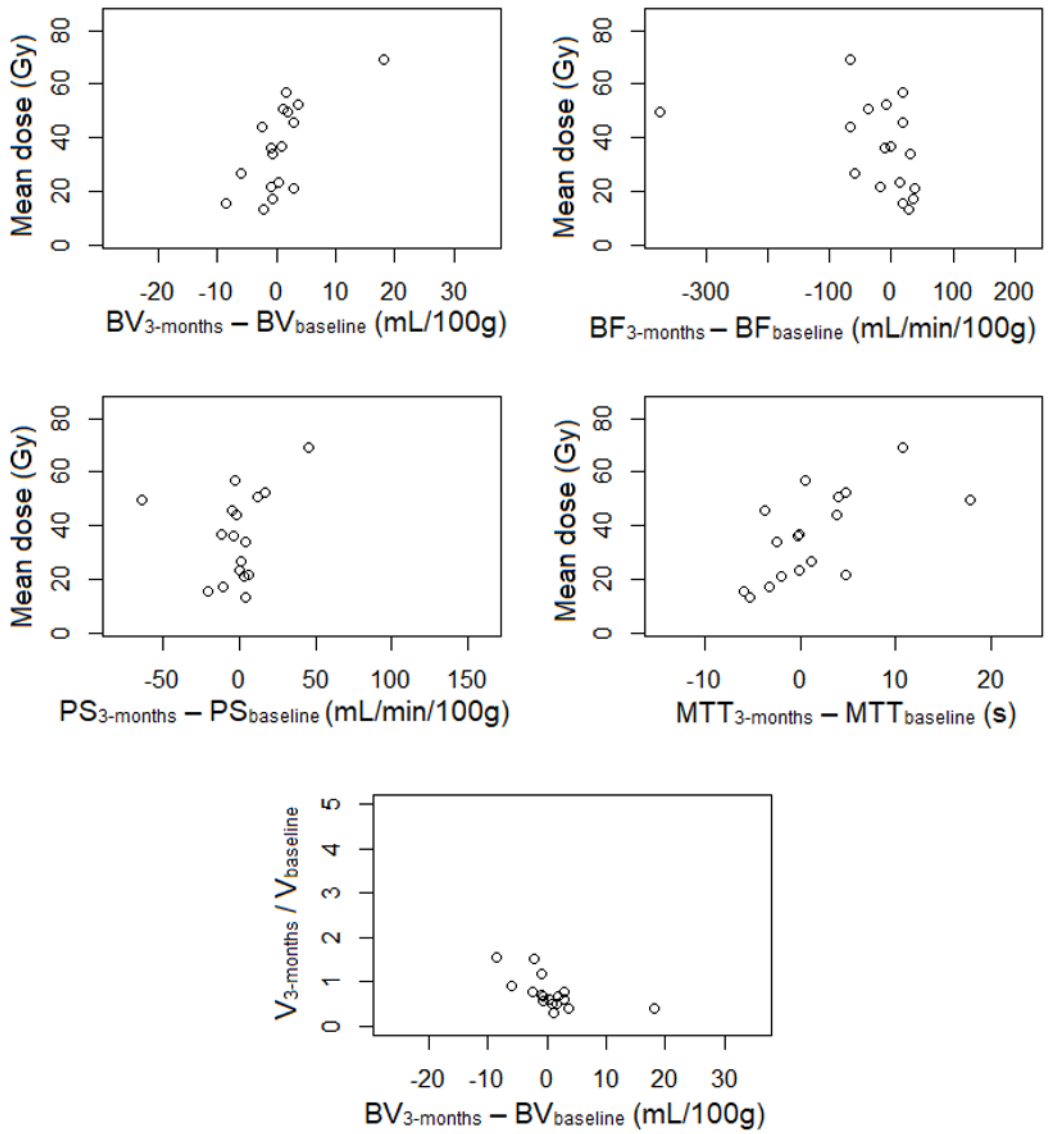

Figure 4.5-6 Assessment of change at three-months follow-up from baseline from various pCT metrics against deposited mean dose to tumours and volumetric response at three-months follow-up.

4.6 Summary

This chapter investigated the dose-response relationship of ^{90}Y SIRT in a cohort of CRC patients. Clinical dosimetry was further augmented with radiobiological modelling in the form of BED and EQD based on the findings from ^{90}Y radiosensitivity characterisations

of CRC cell lines from Chapter 3. Finally, liver perfusion imaging (DCE MRI and pCT) metrics were explored as an indicator of tumour dose deposition or volumetric response from ^{90}Y SIRT to capture additional clinical factors relevant to this vascularly-delivered treatment.

5 Assessment of combined external beam radiotherapy and ^{90}Y microsphere radiotherapy in hepatocellular carcinoma patients

The central aim of the work reported in this Chapter was to expand on the application of ^{90}Y SIRT radiobiological modelling from Chapters 3 and 4 to another patient cohort and to demonstrate its applicability for more complex and real-world radiotherapy treatment scheduling. Specifically, in the case where a patient may have had prior external beam radiotherapy, consideration of the variation of response to different modalities and fractionation regimens would provide considerable clinical utility. In this chapter, these issues are explored in a pilot cohort of 10 patients with hepatocellular carcinoma (HCC) that received both ^{90}Y SIRT and palliative EBRT. In the final Section, this Chapter also investigates the merits of intentionally combining ^{90}Y SIRT and SABR based on SIRT and radiobiologically-informed virtual treatment plans created post hoc. This Chapter serves as preliminary evidence that ^{90}Y SIRT and EBRT can be used together to achieve better outcomes from a dosimetric perspective, than from either one alone.

5.1 Patients

The baseline characteristics of the ten HCC patients who received both ^{90}Y SIRT and EBRT at the time of their initial presentation are summarised in Table 5.1-1. None of the patients had any prior TACE, RFA, chemotherapy, or vascular procedures. Survival of the cohort was followed for several months from the first course of radiotherapy. Because more than half of the patients survived or were censored at the time of analysis, mean and

median survival could not be directly calculated. Instead, mean survival was estimated as 15 months in Figure 5.1-1.

Table 5.1-1 Patient baseline characteristics at consult (n=10).

Characteristic	**N (%)** or **mean ± standard deviation**
Gender/Sex	
Male	8 (80%)
Female	2 (20%)
Age (y)	61 ± 10
Height (m)	1.8 ± 0.12
Weight (kg)	82.8 ± 24.3
[a]Individual tumour volume (mL)	965 ± 1242
[b]Tumour burden (%)	46 ± 21
<25%	1 (10%)
25-50%	4 (40%)
>50%	5 (50%)
[c]Total tumour volume (mL)	1737 ± 1226
Extrahepatic metastases	
Lung	1 (10%)
Prostate	1 (10%)
Rectum	1 (10%)
Lymph node	1 (10%)
Prior therapies	
Chemotherapy	0 (0%)
Radiation	0 (0%)
Ablation	0 (0%)
Hepatectomy	1 (10%)
Portal vein occlusion	3 (30%)
Hepatitis B	0 (0%)
Hepatitis C	6 (60%)
Number of tumours per patient	
1	4 (40%)
2	4 (40%)
3	2 (20%)

[a]Including all tumours across all patients

[b]Percentage (%) of the whole liver occupied tumour

[c]Sum volume of the tumour contours from the first CT scan prior to radiotherapy

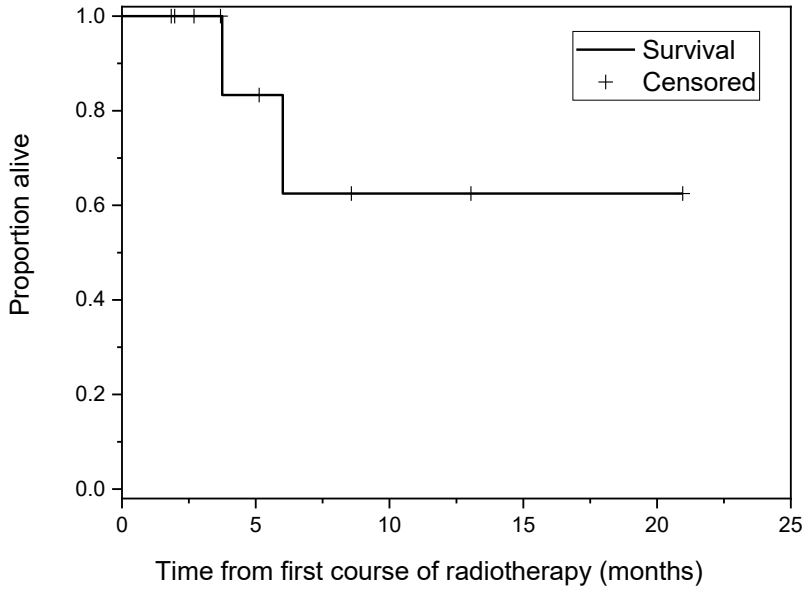

Figure 5.1-1 Survival curve of the HCC cohort that received EBRT and ^{90}Y SIRT treatments.

Most patients were censored as alive at the time of their most recent follow-up. The mean Kaplan-Meier estimated survival was 15.0 months (95% CI 8.3-21.6 months), however this was underestimated as the longest survival observation was censored.In most cases, EBRT treatments were delivered prior to ^{90}Y SIRT with the intention of relieving pain secondary to large hepatic tumours. EBRT was usually selected for initial palliation as it avoids the week-long workup preparation required for the ^{90}Y SIRT procedure. However, only one of the patients had small enough tumours to be considered for SABR. ^{90}Y SIRT followed the EBRT treatment as it is generally well-tolerated and EBRT alone did not achieve cure in any of the patients. The order of the two treatments was reversed in two patients who received SIRT before EBRT, and this was because they met criteria for liver-directed therapy (^{90}Y preferred over TACE due to lower toxicity profile). Both patients' treated disease showed clinical responses, but hypovascular disease areas had poor microsphere

uptake. Thus, a decision was made to proceed to EBRT in an effort to maximise therapeutic efficacy.

5.2 Volumetry

Volumes were measured from all segmented tumour contours on all available pre- and post-treatment scans to capture the outcome of the delivered EBRT and SIRT treatments. Due to the variable timing among the patients, the EBRT and ^{90}Y SIRT portions of the treatment schedules were considered separately. Figure 5.2-1 illustrates the evolution of tumour volume change for all tumours throughout each patients' treatments relative to their baseline imaging timepoint. For EBRT treatments, baseline was defined as the planning CT. For ^{90}Y SIRT, the last scan acquired before ^{90}Y SIRT was defined as baseline. The majority of EBRT-treated tumours did not increase in tumour volume, though some did not reduce in volume, likely because the dose delivered was modest as the treatment was given for palliation. The small number of tumours that did increase in volume did not fall in the EBRT treatment volume, as they were smaller satellite lesions that were thought not to be contributing to symptoms. Baseline was also chosen as the reference timepoint because the timepoint immediately following SIRT may be associated with inflammation or hypertrophy. This could bias the results to 'appear' as better response than true response. Even with this under consideration, the majority of tumours decreased in size in the months following the baseline scan. Patient TN005's worst-responding tumour (Figure 5.2-1C, Tumour 2) had the highest additional tumour doses from EBRT (mean EBRT dose 39.56 ± 11.23 Gy). Tumours 1 and 3 had partial volume reduction with lower tumour doses from the additional EBRT treatment (mean EBRT doses of 6.38±3.37 and 11.41±1.48 Gy, respectively). Inflammation following ^{90}Y SIRT administration potentially biases the measured % volume change at the first timepoint. A differential response to SIRT was

noted. For example, tumour 2 in study subject TN005 progressed following SIRT while tumours 1 and 3 regressed.

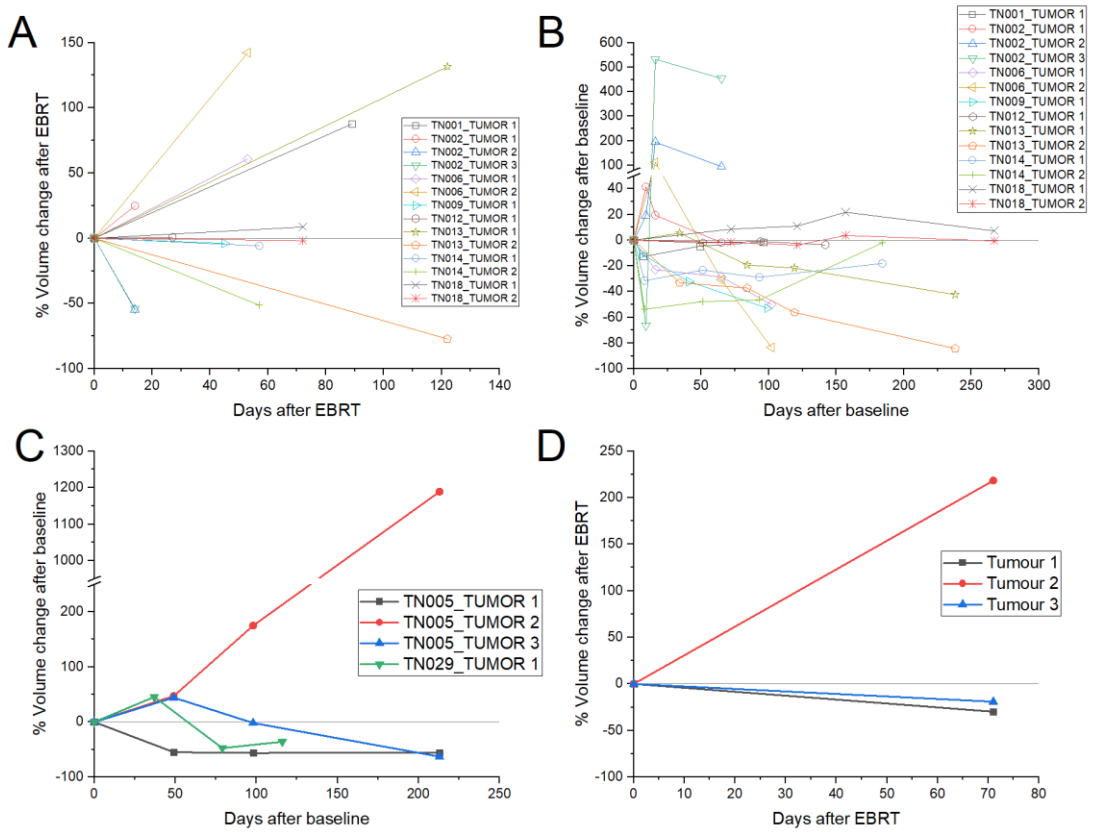

Figure 5.2-1 Change in HCC tumour volume over time according to treatment scheduling. Tumour volumes were tracked as a function of time based on available imaging. Tumour volume was measured relative to baseline, and so, all tumour volume curves pass through the origin. The grey horizontal line at 0% represents the threshold for tumour shrinkage or enlargement. (A) The change in volume of 14 tumours over time in 8 patients that received EBRT prior to ^{90}Y SIRT treatment illustrated variable response up to the time that SIRT was given. The tumours which greatly increased in volume were not targeted by EBRT. (B) The percentage volume change of tumours from ^{90}Y SIRT illustrated that most tumours reduced in volume following treatment. This could be attributed to the targeting of all tumours from the ^{90}Y treatment, which was not the case for EBRT treatments. (C) The

change in tumour volume in the two patients that received SIRT, prior to EBRT. (D) Change in tumour volume for only patient TN005 who received EBRT after having already received SIRT. Uniquely, tumour 2 progressed after both therapies, whereas the others did not, suggesting that this tumour may have been more radioresistant. While patient TN029 also had EBRT after SIRT, they had no imaging following EBRT and only one tumour to consider, so was excluded from this figure.

5.3 Dosimetry

All tumours were contoured on baseline and post-treatment scans. All contours were validated by an independent radiologist, Robert Young (Sarah Cannon, Nashville, TN). Differences between volumes previously contoured during EBRT planning and the new contours were apparent from the DVHs. For example, in the TN029 case, part of the new tumour contour was outside the EBRT fields, which were planned based on the previous contours. While the original EBRT dosimetry was preserved, new contours were drawn due to missing tumours, which were not targeted by the plan, and to reduce inter-operator error. This difference in contour definitions resulted in less favourable treatment plans, which was apparent from nonuniformity artefacts in the DVHs.

Absorbed doses were measured according to the body-based method (MIM SurePlan default configuration) and compared with those calculated using the same liver-based method as presented in Chapter 4 (Figure 5.3-1). The body-based method differed as administered activity was equated to the total signal due to ^{90}Y in the body contour as opposed to signal within the liver contour only from the Chapter 4 method, described in Section 2.3.4.1 on page 38.

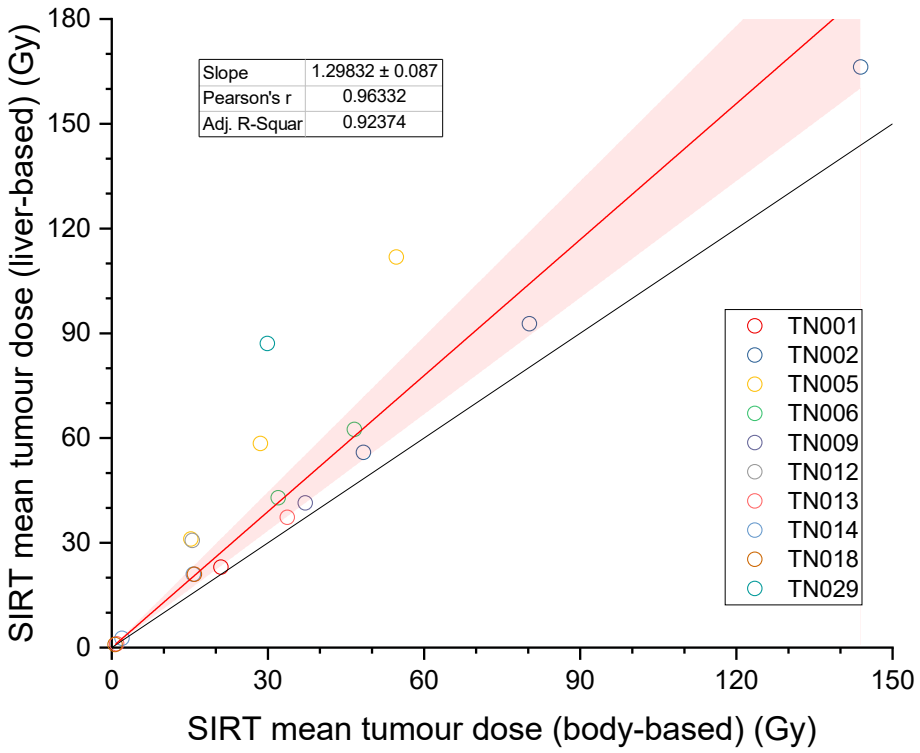

Figure 5.3-1 Comparison of mean individual tumour doses measured using the body-based method (MIM default) versus the liver-based method (as used in Chapter 4). The linear regression line with 95% confidence band is shown in red and the black line indicates dose equivalence.

Dose-response effect is an established cornerstone of EBRT and, although this cohort was treated with palliative intent and, therefore, the prescribed dose was low, the relationship between dose and effect was investigated. To assess whether EBRT dosimetry was predictive of response, the percent change in tumour volume was plotted against mean absorbed dose to each tumour (Figure 5.3-2A). The fit line trended as expected with a 7.6% decrease in tumour volume per Gy of absorbed dose which was statistically significant ($p=0.028$). Dose-response effect was also tested for ^{90}Y SIRT (Figure 5.3-2B) at each of the timepoints with available tumour follow-up volumetry. The dose values from this analysis disregarded the EBRT dose history and no statistically significant relationship

was observed. However, the mean volume change at the first and second follow-up timepoints were shown to be statistically significantly different from 0%.

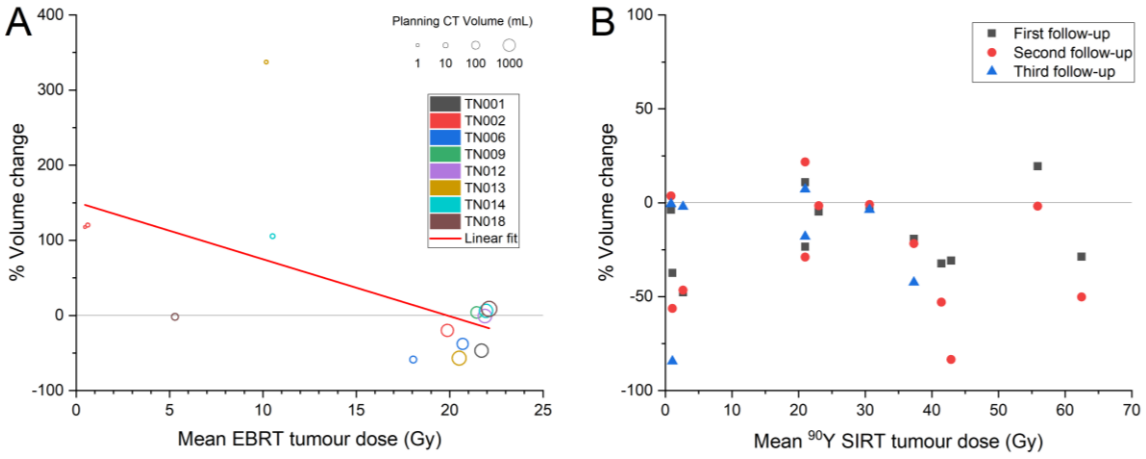

Figure 5.3-2 EBRT and SIRT dose-response. The relative change in tumour volume following either EBRT or SIRT was plotted against mean dose to identify any trends in dose-response relative to either treatment modality. Analysis of the combined dose-response is further analysed in Section 5.6. A line at 0% volume change represents the threshold for increasing versus decreasing tumour volume. The linear regression analysis did not account for clustering of tumours within patients and the ^{90}Y SIRT first group (patients TN029 and TN005) were excluded. (A) EBRT demonstrated a statistically significant (red line, p=0.028) slope of decrease in tumour volume change of 7.6% per Gy of EBRT dose. The cluster of tumours with mean tumour doses above 17 Gy were all included in the EBRT Planning Treatment Volume (PTV). No tumour showed complete response, but all targeted tumours were either stable or reduced in volume, which reflects the palliative intent of the therapy. (B) ^{90}Y SIRT dose did not achieve a statistically significant slope of dose against % volume change for any of the first, second, or third follow-up timepoints (p=0.51, p=0.61, p=0.81, respectively). This could be due to the prior treatment with EBRT complicating the dose-response relationship as prior doses were not considered. This analysis excluded two outlier tumours with volumes <10 mL, absorbed doses above 70 Gy, and % volume changes >90%. However, t-tests indicated mean response of

individual tumours at first, second, and third follow-up timepoints -17% (p=0.017), -26% (p=0.014), and -21% (p=0.14). The first and second follow-up volumes were statistically significantly different from 0% change in volume. Although its implications are limited by the confounding EBRT dose, these findings suggests there is a therapeutic benefit of the ^{90}Y SIRT treatment regardless of absorbed dose.

5.4 External beam radiotherapy

EBRT is well-known to have increasing efficacy with increasing dose. However, owing to the large tumour volumes and risk of radiation-induced liver toxicity in a group of patients with generally poor performance status, apart from one SABR case, palliative regimens using 3 Gy fractions were employed (details in Table 5.5-1). Half the patients experienced minor early complications while none experienced Grade 3 or 4 toxicity, e.g. liver decompensation.

Table 5.4-1 Details of EBRT treatment (n = 10).

Characteristic	**N (%)** or **mean ± standard deviation**
Individual tumour volume (mL)	969 ± 1239
SIRT treatment prior	2 (20%)
EBRT schedule	
7 fractions of 3 Gy	8 (80%)
6 fractions of 3 Gy	1 (10%)
5 fractions of 10 Gy	1 (10%)
Elapsed treatment time (d)	8.6 ± 1.1
Target site	
Whole liver	6 (60%)
Right lobe	3 (30%)
Segment II	1 (10%)
Early complications	
None	5 (50%)
Pain	4 (40%)
Nausea	3 (30%)
Fatigue	1 (10%)
Other	2 (20%)

A detailed summary of all EBRT treatments is shown in Figure 5.4-1 and Figure 5.4-2. Patients selected for treatment with EBRT prior to SIRT had a dominant, large tumour accounting for the majority of the tumour burden. In general, the smaller satellite tumour masses were not targeted in the EBRT plan.

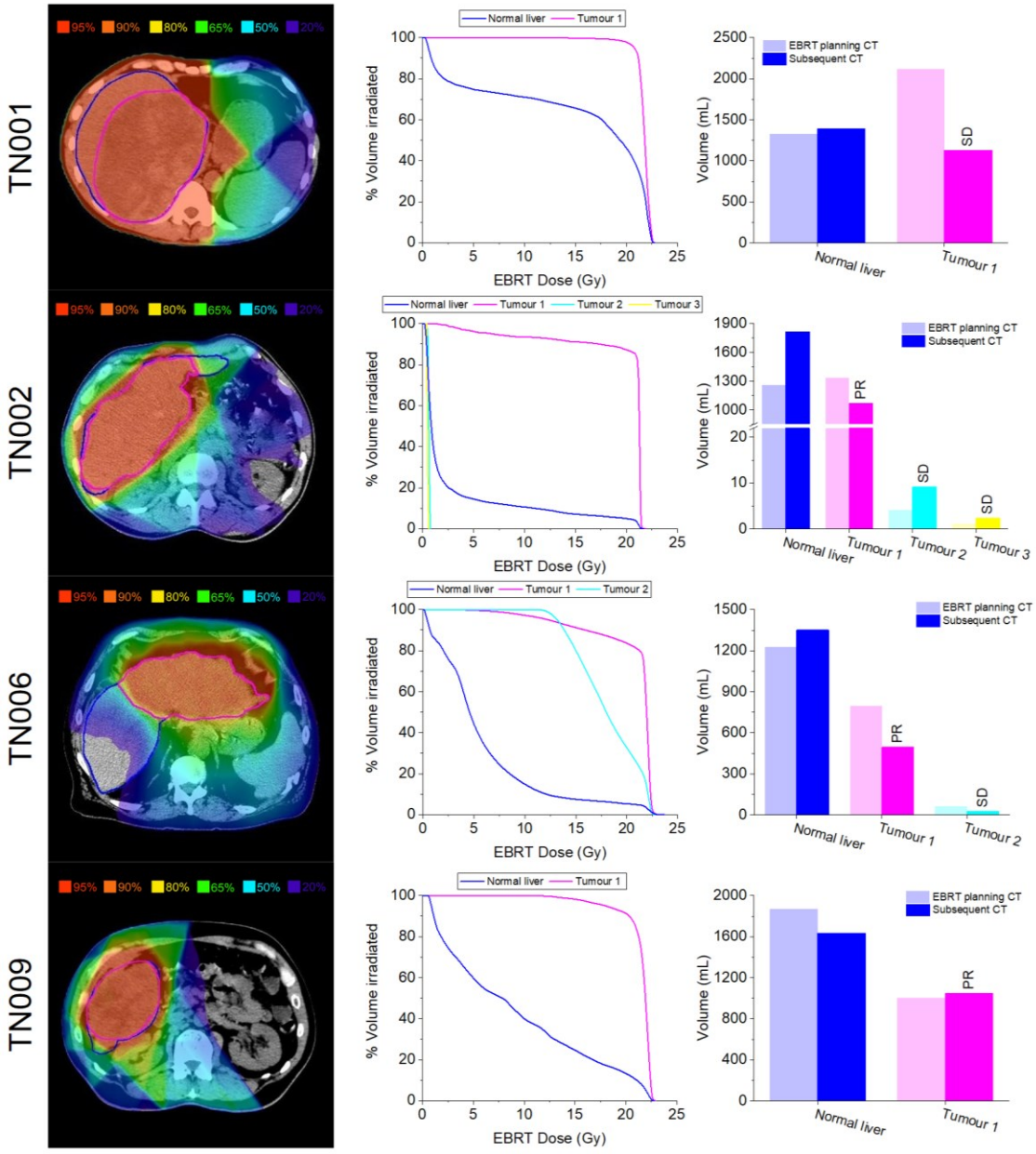

Figure 5.4-1 EBRT in patients who had EBRT before ^{90}Y SIRT. (figure continued on next page) Radiotherapy plans are shown for each patient (one per row) as follows: EBRT dose map (left), the DVH for normal liver and individual tumours (middle), and normal liver and

individual tumour volumes at baseline and follow-up (right). The EBRT dose map shows a single section through the main tumour, denoting dose according to the percentage of the total prescribed dose. Above each bar is the reported radiological response at the respective timepoint relative to the first bar.

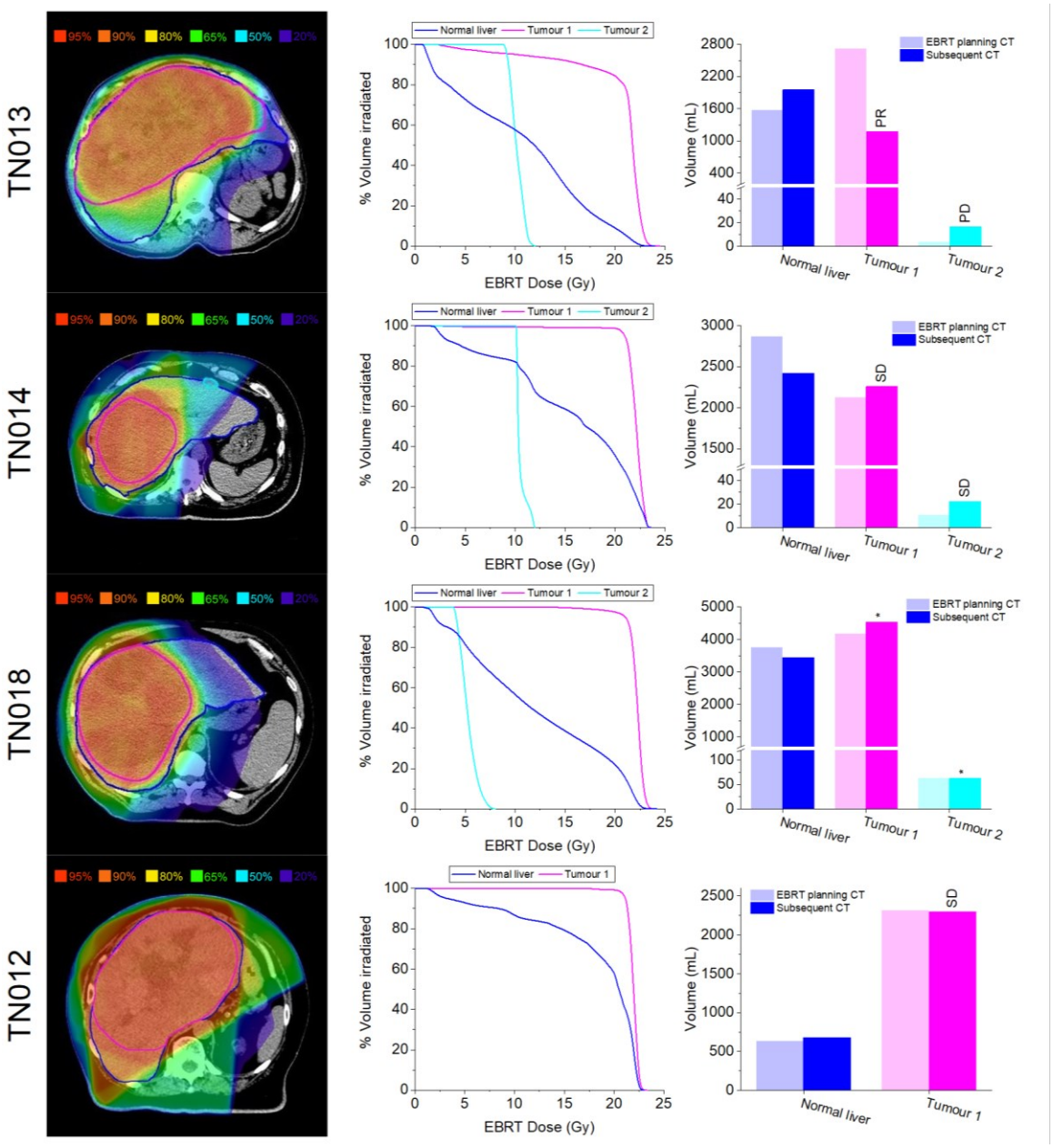

Figure 5.4-1 (continued) **EBRT in patients who had EBRT before ^{90}Y SIRT.**

* Radiological response not reported as no prior CT imaging was available

The ^{90}Y SIRT-first cases (TN005 and TN029) had lower tumour burden than the EBRT-first group (TN001-2, TN009, TN012-014, and TN018). The smaller tumours were generally not targeted by EBRT and this is evident in the DVH column, which is coloured to match the contour. The tumour volume plots, also coloured to match the contour, illustrate the raw data used to measure percentage change in volume between timepoints, which is utilised in subsequent analysis.

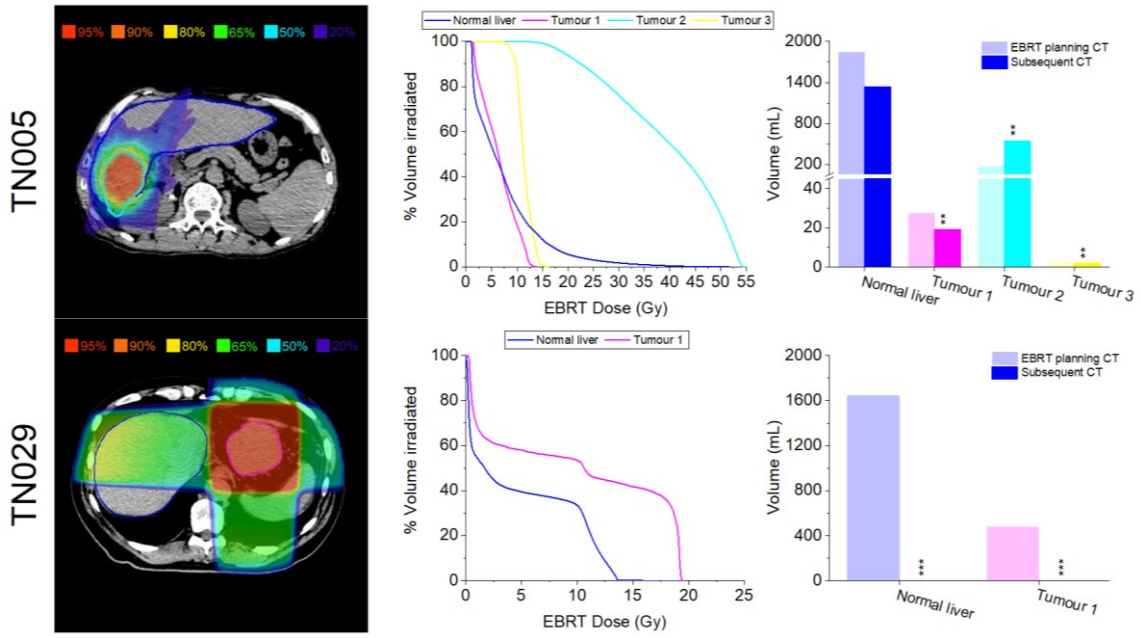

Figure 5.4-2 EBRT in patients who had ^{90}Y SIRT first. Radiotherapy plans are shown for each patient (one per row) as follows: EBRT dose map (left), the DVH for normal liver and individual tumours (middle), and normal liver and individual tumour volumes at baseline and follow-up (right). The EBRT dose map shows a single section through the main tumour, denoting dose according to the percentage of prescribed dose (50 Gy for TN005 who was prescribed SABR and 21 Gy for TN029). Above each bar is the reported radiological response at the respective timepoint relative to the first bar.

** Radiological response not reported as no prior CT imaging was available

*** Radiological response not reported as only baseline CT imaging was available

5.5 ^{90}Y microsphere radiotherapy

The second hypothesis was that the distribution of ^{90}Y SIRT dose would predict response. This was demonstrated already in Section 4.3 for CRC patients and several other recent studies supported this conclusion (*20*,*27*). However, the patients presented here represent a distinct group as they were treated at a different centre, had a different primary, and had prior EBRT, all of which could alter the outcomes. There were no procedure administration complications and none of the patients experienced liver decompensation, although half the patients experienced minor early side effects, e.g. pain, nausea, and fatigue (see Table 5.4-1 on page 99). Further details about the SIRT treatments are provided in Table 5.5-1.

All tumours were targeted in all ^{90}Y SIRT treatments, as opposed to segment ablation. A detailed summary of all SIRT treatments is shown in Figure 5.5-1 and Figure 5.5-2. Two cases were treated with EBRT afterward (i.e. SIRT first), which means they had no prior therapies and so would not be comparable with the majority of the patients in the cohort. These cases were considered separately.

As evident in the DVH column, which is coloured to match the contour, most tumours achieved higher absorbed dose from SIRT than did the normal liver, as expected to achieve therapeutic effect. The tumour volume plots, also coloured to match the contour, illustrate the raw data used to measure percentage change in volume between timepoints, which is utilised in subsequent analysis. Above each bar is the reported radiological response at the respective timepoint relative to the first bar at baseline.

Table 5.5-1 Patient ^{90}Y SIRT treatment characteristics (n = 10).

Characteristic	**N (%)** or **mean ± standard deviation**
Individual tumour volume (mL)	803 ± 1166
EBRT treatment prior	8 (80%)
Target site	
Right lobe	2 (20%)
Left lobe	2 (20%)
Whole liver	6 (20%)
[a]Lung shunt (%)	7.3 ± 4.7
Body surface area (m^2)	1.86 ± 0.32
Administered activity (MBq)	1934 ± 293
Complications	
None	5 (50%)
Fatigue	2 (20%)
Nausea	1 (10%)
Pain	3 (30%)
Other	3 (30%)

[a]Data missing for one patient

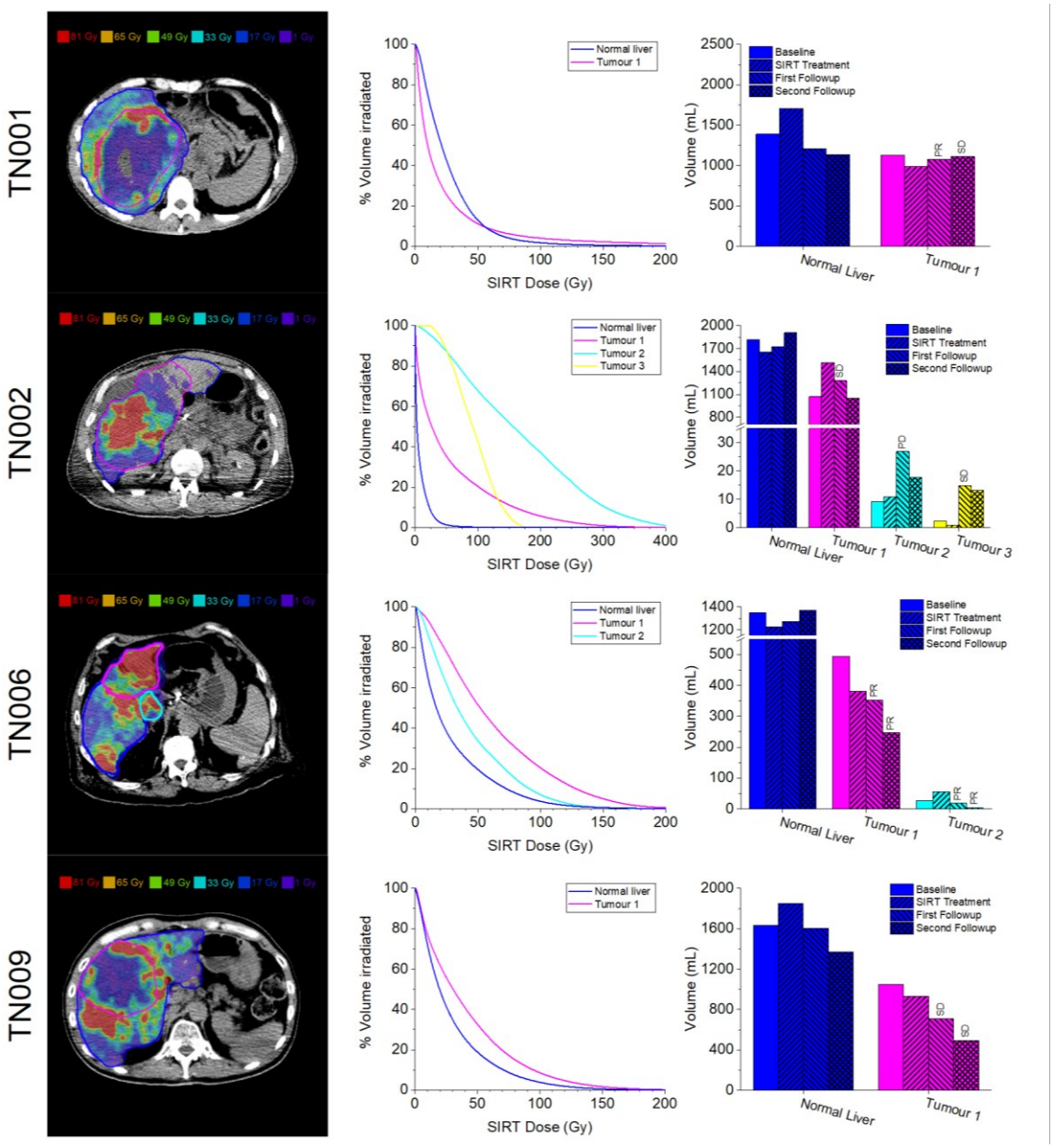

Figure 5.5-1 SIRT in patients who had EBRT first (figure continued on next page) Each patient case (one per row) was broken down into the SIRT dose map (left), the SIRT DVH to normal liver and individual tumours (middle), and measurements of absolute normal liver and individual tumour volumes at each reference timepoint (right). The SIRT dose map column represents a single slice from the treatment PET/CT (or SPECT/CT) and superimposed dose map, denoting dose according to the percentage of deposited dose.

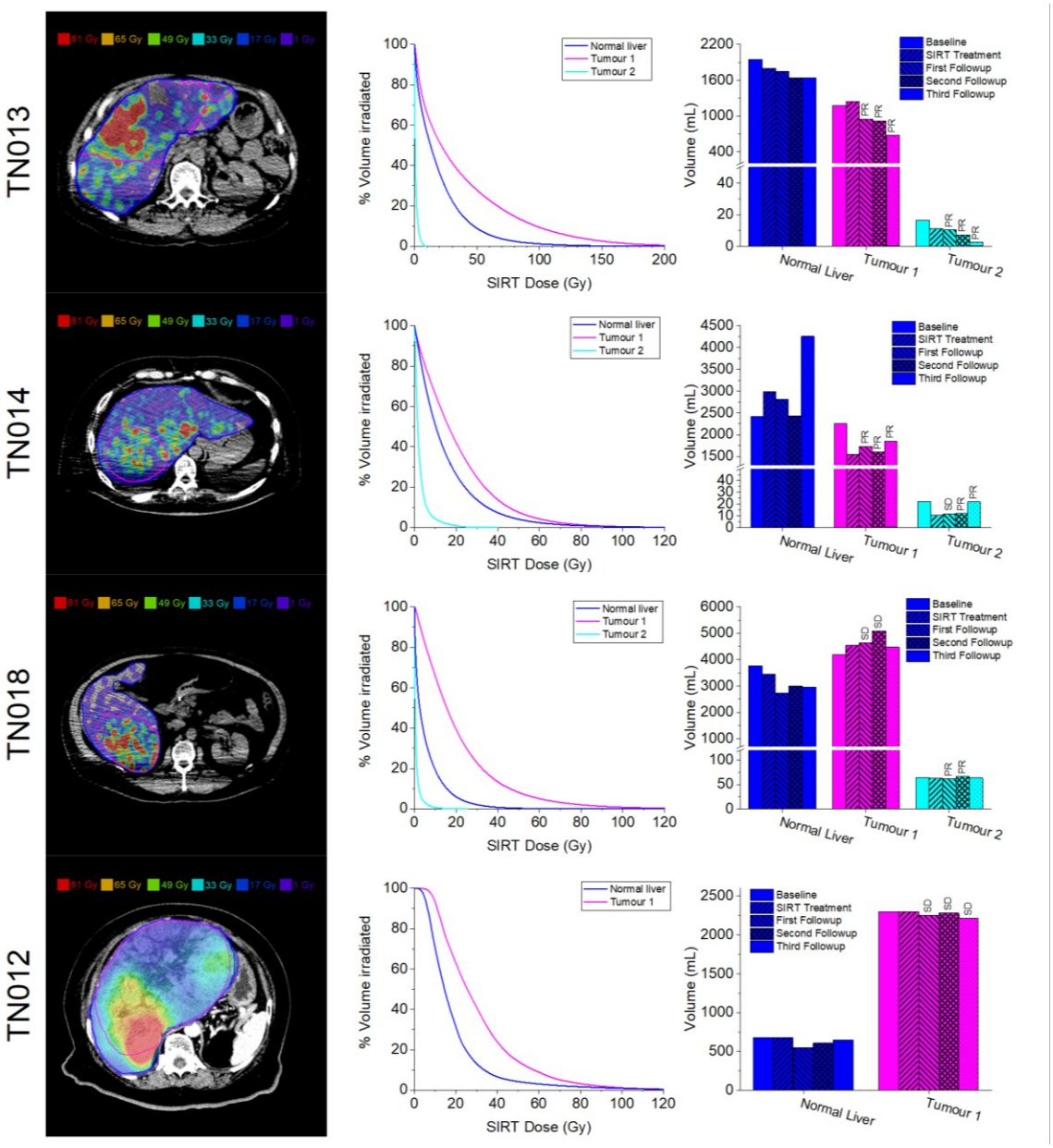

Figure 5.5-1(continued) **SIRT in patients who had EBRT first**

The ^{90}Y SIRT-first cases (TN005 and TN029) had lower tumour burden than the EBRT-first group. Above each bar is the reported radiological response at the respective timepoint relative to the first bar.

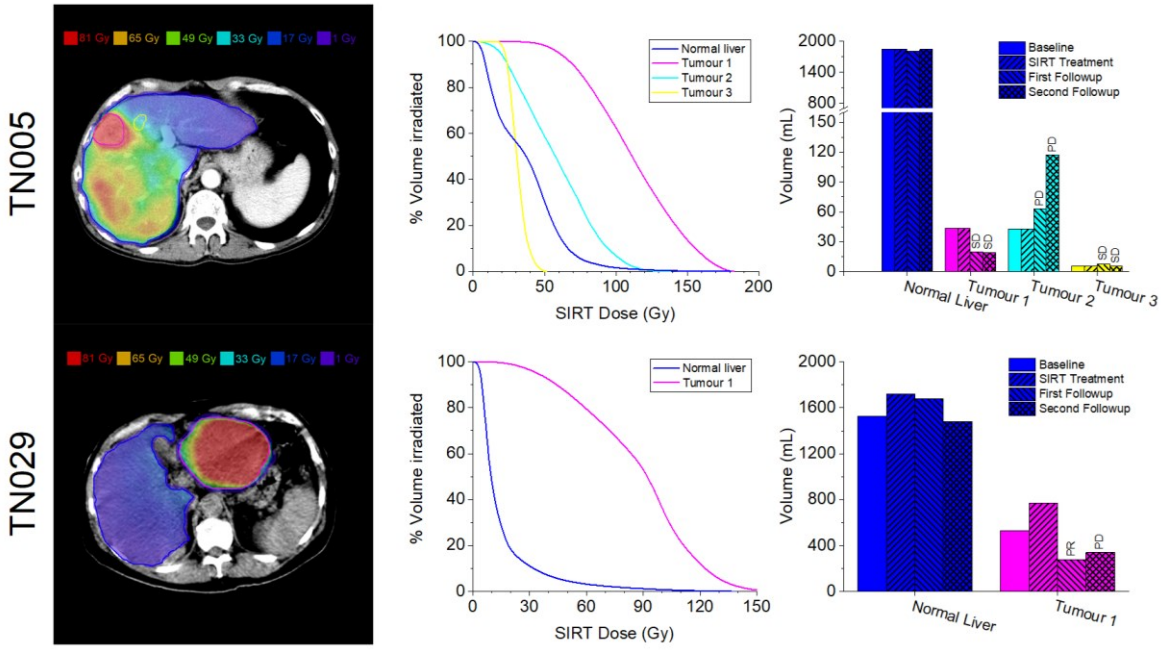

Figure 5.5-2 SIRT in patients who had ^{90}Y SIRT first. Each patient case (one per row) was broken down into the SIRT dose map (left), the SIRT DVH to normal liver and individual tumours (middle), and measurements of absolute normal liver and individual tumour volumes at each reference timepoint (right). The SIRT dose map column represents a single slice from the treatment PET/CT (or SPECT/CT) and superimposed dose map, denoting dose according to the percentage of deposited dose. Radiobiological modelling

5.6 Combination SIRT and EBRT

It was hypothesised that sum BEDs could be used to describe the combination of EBRT plus SIRT. BEDs were calculated (in the same BED units) independently for the EBRT treatment and for ^{90}Y SIRT treatment as described in Section 2.2.1. Owing to the lack of data to describe repopulation dynamics, no term for repopulation was included in the BED models. The voxelised dosimetry process lent itself to calculating sum BEDs in two ways. The first, involved performing the dosimetry and BED calculations and then summing the doses independent of spatial information, i.e. summing the BED histograms. The second method included voxel-wise dosimetry whereby voxels from each the dosimetric outputs

of each treatment were associated with their respective location in the patient. Although potentially simpler to add BED histogram or summary statistics, it was considered that true BEDs were best captured by attempting the summation on a voxel-by-voxel basis. Additionally, modern conformal treatment planning would surely account for the ^{90}Y SIRT voxelised doses in the EBRT planning process. Consideration of prior radiotherapy from ^{90}Y was done in the two SIRT-first patient cases and the 40 Gy physical dose was chosen as the maximum tolerated dose to normal tissue. The 40 Gy dose was based on the normal tissue constraint used in planning from the clinical experience of Andrew Kennedy (radiation oncologist, Sarah Cannon).[2] No radiobiological calculations were performed at Sarah Cannon so an approach of calculating BEDs could offer a more-systematic justification for appropriating dose thresholds. The challenge to sum individual voxels was then the question of how to identify which voxels from each timepoint were associated. Misregistration is possible as scans were not acquired in the same time or manner. For example, SPECT/CT images required a longer exposure duration so deep inspiration breath hold was not feasible for the patients. The adopted approach involved a contour and intensity-based deformable registration algorithm in MIM. Part of the MIM workflow included a deformable registration step with respect to the whole liver and to tumour contours so that doses from both therapies could be directly accumulated. Organs at risk (OARs) were not included in the algorithm due to the added computational demands. Consequently, voxels for OARs may not have aligned well. However, the MIM version 6.9.4 dosimetry algorithm did not compute ^{90}Y doses outside of the liver, excluding OARs and resulting in sum BED values were then equal to EBRT BED.

[2] The recommended 40 Gy threshold was confirmed through direct personal communication.

The BED maps calculated from EBRT plus ^{90}Y SIRT dosimetry along with the sum BED map are illustrated in Figure 5.6-1 with two exemplar patients. Differential histograms of each treatment for all patients are given in Figure 5.6-2

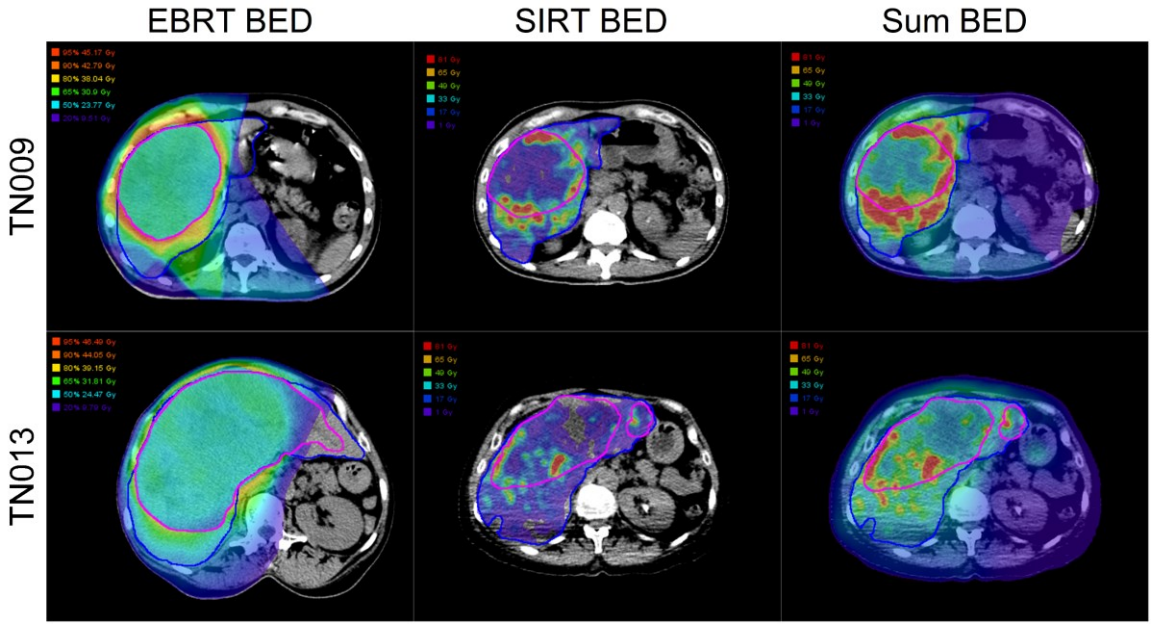

Figure 5.6-1 BED maps for two example patients (TN009 and TN013). The first, second, and third columns illustrate the calculated BED from the EBRT, ^{90}Y SIRT, and the accumulated BEDs from each determined by summation of the BEDs through a deformation matrix determined using a contour and intensity-based algorithm in MIM. The SIRT and sum BED columns were given different scaling to aid in visualisation of the areas treated with more than the 40 Gy physical dose constraint to normal tissue. BED values inside the tumour had differing scaling than the normal tissue owing to their differing radiosensitivity parameters.

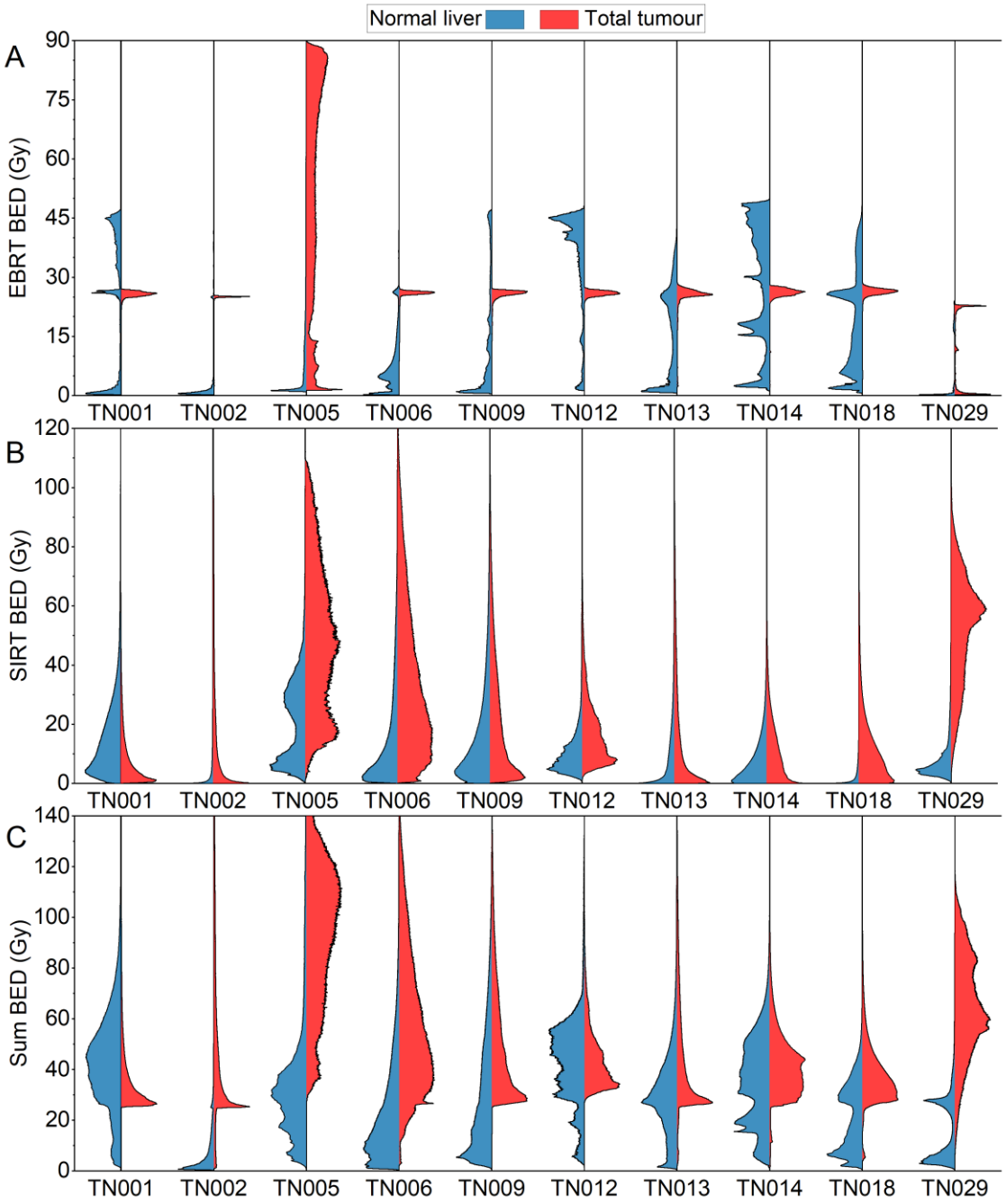

Figure 5.6-2 Differential BED histograms. Cumulative DVH outputs from MIM were differentiated to produce dose frequency distributions. Widths for normal liver and total tumour from each patient were normalised to the maximum frequency value to illustrate the distribution of different doses values in the patients. (A) BED distributions for each patient illustrated dose deposition in normal liver and all tumour tissues from EBRT. For the EBRT-first patients, BEDs achieved uniform and complete coverage in tumour and achieved mean BED values of at least 25 Gy. (B) BED distributions for each patient's ^{90}Y

SIRT treatment. Dose deposition was considerably more heterogeneous than in EBRT and varied considerably between patients. Despite high normal liver uptake, the patients tolerated ^{90}Y SIRT well. Patients TN005, TN012, and TN029 had SPECT-based dosimetry. Due to the 'blurring'-effect from the bremsstrahlung signal recovery, their lowest BED voxels appear greater than the other patients' with PET-based dosimetry. (C) The Sum BED histograms were generated from voxel-wise addition of biological effect-adjusted dose values. The apparent 'shelf' where tumour doses begin at around 25 Gy was a result of the good coverage from EBRT guaranteeing that all tumour voxels achieved a minimum BED. The combined therapy offered the advantage of providing a near threshold minimum doses to tumour tissue.

5.7 External beam planning after ^{90}Y microsphere radiotherapy

The aim of a separate EBRT planning exercise was to determine whether there is merit in intentionally combining ^{90}Y SIRT and SABR therapies. Two sample patients were selected for this dose planning exercise for a curative SABR. An important caveat was that, although most previously reduced in volume from EBRT, these tumours were larger than those which would typically be treated by SABR. The aim was for the patients to be selected to represent the wider population that might be candidates for ^{90}Y SIRT followed by SABR. To appreciate the variability in tumour presentations, the selected patients were not those that had highly specific uptake of ^{90}Y to tumour tissue, but included a case (TN009) where there was moderate uptake to normal tissue and only peripheral tumour uptake, and another case (TN013) where there were multiple lesions with differing average uptake values.

Doses and fractionation were selected according to the Radiation Therapy Oncology Group (RTOG) randomised phase III study of sorafenib versus SABR followed by sorafenib in HCC (RTOG 1112). Dose constraints were adopted from treatment protocols used at Sarah Cannon Research Institute (Nashville, TN). These protocols recommend a maximum dose of 40 Gy to normal liver from ^{90}Y SIRT to avoid RILD and considered against 30 Gy from which a uniform dose of 2 Gy/fraction conventional EBRT is the accepted threshold dose to cause RILD (*92*). However, owing to differences in radiobiological effects, ^{90}Y and EBRT physical doses are not directly comparable. The ^{90}Y doses considered in the plan would instead be based on a different value determined as the EQD for the delivery of 5×10 Gy fractions. Plans were normalised to give 95% of the target 100% of the prescription while sparing 700 mL of normal liver. EQD base doses were determined from the MIM default body-based dosimetry approach using the radiobiological modelling parameters mentioned in Section 3.3 on page 63. However, due to a lack of beam sequence data, the Eclipse planning software was unable to consider the voxelised EQDs from ^{90}Y SIRT as a base dose. Instead, a solution using a threshold maximum dose to normal liver (α/β = 3 Gy) only was determined from the dose constraints mentioned above. As the tumour tissue has different radiobiological parameters and improved control is expected above the prescribed EBRT dose, maximum dose constraints to tumour tissue were not required. The normal liver constraints were converted from 40 Gy ^{90}Y physical dose to the EQD threshold of 7 Gy as follows.

$$EQD = \frac{BED'_{LINAC}}{RE_{LINAC}}$$

$$= \frac{RBE_{max} \times D_{90Y}}{1 + \frac{D_{LINAC}/n}{(\alpha/\beta)_{LINAC}}}$$

$$= \frac{0.6 \times 40\ Gy}{1 + \frac{40\ Gy/5}{3\ Gy}}$$

$$= 6.54\ Gy \approx 7\ Gy$$

The denominator offered a challenge due to the threshold requirement and by not using ^{90}Y EQD as a base dose. The voxelised values would mean that each voxel would have a different dose value. Because that was not possible using the threshold technique, 40 Gy in the denominator was decided for the 5×10 Gy plan since it would conservatively overestimate the physical dose to normal liver (not expecting to achieve the uniform 50 Gy from EBRT, while remaining conservatively above the mean dose to normal liver. Some subjectivity was required when using a threshold value (as opposed to base dose) for the LINAC dose value D_{LINAC} of the RE term in the denominator of the EQD equation. The determined threshold EQD was rounded to 7 Gy. The resultant boundary of 7 Gy from ^{90}Y EQD was sufficiently large to allow some areas of normal liver to have EBRT added. The less conservative estimate of using 30 Gy in the denominator resulted in a boundary for additional dose which was 8 Gy leaving room for more dose to pass through normal liver. A more conservative estimate using 50 Gy total dose to normal liver in the denominator (which is unrealistic as the DVHs showed an average dose around 25 Gy) achieved a dose of 5.54 Gy covering a larger area of the normal liver and allowing for less dose to pass through the normal liver. For comparison, the standard uniform normal liver dose threshold of 30 Gy from 2 Gy/fraction EBRT has a BED of 50 Gy. Consequently, these estimates would be 11.5 or 16.7 Gy, which errs to the more conservative side, however these values were for uniform irradiation and normal liver is known to be more tolerant to heterogenous SIRT dose than to uniform liver dose from EBRT. Therefore, 40 Gy was a reasonable value to balance the benefits and disadvantages of either the more- or less-conservative approach.

Finally, to assess feasibility, multiple plans were prepared by the dosimetrist Kimberly Mitchell (Sarah Cannon, Nashville, TN) in the same clinic where these patients were

treated. For TN009, a SABR plan was created with the constraints defined above. Adding ^{90}Y dosimetry into the planning process, including ^{90}Y dose in all tissues resulted in a categorically inferior plan because the mean normal liver dose was nearly 10 Gy higher. When considering ^{90}Y dose within only the normal liver and neglecting ^{90}Y dose within the targeted tumour tissue, it made a difference as it reduced the constraints on the optimisation algorithm because existing ^{90}Y doses contributed against the normal liver constraints. This optimisation algorithm decreases dose to normal liver as much as possible regardless of what prior dose it received, the normal liver was found to be very similar. From this approach, less volume of normal liver received higher doses but more volume received lower doses, which can be typical when trying to reduce hot areas. In this way, and in achieving more uniform coverage, the plan which did not take ^{90}Y dose into account was the better plan because of the improvised isodose contour constraints on normal liver dose. This was a negative result for the hypothesis that planning EBRT around a ^{90}Y treatment would achieve better DVHs and could explains why this approach is not typically taken. TN009 was planned including the additional approach of a lower dose line from ^{90}Y, resulting in a larger volume with which the optimisation algorithms could operate. Figure 5.7-2 illustrates the EBRT doses from these approaches to various tissues of interest.

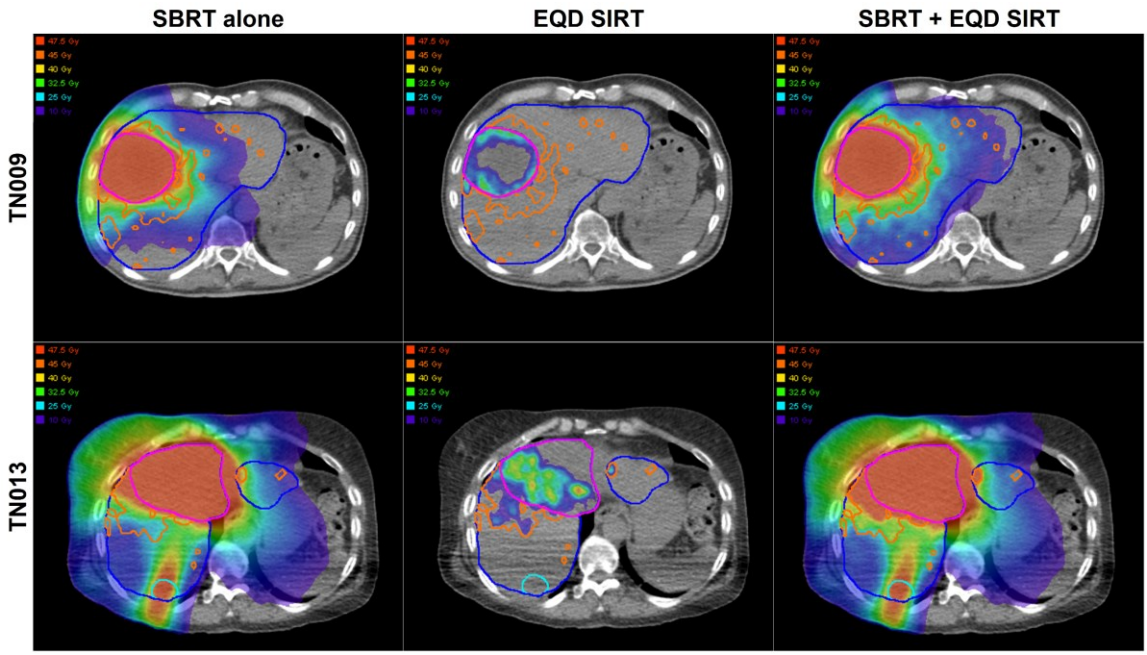

Figure 5.7-1 SABR plans for patients TN009 (top row) and TN013 (bottom row). Contours representing the liver (blue), tumour 1 (magenta), tumour 2 (cyan, for TN013 only), and the 7 Gy EQD isodose line (orange, corresponding to ≈40 Gy of SIRT in the normal liver only) were used to plan and assess the SABR planning. The first column is a ^{90}Y SIRT-naïve SABR plan, the middle column is the ^{90}Y SIRT dose calculated from the default body-based method in MIM and radiobiologically-converted to EQD, and the last column is the accumulated doses of the SIRT EQD with an SABR plan created with the 7 Gy isodose line. The PTV was defined as the combined tumour contours.

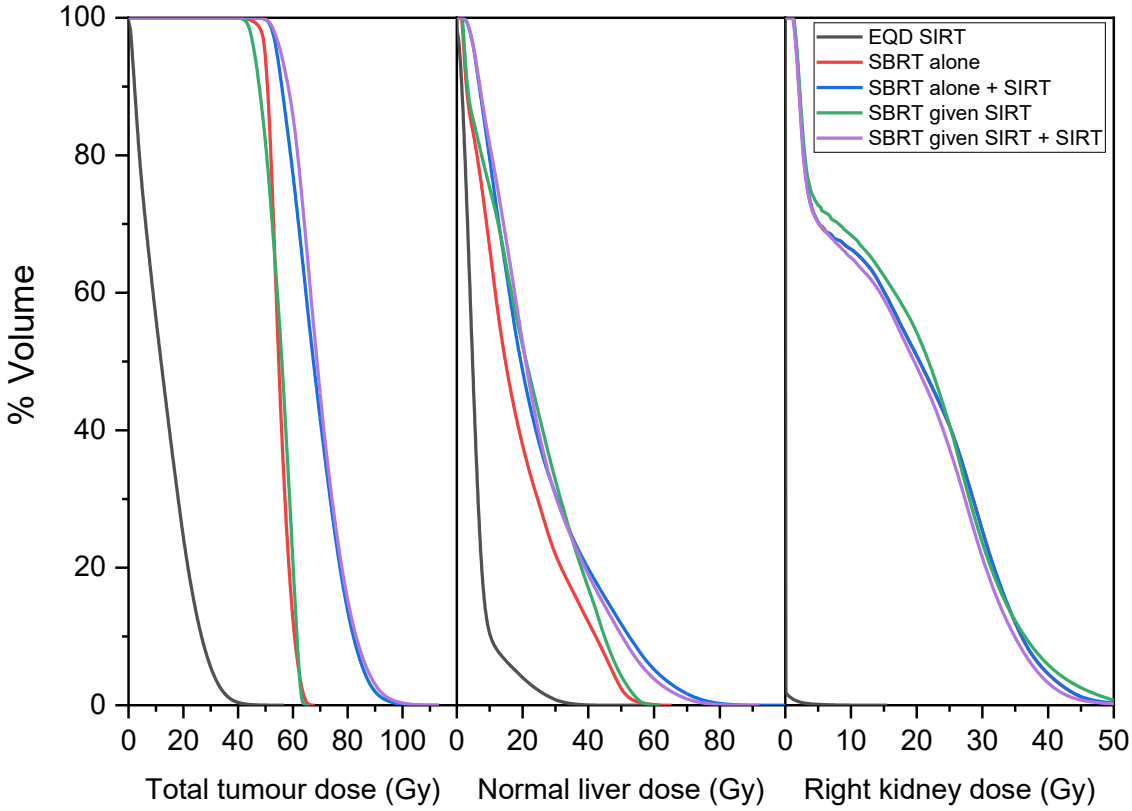

Figure 5.7-2 Patient TN009 DVHs of four EBRT plans for combination therapy. Tumour coverage (left panel) was best/maximal when considering dose constraint in the normal liver only and allowing unbounded doses to be put into the tumour. In normal liver (centre panel), doses were worst/maximal when including the dose constraint inside the tumour tissue (blue). DVHs for the right kidney (right panel, the extrahepatic OAR with the highest dose deposition) were effectively the same although results were marginally better/minimal for dose in the plan that utilised the isodose line of 7 Gy inside the normal liver. Other organs at risk such as lung changed very little across all the planned treatments as the beams did not significantly pass through these tissues.

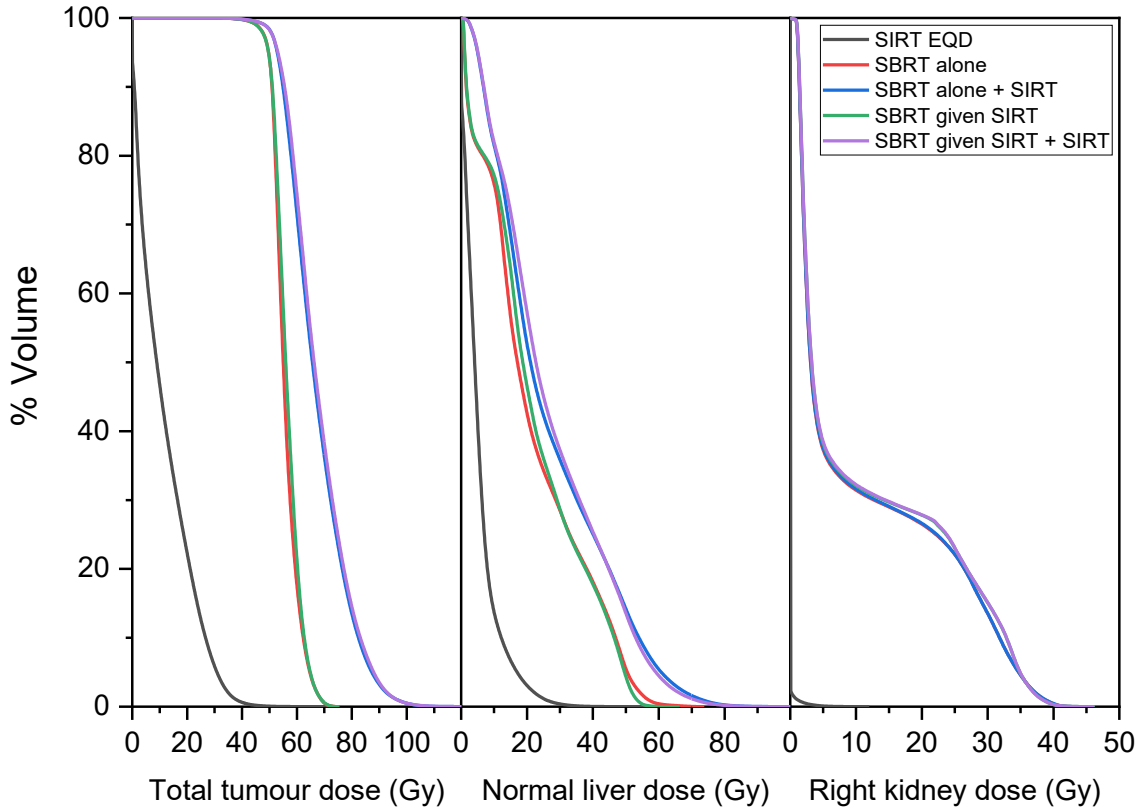

Figure 5.7-3 Patient TN013 DVHs of four different EBRT plans for combination therapy. Tumour coverage (left panel) was best/maximal when considering dose constraint in the normal liver only and allowing unbounded doses to be put into the tumour. In normal liver (centre panel), doses were worst/maximal when including the dose constraint inside the tumour tissue (blue). DVHs for the right kidney (right panel, the extrahepatic OAR with the highest dose deposition) were effectively the same although results were marginally better/minimal for dose in the plan that utilised the isodose line of 7 Gy inside the normal liver. Other organs at risk such as lung changed very little across all the planned treatments as the beams did not significantly pass through these tissues. Interestingly, SIRT has 6.5% of the tumour getting 0 Gy EQD.

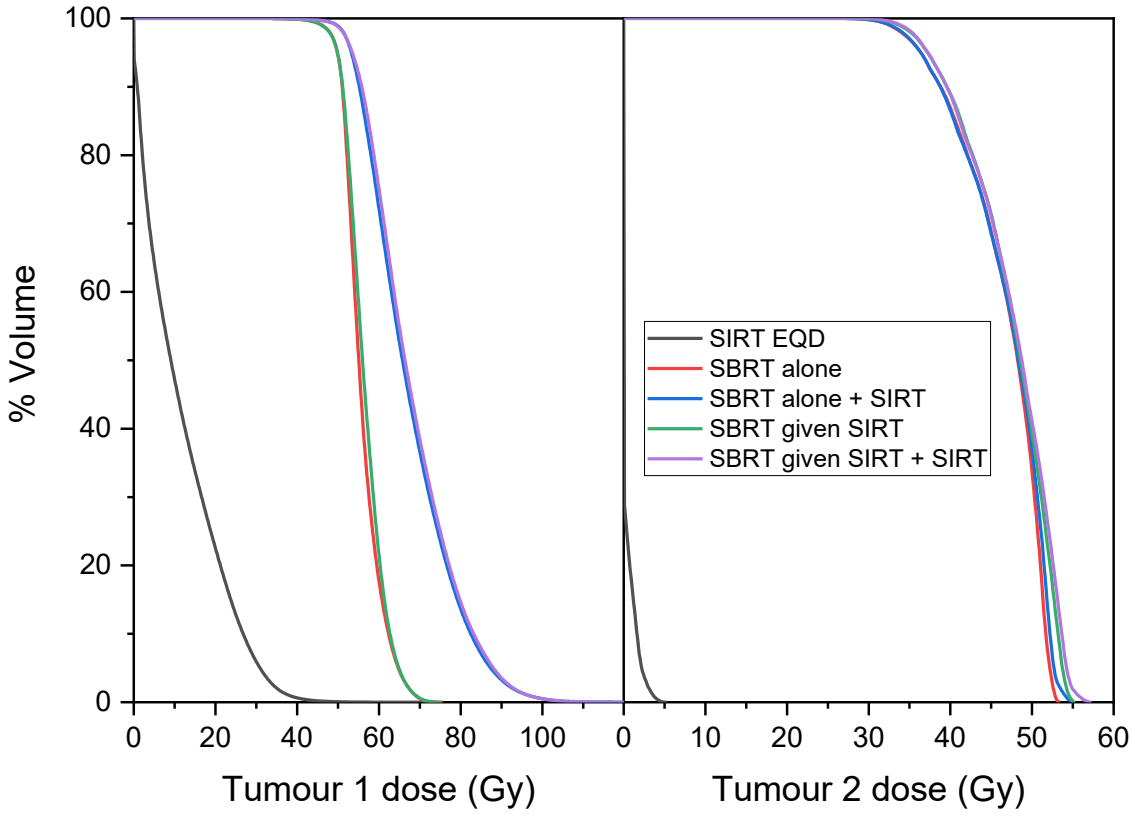

Figure 5.7-4 Patient TN013 total tumour PTV breakdown. Addition of EBRT made SIRT doses much more conformal. Separating the total tumour from Figure 5.7-3 into its two individual tumours revealed limitations of the single PTV approach. From the plans illustrated in Figure 5.7-1, tumour 1 (left panel) had 6% of the volume with 0 Gy EQD from SIRT. Because base dose was not utilised, the addition of SABR dose was more than the planned 50 Gy to 95% and so was overtreated. Tumour 2 (right panel) had 71% of the volume with 0 Gy EQD from SIRT. While Tumour 2 was part of the PTV, it was not independently treated so the minimum dose to 95% of the volume was less than the prescribed 50 Gy to the total tumour. Both accumulated plans of SABR with the SIRT dose yielded 95% coverage for tumour 1 and tumour 2 of 53.5 Gy and 37.2 Gy—7% greater and 26% less than prescribed—respectively. Consequently, the single PTV for multiple tumours is expected to result in worse response in tumour 2 than expected from the combined SABR and SIRT doses. The SBRT DVHs for tumour 2 agreed with each

other, whereas the tumour 1 DVHs separated because tumour 2 had nearly no component of SIRT dose deposition whereas tumour 1 did as shown in Figure 5.7-1.

Doses from ^{90}Y should only be considered inside the normal liver because the optimisation algorithm aims to decrease total normal liver doses as much as possible regardless of what the tumour tissue has seen before and additional constraints on tumour tissue would reduce total tumour doses. Future approaches should prescribe sum dose based on EQD and should allow for true base dose plan to be used in the optimisation calculations. Furthermore, planning treatments on patients with smaller tumours could achieve better targeting and treatment results. Dose from SIRT in normal liver was very small and the main toxicity risk would be from normal liver uptake. Yet, if performed conservatively, the dosimetry from this treatment cohort demonstrated that combined therapies could be done safely.

5.8 Summary

This chapter demonstrated that BED from separate radiotherapies can be combined in a clinically meaningful way. Future studies prospectively combining EBRT and ^{90}Y SIRT could add utility and flexibility to both treatments. However, a reasonably large randomised controlled trial would be necessary. This chapter offered methodological contribution to identify reasonable BED modelling and parameters, a potential clinical workflow methodology that could be applied to multiple tumour primaries, and assessment of dose-response in a small cohort that received combined EBRT and ^{90}Y SIRT.

6 Discussion

Radiotherapy has been marked by its success in maximising dose to tumours through precision targeting while sparing organs at risk. Conventional EBRT is prescribed and delivered by tailoring the beam shape and intensity to complement the targeted tumour and normal liver dose constraints. In some cases, among others, EBRT fails due to physical or biological limitations such as obstructed beam access from a dose-limiting organ at risk or side-effects from the treatment which disallow delivery of the full targeted prescription. EBRT exploits the varying radiobiology of targeted cancer tissue versus normal tissue. This is largely explained by the linear-quadratic model which is used for assessing varying fractionation schedules to achieve the desired dose-response effect. Modern external beam planning considers the effects of radiosensitivity, fractionation, and repopulation on the outcomes of the therapy.

These concepts from EBRT also apply to radionuclide therapy. Radiobiological parameters specific to radionuclide therapy remain substantially less-developed and this is partly due to the shortage of studies investigating the effects of radionuclides. Despite identical physical dose, phenomena which may vary substantially in radionuclide therapy compared to EBRT and result in differing radiobiologic effects include dose rate and LET effects (*93*). The modified BED equation used throughout this work is meant to account for these such phenomena which alter the RBE of radionuclide therapy versus that of conventional EBRT.

The use of targeted radiotherapies, particularly ^{90}Y SIRT, has created a need to further optimise dose administration. The delivery of multiple cycles of ^{90}Y SIRT or combination with various fractionation schemes of EBRT, poses significant clinical challenges. Dose-response is well-understood in the context of EBRT and, with the work presented here plus that which has emerged in the literature over recent years, there is an ever-growing body

of evidence that dose-response underlies ^{90}Y SIRT as well. However, radiosensitivity of ^{90}Y has only recently been directly characterised in biological systems (*46*,*81*). Consequently, doses for ^{90}Y SIRT have been prescribed and combined with EBRT based on physician experience without rigorous appreciation for the radiosensitivity of tumours to ^{90}Y SIRT. The work presented here addresses the radiobiological effects of ^{90}Y SIRT in cells and in patients. It proposes several strategies which could help with the decision-making process and to optimise dose delivery in various clinical scenarios involving ^{90}Y SIRT.

6.1 Clonogenic assays

The survival of DLD-1 and HT-29 cell lines after exposure to ^{90}Y, LINAC, and ^{137}Cs were determined to help answer the question of radiosensitivity from CRC, a common secondary liver cancer. The work presented here utilised the clonogenic assay as a measure of reproductive viability based on colony counts from the progeny of exposed cells. This expands upon a recent investigation by Gholami et al. (*46*), which determined survival to ^{90}Y using the MTS assay as a measure of metabolic viability based on an optical density approach. In their study, Gholami et al. also investigated CRC cell lines (HT-29, HCT-116, and SW-48). Only HT-29 was common to the results presented here.

These differing approaches offer their own advantages. In their study, Gholami et al. directly mixed cells with $^{90}YCl_3$ which captures the uptake of free Y^{3+} into the cell. This could have some broader implications for peptide receptor RNT such as ^{90}Y-DOTA-TOC or ^{90}Y-DOTA-TATE, where chelated ^{90}Y is delivered molecularly. Conversely, the experimental setup designed here (Figure 2.1-2 on page 19) was developed to represent the dose delivery mechanism of ^{90}Y SIRT. As the ^{90}Y microspheres become permanently lodged (Figure 1.1-3 on page 6) in the hepatic capillary bed and are not internalised into

the cells, the experimental setup used here physically separated the ^{90}Y from the exposed cells. The energy spectrum of ^{90}Y emissions was shown in Figure 3.1-2 to be proportionate, such that LET effects between dishes at varying distances from the source and target are believed to be negligible. However, in the experimental setup, the source dish and target cells are physically separated by millimetres. In SIRT treatment, the physical separation between the closest cancer cells and vasculature is only tens of μm. Nevertheless, tumours can vary up to several centimetres in diameter and it has been demonstrated that microsphere uptake is typically strongest at the interface of tumour and normal tissue (*9*). Therefore, dose penetration into the tumour from the boundary in such cases may still be adequately captured by this experimental setup.

Despite these different approaches, fits of the survival curves were used to measure the radiosensitivity parameters α and β to calculate various radiobiological endpoints. The linear quadratic model fit of the Gholami et al. survival curve yielded parameters (α=0.0842 Gy^{-1} and β=0.0239 Gy^{-2}) which agreed within the 95% CI of the EBRT clonogenic survival results. However, the fit parameters differ for ^{90}Y with Gholami et al. measuring α=0.0145 Gy^{-1} and β=0.0005 Gy^{-2} versus α=0.090 Gy^{-1} (95% CI, 0.063–0.116 Gy^{-1}) and β=0.000141 Gy^{-2} (95% CI, -0.000969–0.00125 Gy^{-2}) measured here (Table 3.2-1 on page 59). Although not directly comparable, this trend appears on average across the other unrelated CRC cell lines investigated in either study. The Gholami et al. results suggest a much greater surviving fraction after 8 days of exposure to ^{90}Y than these results after 6 days of exposure. This finding holds true even when correcting the clonogenic assay results for indefinite exposure (Table 3.2-4 on page 63). The correction factor decreases with exposure time (Figure 3.2-3A) therefore, the 8-day exposure of the MTS viability assay corrected for indefinite exposure would also not agree. This disagreement could be due to the fact that fatally affected cells in the ClonogenCity setup would not have been

included in the reseeding for colony formation after the exposure period. Alternatively, this disagreement could be based on the dosimetric assumption by Gholami et al. that ^{90}Y was uniformly distributed in the well without being internalised into the cells. The precipitation findings in Section 3.1.3 on page 53 and Figure 3.1-7 on page 56 illustrate that the distribution of the ^{90}Y source from YCl_3 can greatly affect the dosimetry when not corrected, though there was no indication of a need for correction in the Gholami et al. study. It may also be explained by the significant differences in the measured survival endpoints between the two approaches, i.e. colony formation vs MTS.

Despite differences in the mean energies, dose rates, and LETs of the delivered LINAC x-rays and ^{137}Cs γ-rays, the surviving fraction curves for either DLD-1 or HT-29 cell line was statistically significantly overlapping (Figure 3.2-1 and Table 3.2-1 on page 59) between the sources. A difference in cell kill was expected due to the order of magnitude higher dose rate from LINAC (6.6 Gy min^{-1}). The lower dose rate from ^{137}Cs (0.77 Gy min^{-1}) was expected to allow damage repair to increase cell survival, as repair is considered inevitable with dose rates under 1 Gy min^{-1}. Each of the sources delivered the desired radiation dose in less than 13 minutes such that the cell DNA damage repair response was not fully engaged to reduce cell kill (*94*). However, the radiosensitivity of the cell lines to LINAC and ^{137}Cs was statistically significantly higher than from exposure to ^{90}Y (Table 3.2-1). Unlike the acute exposures from LINAC and ^{137}Cs, full deposition of dose (up to 32 Gy at a maximum of 0.0028 Gy min^{-1}) from exposure to ^{90}Y occurred over several days which, under the assumptions of the Lea-Catcheside model, allowed the damage to be repaired. These repair and protraction of dose delivery dynamics have widely been adopted in the literature to explain the apparent radioresistance of clonogenic cells to ^{90}Y SIRT (*20*,*38*,*46*). These adopted approaches are mostly based on mathematical models explaining the interplay between dose deposition over time and the damage repair in cells

over time, most often assumed to be a monoexponential function (*70*). One such model is the Lea-Catcheside dose protraction factor based on several assumptions that are declared in its derivation in Section 8.4.1 on page 167. The Lea-Catchside factor is a model derived from first principles. This equation is a function of the repair half-time T_{rep} and physical decay half-life T_{phys} of the radioisotope (Figure 3.2-3A on page 62). T_{phys} for ^{90}Y is constant, but T_{rep} can vary based on the biology of the cell line. T_{rep} was derived numerically to estimate the correction factor due to finite exposure of the radioisotope. Unlike the indefinite exposure of SIRT, this results in a Lea-Catcheside factor value that is higher than the infinite limit would expect (Figure 3.2-3A). The correction to the Lea-Catcheside factor which was derived as a result of the statistical regression G_6/G_∞ was found to be nearly constant and independent of T_{rep} (Figure 3.2-3B on page 62) for exposure durations of less than 5 h. Applying the correction factor by substituting G_6 with the projected G_∞, i.e. multiplying the fit parameter for 6-day exposure by G_∞/G_6, further supressed the ^{90}Y β parameters closer to zero because $G_\infty/G_6<1$.

Although not explicitly shown in the published literature in the context of ^{90}Y SIRT, there is good experimental evidence to apply the Lea-Catcheside factor in low dose rate studies (*58*). As it is standard in the field, this was taken forward to correct fitted β-parameter values—since the Lea-Catcheside factor only applies to the dose-squared term—of the LQ model determination in Chapter 3 on page 45.

The ^{90}Y survival curves were fitted based on finite exposure. Conversely, the ^{90}Y SIRT treatment is under indefinite exposure conditions as the microspheres are left to decay fully *in situ*. A correction factor must be applied to the regression fit to assess the parameter values under indefinite exposure conditions, which is not experimentally possible to do with the clonogenic assay because the cells would require a change of media and might then form a confluent monolayer rather than discrete colonies.

Whether due to underlying radiobiology or choice of statistical method, the ^{90}Y fit parameter for the dose-squared term was found to contribute very little to the explanatory power of the model regardless of cell line (p>0.05 by a Wald test). The parameter fits were statistically indistinguishable from zero as the 95% confidence interval included 0 and all the behaviour of the data (given the large variance in the data) were explained by just the linear component. The LQ model was arguably over-fitting the data and this is also mentioned by Chiesa et al. and Bastiaannet et al. (*44*,*47*). For this reason, a linear fit was included (Table 3.2-1 on page 59), assuming the β term was 0 and this adopted assumption did not significantly affect the fit value for the α term. This assumption renders the α/β-ratio to be undefined; the term in the BED equation therefore becomes zero such that BED effectively becomes a linear scaling of dose.

Despite the arguable insignificance of the β term, extraction of the Lea-Catcheside factor for 6-day exposure was achieved by adopting the assumption $G_6 = \beta_{90Y}/\beta_{LINAC}$. By equating this empirical value with the full formulation of the Lea-Catcheside factor (Section 8.4.1 below), damage repair half-time (T_{rep}) values were measured by solving numerically (Table 3.2-3 on page 62). The DLD-1 T_{rep} parameter resulted in a physiologically meaningful repair time of 2.5 hours whereas HT-29 was 0.2 hours, which was unexpected as repair half times are known to be longer at around 1-5 hours (*20*,*46*). For comparison, the T_{rep} values derived from the dataset acquired from different methods by Gholami et al. including other CRC cell lines are very similar to one another at 1.06, 1.04, and 1.08 hours for HT-29, HCT-116, SW-48, respectively. These results lie within the 95% CIs for both cell lines measured by clonogenic assay, yet these CIs also contain negative values. Because of the large experimental uncertainties, it is challenging to read further into these determined repair half-times given the current dataset.

Using LINAC as the reference radiation source allows for comparison of the nonzero α-parameters, which do a better job than β-parameters at explaining the regression model against the data. Further radiobiological analysis can be made when proceeding the assumption that the RBE in its maximum value between the two modalities—as described by (*95*)—is $RBE_{max} = \alpha_{90Y}/\alpha_{LINAC}$. RBE is known to be a function of radiation type based on qualities such as mean energy, LET, and dose rate (*34*,*62*,*96*). In this way, RBE for ^{90}Y is expected to yield $RBE_{max} < 1$. Table 3.2-3 on page 62 shows that DLD-1 had an $RBE_{max} = 0.4$ whereas HT-29 paradoxically had an $RBE_{max} > 1$. These 95% CI for the α-values also overlap considerably. The fit values reported by Gholami et al. suggest $RBE_{max} = 0.172$ for HT-29, yet this result lies outside the lower CI. This further disagreement discourages confidence in the certainty of this finding. It is possible that this uncertainty was a result of the fitting method or from not having propagated experimental uncertainty throughout.

This further radiobiological modelling to measure RBE_{max} and the Lea-Catcheside factor relied on several assumptions that the two are directly related by measuring their ratios. Notably, the α values are related through RBE_{max} but the β values are independent of LET and thought only to be affected by modifications of repair. While other RBE models predict a dependency of β on LET (Stewart et al., 2018), these are primarily applied in the context of protons and heavy ions with LET>4 keV/μm greatly surpassing the current used radiation sources. Although a convenient approach to capture both fit parameters in one reference equation, this choice of radiobiological model is not standard, so further testing of these assumptions is necessary.

As reported by Chiesa et al. and Tai et al., efficacy in patients receiving glass microspheres or EBRT resulted in tumour α-values which were at least an order of magnitude smaller than reported in this thesis, 0.004 Gy^{-1} and 0.01 Gy^{-1} respectively (*47*,*54*). They attributed

these unexpectedly low values to being “effective radiosensitivity” only as pragmatic figures for modelling. Notably, their ratio yields an effective RBE_{max} of 0.4, which agrees with the hepatocyte RBE_{max} of 0.555 in the mixed model and particularly with the DLD-1 RBE_{max} of 0.388.

Several lessons regarding the experimental and statistical methods, such as dose rate effects and the value of physically isolating the source from the target were revealed. One must consider these caveats when applying these findings, which are also informative of other therapies targeting with ^{90}Y such as peptide receptor radionuclide therapy with ^{90}Y-DOTA-TATE.

Cells could only be plated for LINAC and ^{137}Cs irradiation doses up to 10 Gy for the CRC cell lines and 7 Gy for the HCC cell line. The number of cells plated was adjusted with the aim of achieving the same number of cells per plate. Because the cell morphology became irregular, higher doses resulted in colonies which merged. This means that values of the curve beyond 7 or 10 Gy are extrapolations from the data based on the LQ model, which may not make as much sense unless it is applied to BED modelling where fractionation is being considered. Likewise, doses up to 32 Gy were achievable for ^{90}Y. Any radiobiological modelling above these doses are extrapolations from the LQ-model fit parameters, e.g. dashed line in Figure 3.3-2 on page 67.

Ultimately, these cell experiments are a model for a biological system and there are a great number of complicating factors that may indicate variation of radiosensitivity *in vitro* from tumours in patients, i.e. whether cells grown in culture really represent human tumours. It can certainly be said that immortalised normal liver cell lines are no longer ‘normal’. For this reason, normal tissue modelling remains a challenge to represent *in vitro*.

The regression modelling yielded results which varied according to the method applied, such as boundary constraints or inclusion of a random intercept variable in the fit model.

Some methods produced negative parameter fit values, which are nonsensical under the assumptions of the LQ model. Since most of the variation in the survival curve data were found to be explained by the linear α component, the quadratic β component could be assumed to be zero.

Unlike the majority of quoted ^{90}Y radiobiology literature values which assume α-values are identical for ^{90}Y SIRT and EBRT, no *a priori* assumptions were made so fit was created without fixing the α-value from the regression to be identical across all modalities. This resulted in statistically significantly different α-values, and in order to have a consistent BED model, the RBE_{max} term is necessary. The fixed-alpha model assumes alpha is equivalent for EBRT and ^{90}Y and means that $RBE_{max} = \alpha_{90Y}/\alpha_{LINAC}$ is assumed to be unity. This is not necessarily an unreasonable assumption given the large uncertainties observed with this term. However, it does have substantial implications if alpha fit values of EBRT and ^{90}Y are different. For example, when $\alpha_{90Y} < \alpha_{LINAC}$, then BEDs less than physical dose are expected.

The assumption that α is the same hinges on assumed identical radiation quality (LET) between ^{90}Y, LINAC, and ^{137}Cs, but not repair or dose-rate effects which are typically associated with the β-value. Conceivably, the regression analysis could have incorporated the assumption that alpha values are the same in the model as has been implied by the field, but the statistically significant differences between α of each modality made this assumption unreasonable. One cannot know with certainty until undertaking further experiments like split dose or repeats of the experiments done here, including propagating experimental errors.

Error propagation of the standard errors from the regression modelling based on the formulae included in Section 8.5 indicated large uncertainties in BED calculations. Propagated errors excluded experimental uncertainties, e.g. uncertainties in pipetted

volumes and number of cells plated. While these sources of error were not accounted for and could affect the fit result, subsequent analysis proceeded from mean values.

There was great variability of the derived α/β-ratio depending on fitting method. To demonstrate why this might be, Figure 6.1-1 illustrates how noisy but similar datasets could derive vastly different survival curve shapes despite having similar α/β-ratios and highly similar curve shapes despite having very different α/β-ratio. Arbitrary α- and β-parameter values were chosen for their convenience for demonstration purposes. For these reasons, the standard error on each fit parameter tends to be large from the statistical model. These errors are magnified when deriving the α/β ratio.

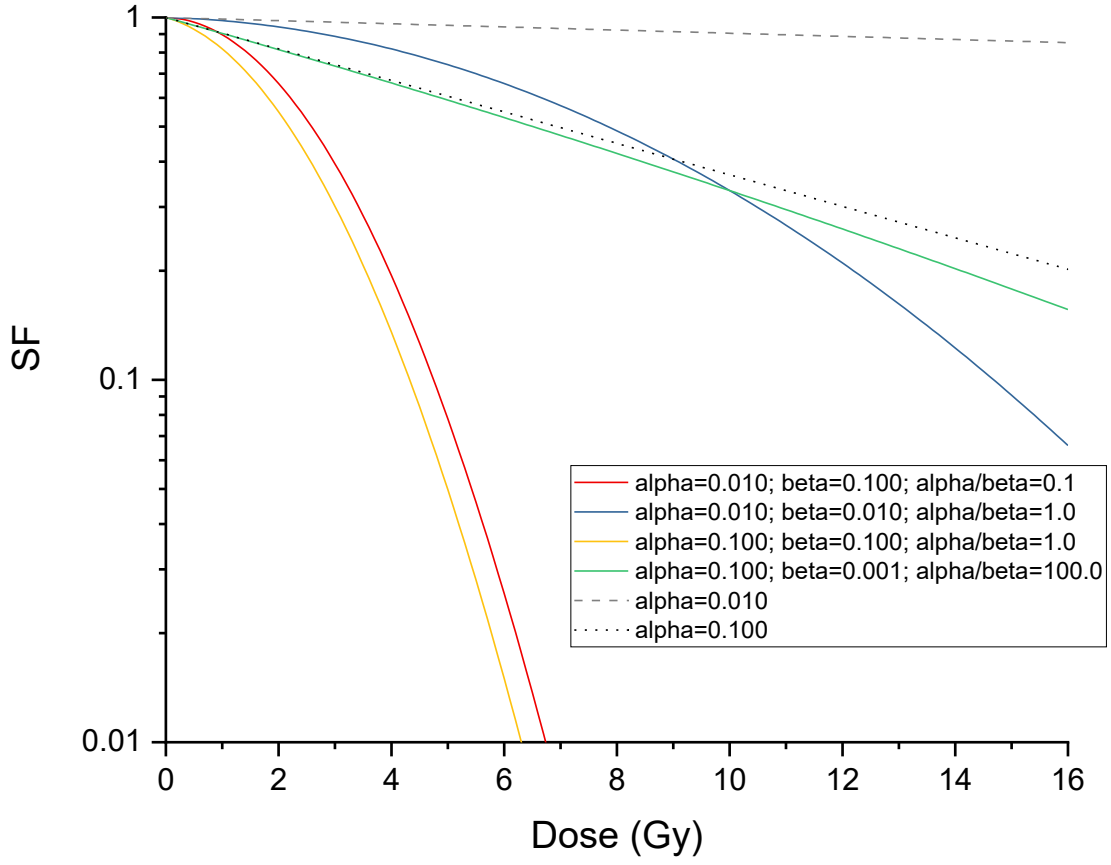

Figure 6.1-1 Comparison of survival curves with identical radiosensitivity parameters yet completely different shapes. The yellow and blue curves have the same α/β-ratio. The pairs of curves have the same α value (red and blue, or green and yellow).

6.2 Radiobiology considerations *in vivo*

Characterisation of radiobiological properties such as damage repair, checkpoints and reassortment are outside the scope of this work. However, they would be interesting to investigate further as it could elucidate the mechanisms of damage and how it is handled in SIRT patients beyond the concepts already explored here.

Results from the clonogenic assays yielded parameters for application to clinical data. Several models allow for direct comparison of ^{90}Y SIRT with EBRT through equivalent dose (EQD) measurements. Although the liver is a relatively radiosensitive OAR, EBRT has been utilised (especially with the advent of conformal techniques) to treat patients with liver tumours such as CRC metastases and primary HCC. EBRT treatments include various fractionation schemes like the conventional 2 Gy per fraction (sometimes referred to as EQD2) and ablative SABR 10 Gy per fraction (sometimes referred to as EQD10). As such, this tool is useful for direct comparison of dose values with similar cell killing effect regardless of fractionation scheme or radiation modality and can be defined in terms of different treatment schedules. The EQD effects are illustrated in Figure 3.3-2 on page 67 which demonstrates that the physical doses 10 Gy fractions have considerably greater potency against those from ^{90}Y SIRT and of 2 Gy fraction EBRT. Yet, ^{90}Y SIRT has several advantages over EBRT due to its low toxicity to normal liver and several clinical scenarios exist where it may be desirable to use both together (as discussed in the SIRT first cases in Chapter 5). As such, EQD was useful to define for the prospective SABR planning assessment of the combined therapies for the HCC patients in Section 5.7. Although the derived parameters would benefit from further confirmation with independent studies, the methods demonstrated here provide a robust approach for such dose combination scenarios.

BED units depend on the value of α selected. In this sense, BED units themselves vary according to the biology of each primary. An assumption usually adopted for EBRT is that the α/β ratio for normal cells is 3 Gy while for tumour cells is 10 Gy. This may generally be true, but it is also acknowledged that the values may vary and can be substituted with appropriate values. Consequently, the RBE_{max} and G values are also taken to be generally true, but may in fact have differing biology. The results presented here serve as preliminary evidence based on rigorous analysis using the clonogenic assay technique, which has historically been adopted as the gold standard owing to its ability to determine reproductive potential in addition to viability. The clonogenic assay remains very challenging experimentally. The successful experiments resulted in very large uncertainties, with α/β ratios in the hundreds of gray and dropping below 0 Gy, a theoretical impossibility. Consequently, the LQ modelling produces a wide range of possible BED values. Nevertheless, the results here are currently the only *in vitro* experimental evidence for ^{90}Y SIRT based on the clonogenic assay. The strength of these results confirmed in a CRC tumour primary that cells are more radioresistant when exposed to ^{90}Y than to EBRT.

The *in vitro* work demonstrated that the lower dose rate means that repair during exposure impacts outcome. This effectively increases survival at higher doses. The Lea-Catcheside correction accounts for repair from a fundamental principles argument (see Section 8.4.1 on page 167 for derivation). The CRC *in vitro* work demonstrated that the Lea-Catcheside repair factor G supressed the quadratic term of the LQ model. Even when accounting for the fact that infinite irradiation exposure did not occur demonstrated that the supressed β-term adjusted based on the measured repair half-lives resulted in betas that were not statistically significantly different from zero. As a result, this term can be neglected in the BED models resulting in a simplification $BED = RBE_{max} \times D$.

Although not considered in this work, repopulation of the cancer cells over a given time between exposures does play a substantial role in the effective biological response to the therapy. While cell repopulation does play a role in this work, limited data for this exist for ^{90}Y SIRT. Doubling times which affect the BED model would be based on results from EBRT which may not be representative of ^{90}Y SIRT treatment. Although repopulation was excluded from the model, it should be incorporated into the BED model as follows, which requires an additional term (γT) to explain the repopulation of tumour cells a certain amount of time (T) after treatment in a patient.

$$BED = D \times \left(RBE_{max} + G_{\infty} \frac{D}{\alpha/\beta} \right) + \gamma \mathrm{T}$$

Another radiobiological consideration is oxygenation. If the embolisation component of ^{90}Y SIRT reduces oxygen circulation in tumours, it could reduce the effectiveness of radiation. As oxygenation is related to circulation, perfusion through the liver plays a direct role. Although the literature shows that radioembolisation is not 100% embolic, the results from the PERFORM study indicate that perfusion is affected by the administration of ^{90}Y SIRT. This effect could suggest that a multicycle ^{90}Y SIRT has merit. The rationale would be to take advantage of reperfusion and reoxygenation of the tumour (*34*). After SIRT ablates the liver, the tumour rim (where greatest uptake frequently occurs) dies, then the hypoxic and slow growing region which likely had poor SIRT uptake due to higher interstitial pressure and poor vasculature can incur angiogenesis to reperfuse the tumour (*34*). This allows oxygenation to occur, and thus re-radiosensitisation. Furthermore, the enhanced blood flow to tumour means that ^{90}Y SIRT could take advantage of smaller administered activities per fraction, which would allow better tolerance to SIRT through the repair of damage from the reduced doses in normal tissue. In this way, Cremonesi et

al. suggest that multi-cycle SIRT would achieve tumour control by killing the ever-shrinking tumour rim through each cycle of the treatment (*34*).

A final radiobiological consideration was reassortment, i.e., changes in the distribution of different phases in the cell cycle, which was not investigated. However, prolonged exposure of ^{90}Y from SIRT might result in an accumulation of cell in the S-phase. Future studies could consider how the reassortment effect could be exploited during the administration of ^{90}Y SIRT, such as codelivery of modulating drugs.

The dose planning and retrospective EBRT combined with ^{90}Y SIRT investigations in Chapter 5 were designed to generate a basis and hypothesis for a clinical trial of combined therapies. A prospective clinical study would in turn provide clinical evidence for combined and multi-cycle therapies.

BED estimated for ^{90}Y as 0.6D from Table 3.3-2 on page 67 is based on the RBE_{max} concept. Applying this to all other tissues is an assumption but a reasonable one given evidence of the high α/β ratios seen and the protraction of total dose supressing the β term. Additionally, normal liver radiosensitivity measurements are absent in literature due to being very difficult to measure. Application of these adjustments (RBE_{max} and G) based on observed values from clinical EBRT parameters is the best approach available for organs at risk. As such, BED maps can be generated according to Table 3.3-2 across other OARs based on these parameters applied to their EBRT radiobiological parameter values.

The nature of SIRT dosimetry requiring post-treatment scans, which limits the therapy as current planning methods are not a precise indicator of dose deposition. Nevertheless, with dosimetry for ^{90}Y (and radiobiologically-informed dosimetry), treatment response can be predicted shortly after administration. Chiesa et al. highlighted the issue of nonuniform dose uptake from ^{90}Y SIRT (*77*), "We have a large waste of deposited energy in overkilling caused by non-uniformity. A fixed mean absorbed dose delivered to a bulky region seems

therefore much less effective than in EBRT uniform irradiation." By adding EBRT, possibly immediately after SIRT, to top up undertreated lesions, SIRT could achieve the minimum required doses with reduced doses absorbed in the critical organs. As the EBRT plan DVHs indicated, we would expect to see improved outcomes from increases in conformity of total absorbed doses. In addition, if the SIRT patient has good uptake and good response to a lower dose first cycle SIRT treatment, then they could be a candidate for repeat fractions of SIRT. These remain sensible options for circumventing the nature of SIRT dosimetry requiring post-treatment scans.

If treatment were successful for a patient, i.e. ideal deposition of the ^{90}Y microsphere and achieving controlled disease, it could be an indication for retreatment with ^{90}Y instead of EBRT (*34*). If the treatment dose deposition were poor, the intentionally conservative application of ^{90}Y dose would permit EBRT to top up undertreated areas. While this approach has strong theoretical merit, it has not been the focus of treatment centres as control of extrahepatic disease guides the treatment delivery away from such an approach. Future studies intentionally investigating this method are necessary to allow assessment of the clinical merit. However, earlier-stage patients, e.g. liver-limited metastases, would likely be the best suited to such an approach and have more treatment options elsewhere. Despite its theoretical merits, this proposal is complex for a clinical workflow and could face major challenges without full engagement from radiation oncologists.

Radiobiological considerations have merit for risk-based planning (*97*). Organs at risk contouring can be made to denote the area at greatest risk from exposure. If the average dose were taken, then a larger volume would dilute any highly treated volumes. As such, measuring ^{90}Y dose as the maximum dose allows for conservative estimates of OAR doses. Since ^{90}Y radiation penetrates tissue poorly (<11 mm maximum range, 2.5 mm on average), this amounts to negligible dose reaching extrahepatic OARs.

6.3 Imaging and dosimetry

The quality of images plays a major role in their quantitative accuracy. Phantom studies are required to achieve quantitative accuracy and adjust for artefacts through means such as dead time, attenuation, scatter, background, partial volume, recovery, and additional corrections to achieve calibrated measures (*98*). The application of appropriate reconstruction settings greatly affects the dosimetry results.

In the CRC cohort, bremsstrahlung SPECT was utilised to image the ^{90}Y distribution in the liver. Porter et al. performed and reported phantom studies on the exact scanner used in this dosimetry study (*98*). They identified optimal improvement of contrast recovery using OSEM (5 iterations, 15 subsets) with full Monte Carlo collimator modelling. The reconstruction was performed without scatter correction which generally should be applied to avoid inaccuracy of the deposited doses (*79*,*99*,*100*).

Recovery correction was also not performed. The recovery correction varies with volume such that smaller tumours would achieve lower counts than the true value as the signal intensity is washed out by surrounding volume of lower signal. Porter et al. also demonstrated an ≈20% lower contrast recovery for a 14.1 mL sphere than from a 33.5 mL sphere (*98*). While this approach was unavailable during the collection of these data, these optimised settings are especially important in SPECT where the imaging resolution is poor and inferior to PET.

Furthermore, partial volume corrections were not considered in the CRC group. Willowson et al. 2015 and Simian et al. 2016 illustrated recovered activity as low as 20% in small lesions (*78*,*79*). Due to their low contrast recovery, Willowson et al. 2015 and Porter et al. 2018 did not consider spheres for phantom studies of <4.2 mL (20 mm

diameter) (*78*,*98*). Despite the finding in the CRC cohort that it did not affect the linear regression coefficients, separate analysis for tumours <10 and >10 mL was necessary.

In the HCC cohort, bremsstrahlung SPECT and PET were both used to image ^{90}Y distribution, depending on what was available for each patient. While the aforementioned caveats of SPECT-based dosimetry still apply, the reconstruction techniques used in this different treatment centre were adopted from MIM-recommended settings. MIM recommended settings were also applied to PET scans according to the findings of the QUEST study (*78*). In the QUEST study, Willowson et al. indicated that without the time of flight and resolution recovery corrections applied, image quality and quantification in a 37 mm diameter sphere was underestimated by approximately 30%. While the vast majority of tumours investigated in the HCC cohort were greater than 37 mm in diameter, the applied corrections ensured that activity and subsequent dose quantification were accurate.

For imaging ^{90}Y, SPECT has more noise due to bremsstrahlung signal while PET has a very low branching ratio but a more discrete uptake and superior spatial resolution. Accordingly, from these patient cohorts, the ^{90}Y SIRT dose distributions appeared different for the SPECT due to the spatial resolution limitations of bremsstrahlung SPECT. This is apparent when comparing the DVHs from patients with SPECT-based dosimetry (TN005, TN012, and TN029) versus the other patients with PET-based dosimetry, mentioned in Figure 5.6-2B on page 110. The effect also manifests in Figure 5.5-1 on page 105 where the cumulative DVHs for the SPECT-based dosimetry are initially flat at low doses whereas the PET-based dosimetry from the other patients generally has a steep falloff of coverage at low doses. These phenomena can affect the mean value across voxels

in a tissue and, without proper recovery correction, can lead to inaccuracies of dose measurement.

In addition to imaging approaches, the dosimetric methodology can play a role in accuracy. The convolution dosimetry method using a dose voxel kernel adds blurring in the resultant dose distribution. A study by Pacilio et al. indicated that the local deposition method was suited to 3D dosimetry from SPECT images as it was "more strongly represented by image blurring than by differences among the dosimetric methods" (*101*). For this reason, local deposition was adopted as the favoured method for both CRC and HCC patient cohorts.

LDM with known activity assumes that all injected activity is visualised in the PET image, specifically in either the liver or whole body. When using a liver-based approach, it is important to correct for any shunting of dose to the lungs as this affects the amount of activity that is taken up by the liver. MIM calculates dose differently by using a volume-based *S*-value 4.794×10^{-5} Gy mL Bq^{-1}. Dosimetry in the CRC cohort used an *S*-value of 6.22 Gy Bq^{-1} h^{-1}. The S-value for the CRC cohort in the same units as for the MIM method was: $(4.42\ \text{mm})^3(10^{-3}\ \text{mm}^3\ \text{mL}^{-1})(6.22\ \text{Gy MBq}^{-1}\ \text{h}^{-1})(10^{-6}\ \text{MBq Bq}^{-1})\left(\frac{64.1\ \text{h}}{\ln 2}\right) = 4.967\times10^{-5}\ \text{Gy mL Bq}^{-1}$. Therefore, the CRC-cohort used an *S*-value that was 3.6% larger, and so if all other dosimetry steps were performed identically, the differing *S*-value would result in slightly higher deposited doses.

Dose quantification is defined based on the contouring of specific tissues. In the CRC cohort, discerning tumours from normal liver was difficult, even with the window and level options set to maximum contrast settings. This is largely due to imaging resolution of soft tissues, which non-contrast CT has difficulty with but where MR imaging excels. For example, pairing CT imaging with MR adds value of discerning common but benign liver cysts from cancer. While there is some visible difference in tumour morphology from normal liver, e.g. density from interstitial pressure, necrosis, and calcifications, it is not

enough to rely on these alone. For this reason, MR images—particularly the standard fat saturated sequence—were also used to inform variability in soft tissue for the CRC cohort. Additional methods to aid in the discernment of normal liver from tumour tissue is the injection of contrast agent. The venous washout phase of the injection imaged is most useful because the poor perfusion of the tumour tissue leads to retention of the contrast agent. This consideration of maximising tumour contrast aids in contouring, which could affect the distribution of dose values considered in the tissue, especially with the inhomogeneous doses seen from ^{90}Y SIRT treatment. As such, the nuclear medicine imaging upon which dosimetry is based would ideally be acquired with contrast as well.

For the CRC cohort, all contours were newly created and validated by oncologist Tessa Greenhalgh. For the HCC cohort, some imaging had contours pre-existing from clinical analysis. However, all contours were redone from the clinical version, including those used for EBRT treatment planning so that the method was consistent. The newly created contours were generally comparable to the clinically-established ones and also were validated by radiologist Robert Young to ensure they were consistent and reliable. However, artefacts of this approach were evident in their DVHs which all show a lower volume achieving prescribed dose than would otherwise have shown achieving 95% coverage (Figure 5.4-1 on page 100). These artefacts are carried throughout the radiobiological analysis too.

In the HCC cohort, the sum BED output required accumulation of doses recorded from two different anatomical reference scans. Despite evolving and improved methods emerging regularly and algorithms which are successful for specific purposes, deformable registration is not commonly considered robust. In general cases, especially those where patient imaging setup parameters varied, e.g. exposure time and breathing pattern, deformable registration is particularly challenging as these parameters can greatly alter the

orientation of internal organs. As contours were already defined as part of the analysis workflow, a hybrid MIM deformable registration method which accounted for contours as well Hounsfield units was adopted and shown to offer the best results. The dose accumulation method in MIM prevented deforming and distortion of the original dose data. Instead the contours were modified relative to the reference frame.

6.4 Patient outcomes

Currently, no universal standard for reporting of ^{90}Y SIRT dosimetry and no methods for dosimetry-based treatment planning exist (*102*). This is partly due to the large randomised controlled trials to date for ^{90}Y SIRT focusing not on measured dose values but other safety and efficacy-related endpoints. Published guidelines provide the best practice for standard of care (*35*,*43*). Ideally, these should be followed at all centres performing ^{90}Y SIRT, yet until recent years, dosimetry had remained overlooked in the clinical workflow. This has been partly due to the retrospective nature of dose measurement for ^{90}Y SIRT and also to the lack of tools. Commercial tools have begun to emerge such as Varian's Velocity™ RapidSphere, Hermes Medical's Hybrid 3D™ SIRT, MIM's SurePlan, Philips' STRATOS, and Mirada's Simplicit^{90}Y™ and treatment centres are beginning to adopt them. This is partly due to European Union regulations on the assessment of patient dose from interventional radiology techniques including ^{90}Y SIRT coming into effect as of 6 February 2018 and the increasing awareness of the merits of performing dosimetry on radionuclide therapies (*103*). Without thorough multi-centre studies using large patient cohorts to identify optimal dose-response relationships, adopting standards is the best option to inform dosimetry studies.

6.4.1 Colorectal carcinoma cohort

The Kaplan-Meier estimate for this CRC cohort showed a median OS of 10.5 months. This is 12.1 months shorter than that of the recent phase III FOXFIRE, SIRFLOX, and FOXFIRE-Global combined analysis, which found improved local control in the liver from ^{90}Y SIRT but no increase in OS (*104*). This discrepancy cannot be explained by the activity prescription approach since the methodology was common to the combined analysis and this study.

Instead, some clues about this discrepancy are seen in the breakdown of the patients. Baseline characteristics from the combined analysis indicated a lower rate of metastatic disease outside the liver compared to the cohort analysed here. The combined analysis cohort also had no previous lines of chemotherapy and were given concurrent FOLFOX whereas the cohort studied here generally had multiple lines of prior chemotherapy (Table 4.1-1 on page 70). This group had no patients with radiological CR while 14% were PR. However, in the combined analysis 68% of the patients were CR or PR. These differences suggest that the patients from this cohort had a higher disease burden than the cohort from the combined analysis.

6.4.1.1 Dose-response

A correlation between change in individual tumour volumes and their mean, median, or D_{70} dose was demonstrated (*20*,*21*,*27*). Dose-response threshold values of 48.3, 48.8, and 41.8 Gy from the individual tumours were determined from the CT-based volumetric response of mean, median, and D_{70} doses, respectively. Although not directly comparable due to methodology differences in either superior ^{90}Y PET-based dosimetry or using ^{99m}Tc-MAA SPECT dosimetry, several other studies yielded conclusions which were in accord with these findings. Flamen et al. reported a mean dose >66 Gy (95% CI 32-159

Gy) was necessary to prevent progression (*25*). Although likely to differ from morphological assessment on CT as the dose-response measurement was based on metabolic response on an FDG PET/CT scan, Willowson et al. reported a mean dose of ≈50 Gy (*105*). Levillain et al observed that patients with mean tumour dose >39 Gy achieved a significantly longer OS (*26*). Fowler et al. reported MR-based volumetric response predictors of 29.8 and 42.3 Gy for mean and D_{70} doses respectively (*21*). A prospective study by van den Hoven et al. reported a required minimum dose of 51±28 Gy was necessary to reduce TLG by >50% at 1-month follow-up (*27*).

Other studies have demonstrated that baseline and threshold values can relate to measured tumour response to radiation treatment. For example, Bhooshan et al. demonstrated that baseline volume was a significant predictor for vRECIST SD or PR (*106*). Testing the hypothesis that baseline tumour volume could predict response in this CRC patient cohort found no statistically significant correlation between change in tumour volume and log baseline tumour volume. The reason for this lack of correlation is thought to be due to the role of absorbed dose to these tumours as dose-response has been recently demonstrated in ^{90}Y SIRT (*20*,*27*). Non-uniform dose deposition across the tumour has shown it could overtreat the tumour in some areas beyond added therapeutic benefit (*20*,*31*,*87*,*107–109*) and undertreat some parts of the tumours and therefore not achieve response (*32*,*105*). For this reason, RSD of dose throughout the tumour voxels was evaluated against change in volume of the individual tumours. However, this analysis also found no statistically significant correlation. Beyond these RSD and baseline volume correlations with change in tumour volume, variability in response among tumours and individual patients may be a consequence of biology from genetic or other pathological characteristics. An example of this was the finding that right-sided primary CRC tumours were more likely to result in a “statistically and clinically significant OS gain” in the combined FOXFIRE Global and

SIRFLOX trials possibly because they have distinct embryological origins compared to left-sided primary CRC tumours (*15*). However, a full biologic explanation of the predictive capacity of primary tumour side to SIRT response is unknown. Nevertheless, these specifics remain unclear and further investigation would benefit from a larger cohort size.

6.4.1.2 Radiobiology

An additional benefit of appreciating the dose-response of ^{90}Y SIRT is the better understanding of the radiobiological effect of required dose to achieve tumour control. The BED model adds clinical utility when planning multiple cycle therapy or combination with treatments such as EBRT (*34*). One reason EBRT would be used is for curative approach by targeting undertreated areas from ^{90}Y SIRT with top-up doses of SABR. Critically, the robust approach relies on radiobiological understanding and modelling of the therapies, as shown in Section 3.3. In this way, BED and EQD models based on the underlying radiobiological parameters are highly useful for clinical applications. Prior to this work, BED calculations based on experimentally-derived radiobiological modelling parameters have not been performed in ^{90}Y SIRT, partly due to the lack of experimentally-derived radiosensitivity parameters (*20*,*52*). Instead, ^{90}Y SIRT was assumed to be related to EBRT by adjusting the β term of the LQ model for EBRT by the Lea-Catcheside protraction factor. This assumption was shown not to hold as the experimentally-derived β term was zero and the introduction of the RBE_{max} term to account for decreased radiosensitivity of the ^{90}Y β^- particle radiation versus LINAC photons (*81*).

Compared to *in vitro* α-values of ≈0.2 Gy^{-1} found from clonogenic assays of CRC cell lines, efficacy studies by Tai et al. and Chiesa et al. in patients receiving EBRT or glass ^{90}Y microspheres found significantly lower α-values in tumours of 0.01 and 0.004 Gy^{-1} respectively (*47*,*54*). However, they suggested that these values were unexpectedly low

due to being measures of “effective radiosensitivity” based on a different modelling approach rather than measures of intrinsic radiosensitivity. Remarkably, attempting to measure RBE_{max} from the ratio of these “effective radiosensitivity” values between the EBRT and ^{90}Y SIRT results in a value of 0.4, which agrees with the mixed result of CRC cell lines finding an $RBE_{max} = 0.555$. This value is in particularly close agreement with $RBE_{max} = 0.388$ for the DLD-1 cell line.

In the CRC cohort, dose was shown to correlate with ^{90}Y SIRT treatment response. Though BED was not demonstrated, it would be expected because the BED model adopted here for ^{90}Y SIRT is nearly a linear scaling of physical doses by the RBE_{max} factor and so the correlation coefficient would follow similarly. No major toxicity was observed in any of the patients from this CRC cohort. This is likely due to the radiobiologically low doses delivered to the normal liver tissue across the patients.

6.4.1.3 Perfusion

With respect to the subcohort of CRC patients received perfusion imaging, tumours in which greater doses were deposited achieved increases in permeability and decreases in blood flow. This suggests that the vasculature in the tumours was compromised relative to baseline. The slope of the correlation between MTT and dose was positive such that each Gy of dose yields a change of 0.61 s of MTT at one month compared with baseline. This suggests that tumours with higher doses are expected to achieve greater increases in residence time of contrast, which implies that perfusion becomes poorer, possibly due to compromised vasculature.

All pCT perfusion parameters assessed as change at 3 months follow-up against dose (and also BV against volume change) were statistically significant. After the lapse of two additional months, BV showed a positive correlation with dose suggesting tumours that achieved greater doses were to achieve greater differences in BV. Furthermore, higher

doses achieved increases in permeability and decreases in blood flow, suggesting decompensation of the vasculature in the tumours relative to baseline. Counterintuitively, the BV was higher while BF was lower with added dose. This could be explained by extra pooling of blood in tumours with higher doses since BV is calculated as MTT times BF. Supporting the blood pooling hypothesis, the slope of the correlation between MTT and dose was positive such that each Gy of dose yields a change of 0.57 s of MTT at three months compared with baseline. This suggests that tumours with higher doses are expected to achieve greater increases in residence time of contrast. Especially for tumours which received higher doses, perfusion becoming poorer with dose implies that the change in physiology is due to the ^{90}Y SIRT treatment. As such, one could anticipate that the vasculature may change for tumours which received higher ^{90}Y SIRT doses. Changes in vasculature could have consequences for the retreatment, even though retreatment may be unnecessary because high dose tumours generally showed volumetric response and response in perfusion imaging.

Several baseline perfusion parameters correlated with either dose or volumetric response, suggesting there may be some prognostic utility for perfusion imaging of ^{90}Y SIRT. DCE MRI perfusion results demonstrated that only the k_{ep} parameter at baseline was associated with change in relative volume. Notably, this is in agreement with a study by Coenegrachts et al. (*110*). While pCT parameters more-frequently resulted in correlations which reached statistical significance, DCE MRI only did so for baseline k_{ep} as a measure of change of relative volume. Potential explanations for this discrepancy include the nature of in-house methods rather than the mature clinically-deployed workflow from which pCT benefitted and data limited to 10 patients with 53 individual tumours. Regardless, generally in this experience, DCE MRI did not perform nearly as well as pCT at identifying associations with dose or response. Caution should be taken if applying such techniques, until such

relationships can be definitively identified, or the technology is further developed for quantitative liver perfusion imaging.

As doses deposited were higher and therapeutic effect was expected to be greater, perfusion parameter change was observed. These results are a promising indication that perfusion imaging, in particular pCT metrics, may be associated with the deposition of ^{90}Y SIRT microspheres and tumour response. Further investigations are needed in more patients to confirm these findings, including studies of the effects of perfusion nonuniformity throughout a tissue. Determining a relationship between perfusion and revascularisation would be particularly useful as this usually suggests a tumour is aggressive and associated with poorer patient outcomes and may impact clinical decisions about multi-cycle SIRT.

6.4.2 Hepatocellular carcinoma cohort

This HCC cohort provided a rare opportunity to assess patients treated with both ^{90}Y SIRT and EBRT, allowing for some insight into what an intentional combination treatment would involve. Major challenges in this cohort were that it was a heterogeneous group and that few patient numbers meant there was weak statistical power to draw general inferences on the wider population. Limiting the scope of the analyses to consider EBRT and ^{90}Y SIRT treatments separately controlled for the difficulties which arise from many variables.

Analysis of independent patients was necessary to draw inferences from the treatments. For example, TN005 had a complicated case with remote history of lung cancer, hepatitis C causing HCC, undergoing initial resection of hepatic segments 4 and 8 and treatment with sorafenib 1-year post op. Recurrent disease was then treated with 1.7 GBq ^{90}Y SIRT.

Subsequently, SABR with a total dose of 50 Gy in 5 fractions over 9 days was used to treat an inferior right lobe of liver mass unable to be retreated with ^{90}Y SIRT.

6.4.2.1 Dosimetry

Patients TN005 and TN029 who received SIRT first had apparently better sum BED distributions than the EBRT-first patients. This was likely because the EBRT contributed better conformity as it was planned considering the ^{90}Y SIRT as a base dose. Another explanation could be that the sequencing of the therapies mattered, for example that the EBRT modifies perfusion and therefore affects the uptake of the ^{90}Y microspheres.

There are several dosimetric approaches which can be taken with ^{90}Y SIRT including voxel kernel convolution and local deposition and clinical standards across institutions have not been adopted unanimously. As demonstrated by the 30% deviation in Figure 5.3-1 on page 97, these approaches can lead to striking differences in measured absorbed dose depending on the method used. For example, in the body-based method, MIM SurePlan included total signal in the entire body contour to scale the injected activity against. Even after reconstruction, some of these images may have background signal from noise where ^{90}Y dose is not deposited. Consequently, the voxels with the signal of interest in the liver could be outweighed by the large number of voxels across the entire body, biasing the measurement of total signal. This known issue is an active area of research. Other caveats of the ^{90}Y SIRT dosimetry process play a role, e.g. in some software applications, negative image values cannot be stored. Such a restriction means that any background subtraction method would achieve voxels with negative values from subtraction of the baseline set to zero while positive noise remains. Consequently, half the signal attributed to noise remains and this can bias the measurement of signal in the liver voxels. The body-based method from this comparison probably underestimates dose because of background signal in other parts of the tumour. Correspondence with MIM

software suggested that this could be improved with better reconstruction, or background subtraction. While studies such as the MD Anderson investigation of SPECT/CT reconstruction (*79*) indicated good agreement between methodologies, this was not reproduced here for all tumours in question. This could partly be attributed to variations between different treatment centres or noisy images post-reconstruction, despite adopting best practice recommended parameters. While these software solutions typically have undergone rigorous testing to meet regulatory standards such as 510k clearance, it is prudent to appreciate that subtle differences in method could result in differing dosimetric results.

Another caveat is that MIM did not include calculated dose outside of the liver. While it is true that nearly zero dose is deposited outside the liver, additional correspondence with MIM indicated that this is because the dosimetry methodology assumes a liver density of 1.04 g mL^{-1} for soft tissue in the liver. Consequently, dose calculation in organs of differing density, such as lungs or bowel, would be less accurate. Aims to evaluate a tissue density mapping against the PET or SPECT signal are currently under development to account for this.

6.4.2.2 Inverse dose planning

In the previous cases where SABR was given after ^{90}Y SIRT, the BED doses from SIRT were applied based on clinical experience (as described in Section 5.6). The plans of patient TN013 have more variation than the other patient due to the multiple target areas in the liver. Consequently, the dose was not as homogeneous. Additionally, tumour 2 of patient TN013 had a minimum dose to 95% of the volume less than the prescribed 50 Gy. This was because tumour 2 was an individual target that was part of the whole PTV. To achieve the minimum prescribed dose in individual targets, multiple PTVs must be defined. However, in various clinical scenarios, it may be convenient to keep PTVs for individual

tumours separate, e.g. based on proximity to one another, or to combine the PTVs. Either way, this separation of PTV must be considered when taking ^{90}Y doses into consideration as it was shown here to have dosimetric implications (*63*).

There remains an opportunity to reduce initial ^{90}Y SIRT doses as a test of whether the ^{90}Y microspheres deposit in a spatially optimal way in patients. As there has been clinical evidence suggesting multiple ^{90}Y SIRT treatments are comparable within the same patient, reduced initial doses allows an option for repeat treatment with ^{90}Y SIRT if the patient does well, which allows the advantage of lower risk from EBRT toxicity. If the tumours still do not respond or conversion to a curative therapy is desired, there remains the option to follow-up with SABR to top up under-treated tumours without risking toxicity. The additional flexibility of this approach suggests that initial treatment with ^{90}Y SIRT retains several advantages in the clinical approach.

6.5 Future directions

Many of the findings in this work revealed shortcomings of methodology or areas for future development. Further radiosensitivity characterisation of ^{90}Y SIRT in additional tumour histology, such as intrahepatic cholangiocarcinoma, breast, and HCC, would provide valuable evidence for application to the BED model discussed. Preliminary work in HCC fell short due to several challenges of the developed assay as previously discussed. Even with a specially designed experimental container with alignment posts, dishes with differing dimensions could cause tipping to occur. Chemical interactions between the source and buffer, such as precipitation seen here, can interfere with the geometry. It would also have been ideal if the source could be solidified as this would guarantee uniformity was constant throughout the experiment, provide easy solid waste disposal, and limit evaporation effects. However, when attempted here, this was not convenient to achieve

due to the complexity of handling an open source and mixing with, e.g. hot agar. A compromise solution for waste disposal is to use sodium polyacrylate, a super absorbent polymer which captures all the liquid into a gel. This is also convenient for clean-up of liquid contamination from spills and is recommended for the handling of mL volumes of radioactive source.

The perfusion imaging results indicated that pCT in particular would have merit as a prognostic tool for dosimetry. While pCT achieved statistical significant associations and was already a commercial software package, DCE MRI perfusion analysis was performed in house. Because DCE MRI is a very similar technique to pCT, similar findings would be expected. Further investigations of perfusion in larger prospective trial are needed to extend this work. A research question of relevance to ^{90}Y SIRT is whether revascularisation is predictive of subsequent retreatment outcomes. This hypothesis could serve as a convenient tool for ^{90}Y SIRT prognosis and treatment approaches.

Although too early to recommend, it would be useful to further explore the treatment paradigm that complements the specificity and reduced toxicity of ^{90}Y SIRT with the accuracy and ability to prospectively plan SABR. This work has shown that ^{90}Y SIRT and SABR could cooperate to produce better DVHs than ^{90}Y SIRT alone. Another prospective trial which could benefit ^{90}Y SIRT treatment would test the combination of ^{90}Y SIRT with EBRT. Further clinical trials would be necessary, for example, a larger trial to characterise dose-volume toxicity and response constraints would provide great clinical utility. As mentioned previously, having standardised practices would allow for prospective measurement of dose-response effect and establishing the standard methods and best practice, e.g. RTOG trial. It would be ideal to have a prospective trial to answer the question of doses used, to increase tumour conformity and mean dose deposition, bearing in mind liver toxicity was seen in dose escalation studies in the 1990s.

6.6 Conclusions

Dosimetry has substantial value in the assessment of ^{90}Y SIRT therapy. When applied, appropriate radiobiological models could play an important role for personalising radiotherapy of liver tumours with ^{90}Y SIRT.

The clonogenic assay comparing ^{90}Y β^- particles with 6 MV LINAC x-rays and ^{137}Cs γ-rays was performed in DLD-1 and HT-29 CRC cell lines of variable radiosensitivity to appreciate the varying radiosensitivity of patient tumours. Regression analysis of the survival curves using the LQ model to measure radiosensitivity parameters concluded that ^{90}Y α-values were statistically significantly different from LINAC and ^{137}Cs. ^{90}Y β-values were very small and not statistically significant from zero.

A method was developed and explored relating the ^{90}Y physical dose to equivalent EBRT doses based on biological effect models (BED and EQD) from the radiosensitivity fit parameters. This method was applied to the CRC patient data. It was also applied to the HCC patient cohort who received both ^{90}Y SIRT and EBRT for sum BED and inverse dose painting exercises based on inferred radiosensitivity parameters.

Foremost, the measured α and β parameters indicate that BEDs for ^{90}Y SIRT are less than the physical dose deposited as a consequence of the protracted low-dose-rate delivery of the ^{90}Y radiation, which allows time for repair processes to take place. This suggests that on a Gy-by-Gy basis, ^{90}Y is less potent at killing cells and that normal tissue is more tolerant to ^{90}Y than EBRT.

SIRT followed by SABR allows for more dosimetric control over the patient's therapy planning. Improved control adds flexibility for the clinical workflow which could further benefit the patient. While limitations in the patient's status may limit the ability to treat first with SIRT (e.g. workup scan must be done in advance), utilising these dosimetric

tools separately may add considerable improvements in DVHs, and suggests it may improve patient outcomes. Prospective clinical trials are needed to assess this hypothesis. ^{90}Y SIRT has tremendous potential but has been limited due to its use mainly in late stage patients. Although ^{90}Y SIRT has shown merit to control local disease in the liver, it is unlikely to be curative, partly due to the late stage in which patients are prescribed ^{90}Y SIRT. Some of these treatment approaches, namely SIRT and SABR, might have potential to be used synergistically with curative intent through their careful combination. SABR does risk some complication due to dose volume toxicity limitations but could have merit for well-differentiated tumours. The combination of both therapies could offer several logistical, financial, and therapeutic advantages. No alternatives which provide reliably better results exist and in these early stages, this unique approach to target tumours mechanically offers several degrees of control which can be manipulated to the advantage.

7 References

1. Kelly CM, Kemeny NE. Liver-directed therapy in metastatic colorectal cancer. *Expert Rev Anticancer Ther*. 2017;17:745-758.
2. Wong J, Cooper A. Local ablation for solid tumor liver metastases: Techniques and treatment efficacy. *Cancer Control*. 2016;23:30-35.
3. Bentzen SM, Constine LS, Deasy JO, et al. Quantitative Analyses of Normal Tissue Effects in the Clinic (QUANTEC): An Introduction to the Scientific Issues. *Int J Radiat Oncol*. 2010;76:S3-S9.
4. Bouvry C, Palard X, Edeline J, et al. Transarterial radioembolization (TARE) agents beyond 90Y-microspheres. *Biomed Res Int*. 2018;2018:1435302.
5. Eckerman KF, Endo A. MIRD: Radionuclide Data and Decay Schemes. Vol 50. SNMMI; 2009.
6. Mazzaferro V, Sposito C, Bhoori S, et al. Yttrium-90 radioembolization for intermediate-advanced hepatocellular carcinoma: A phase 2 study. *Hepatology*. 2013;57:1826-1837.
7. de Silva S, Mackie S, Aslan P, Cade D, Delprado W. Histological Comparison of Kidney Tissue Following Radioembolization with Yttrium-90 Resin Microspheres and Embolization with Bland Microspheres. *Cardiovasc Intervent Radiol*. 2016;39:1743-1749.
8. Chokkappan K, Kannivelu A, Srinivasan S, Babu S. Review of diagnostic uses of shunt fraction quantification with technetium-99m macroaggregated albumin perfusion scan as illustrated by a case of Osler-Weber-Rendu syndrome. *Ann Thorac Med*. 2016;11:155-160.
9. Kennedy AS, Nutting C, Coldwell D, Gaiser J, Drachenberg C. Pathologic response and microdosimetry of 90Y microspheres in man: Review of four explanted whole livers. *Int J Radiat Oncol Biol Phys*. 2004;60:1552-1563.
10. Vieth M, Montgomery E. Medication-associated gastrointestinal tract injury. *Virchows Arch*. 2017;470:245-266.
11. Bray F, Ferlay J, Soerjomataram I, Siegel RL, Torre LA, Jemal A. Global cancer statistics 2018: GLOBOCAN estimates of incidence and mortality worldwide for 36 cancers in 185 countries. *CA Cancer J Clin*. 2018;68:394-424.
12. Wasan HS, Gibbs P, Sharma NK, et al. First-line selective internal radiotherapy plus chemotherapy versus chemotherapy alone in patients with liver metastases from colorectal cancer (FOXFIRE, SIRFLOX, and FOXFIRE-Global): a combined analysis of three multicentre, randomised, phase 3 trials. *Lancet Oncol*. 2017;18:1159-1171.
13. Van Hazel GA, Heinemann V, Sharma NK, et al. SIRFLOX: Randomized Phase III Trial Comparing First-Line mFOLFOX6 (Plus or Minus Bevacizumab) Versus mFOLFOX6 (Plus or Minus Bevacizumab) Plus Selective Internal Radiation Therapy in Patients With Metastatic Colorectal Cancer. *J Clin Oncol*.

2016;34:1723-1731.
14. Dutton SJ, Kenealy N, Love SB, Wasan HS, Sharma RA. FOXFIRE protocol: An open-label, randomised, phase III trial of 5-fluorouracil, oxaliplatin and folinic acid (OxMdG) with or without interventional Selective Internal Radiation Therapy (SIRT) as first-line treatment for patients with unresectable liver-on. *BMC Cancer*. 2014;14:497.
15. Gibbs P, Heinemann V, Sharma NK, et al. Effect of Primary Tumor Side on Survival Outcomes in Untreated Patients With Metastatic Colorectal Cancer When Selective Internal Radiation Therapy Is Added to Chemotherapy: Combined Analysis of Two Randomized Controlled Studies. *Clin Colorectal Cancer*. 2018;17:e617-e629.
16. Vilgrain V, Pereira H, Assenat E, et al. Efficacy and safety of selective internal radiotherapy with yttrium-90 resin microspheres compared with sorafenib in locally advanced and inoperable hepatocellular carcinoma (SARAH): an open-label randomised controlled phase 3 trial. *Lancet Oncol*. 2017;18:1624-1636.
17. Kennedy A, Brown DB, Feilchenfeldt J, et al. Safety of selective internal radiation therapy (SIRT) with yttrium-90 microspheres combined with systemic anticancer agents: Expert consensus. *J Gastrointest Oncol*. 2017;8:1079-1099.
18. White J, Carolan-Rees G, Dale M, et al. Analysis of a National Programme for Selective Internal Radiation Therapy for Colorectal Cancer Liver Metastases. *Clin Oncol*. 2019;31:58-66.
19. Benson AB, Venook AP, Cederquist L, et al. Colon Cancer, Version 1.2017, NCCN Clinical Practice Guidelines in Oncology. *J Natl Compr Canc Netw*. 2017;15:370-398.
20. Strigari L, Sciuto R, Rea S, et al. Efficacy and toxicity related to treatment of hepatocellular carcinoma with 90Y-SIR spheres: radiobiologic considerations. *J Nucl Med*. 2010;51:1377-1385.
21. Fowler KJ, Maughan NM, Laforest R, et al. PET/MRI of Hepatic 90Y Microsphere Deposition Determines Individual Tumor Response. *Cardiovasc Intervent Radiol*. 2016;39:855-864.
22. Chapiro J, Duran R, Lin M De, et al. Early survival prediction after intra-arterial therapies: a 3D quantitative MRI assessment of tumour response after TACE or radioembolization of colorectal cancer metastases to the liver. *Eur Radiol*. 2015;25:1993-2003.
23. Lin M, Pellerin O, Bhagat N, et al. Quantitative and Volumetric European Association for the Study of the Liver and Response Evaluation Criteria in Solid Tumors Measurements: Feasibility of a Semiautomated Software Method to Assess Tumor Response after Transcatheter Arterial Chemoembolizati. *J Vasc Interv Radiol*. 2012;23:1629-1637.
24. Tacher V, Lin M De, Duran R, et al. Comparison of existing response criteria in patients with hepatocellular carcinoma treated with transarterial chemoembolization using a 3D quantitative approach. *Radiology*. 2016;278:275-

284.
25. Flamen P, Vanderlinden B, Delatte P, et al. Multimodality imaging can predict the metabolic response of unresectable colorectal liver metastases to radioembolization therapy with Yttrium-90 labeled resin microspheres. *Phys Med Biol*. 2008;53:6591-6603.
26. Levillain H, Duran Derijckere I, Marin G, et al. 90Y-PET/CT-based dosimetry after selective internal radiation therapy predicts outcome in patients with liver metastases from colorectal cancer. *EJNMMI Res*. 2018;8:60.
27. Van Den Hoven AF, Rosenbaum CENM, Elias SG, et al. Insights into the dose-response relationship of radioembolization with Resin 90Y-Microspheres: A prospective cohort study in patients with colorectal cancer liver metastases. *J Nucl Med*. 2016;57:1014-1019.
28. Willowson KP, Bernard EJ, Maher R, Clarke SJ, Bailey DL. Changing Therapeutic Paradigms: Predicting mCRC Lesion Response to Selective Internal Radionuclide Therapy (SIRT) based on Critical Absorbed Dose Thresholds: A Case Study. *Asia Ocean J Nucl Med Biol*. 2017;5:66-69.
29. Garin E, Rolland Y, Pracht M, et al. High impact of macroaggregated albumin-based tumour dose on response and overall survival in hepatocellular carcinoma patients treated with 90Y-loaded glass microsphere radioembolization. *Liver Int*. 2017;37:101-110.
30. Mazzaferro V, Sposito C, Bhoori S, et al. Yttrium-90 radioembolization for intermediate-advanced hepatocellular carcinoma: A phase 2 study. *Hepatology*. 2013;57.
31. Högberg J, Rizell M, Hultborn R, et al. Increased absorbed liver dose in Selective Internal Radiation Therapy (SIRT) correlates with increased sphere-cluster frequency and absorbed dose inhomogeneity. *EJNMMI Phys*. 2015;2:10.
32. Walrand S, Hesse M, Jamar F, Lhommel R. A hepatic dose-toxicity model opening the way toward individualized radioembolization planning. *J Nucl Med*. 2014;55:1317-1322.
33. Millar WT. Application of the linear-quadratic model with incomplete repair to radionuclide directed therapy. *Br J Radiol*. 1991;64:242-251.
34. Cremonesi M, Ferrari M, Bartolomei M, et al. Radioembolisation with 90Y-microspheres: Dosimetric and radiobiological investigation for multi-cycle treatment. *Eur J Nucl Med Mol Imaging*. 2008;35:2088-2096.
35. Lassmann M, Chiesa C, Flux G, Bardiès M. EANM Dosimetry Committee guidance document: Good practice of clinical dosimetry reporting. *Eur J Nucl Med Mol Imaging*. 2011;38:192-200.
36. Gill MR, Falzone N, Du Y, Vallis KA. Targeted radionuclide therapy in combined-modality regimens. *Lancet Oncol*. 2017;18:e414-e423.
37. Vauthey JN, Abdalla EK, Doherty DA, et al. Body surface area and body weight predict total liver volume in western adults. *Liver Transplant*. 2002;8:233-240.
38. Cremonesi M, Chiesa C, Strigari L, et al. Radioembolization of hepatic lesions from

a radiobiology and dosimetric perspective. *Front Oncol*. 2014;4:1-20.
39. Kim SH, Kamaya A, Willmann JK. CT perfusion of the liver: Principles and applications in oncology. *Radiology*. 2014;272:322-344.
40. Goetti R, Reiner CS, Knuth A, et al. Quantitative Perfusion Analysis of Malignant Liver Tumors. *Invest Radiol*. 2012;47:18-24.
41. Tofts PS, Brix G, Buckley DL, et al. Estimating kinetic parameters from dynamic contrast-enhanced T1-weighted MRI of a diffusable tracer: Standardized quantities and symbols. *J Magn Reson Imaging*. 1999;10:223-232.
42. Morsbach F, Sah B-RR, Spring L, et al. Perfusion CT best predicts outcome after radioembolization of liver metastases: A comparison of radionuclide and CT imaging techniques. *Eur Radiol*. 2014;24:1455-1465.
43. Giammarile F, Bodei L, Chiesa C, et al. EANM procedure guideline for the treatment of liver cancer and liver metastases with intra-arterial radioactive compounds. *Eur J Nucl Med Mol Imaging*. 2011;38:1393-1406.
44. Bastiaannet R, Kappadath SC, Kunnen B, Braat AJAT, Lam MGEH, de Jong HWAM. The physics of radioembolization. *EJNMMI Phys*. 2018;5:22.
45. Solanki JH, Tritt T, Pasternack JB, et al. Cellular Response to Exponentially Increasing and Decreasing Dose Rates: Implications for Treatment Planning in Targeted Radionuclide Therapy. *Radiat Res*. 2017;188:221-234.
46. Gholami YH, Willowson KP, Forwood NJ, et al. Comparison of radiobiological parameters for 90Y radionuclide therapy (RNT) and external beam radiotherapy (EBRT) in vitro. *EJNMMI Phys*. 2018;5:18.
47. Chiesa C, Mira M, Maccauro M, et al. Radioembolization of hepatocarcinoma with 90Y glass microspheres: development of an individualized treatment planning strategy based on dosimetry and radiobiology. *Eur J Nucl Med Mol Imaging*. 2015;42:1718-1738.
48. Walrand S, Hanin F-X, Pauwels S, Jamar F. Tumour control probability derived from dose distribution in homogeneous and heterogeneous models: assuming similar pharmacokinetics, 125Sn–177Lu is superior to 90Y–177Lu in peptide receptor radiotherapy. *Phys Med Biol*. 2012;57:4263-4275.
49. Barone R, Borson-Chazot F, Valkema R, et al. Patient-specific dosimetry in predicting renal toxicity with (90)Y-DOTATOC: relevance of kidney volume and dose rate in finding a dose-effect relationship. *J Nucl Med*. 2005;46 Suppl 1:99S-106S.
50. Chiesa C, Maccauro M, Romito R, et al. Need, feasibility and convenience of dosimetric treatment planning in liver selective internal radiation therapy with 90Y microspheres: The experience of the National Cancer Institute of Milan. *Q J Nucl Med Mol Imaging*. 2011;55:168-197.
51. Jones LC, Hoban PW. Treatment plan comparison using equivalent uniform biologically effective dose (EUBED). *Phys Med Biol*. 2000;45:159-170.
52. Strigari L, Benassi M, Chiesa C, Cremonesi M, Bodei L, D'Andrea M. Dosimetry in nuclear medicine therapy: radiobiology application and results. *Q J Nucl Med*

Mol imaging Off Publ Ital Assoc Nucl Med [and] Int Assoc Radiopharmacol (IAR), [and] Sect Soc Radiopharm. 2011;55:205-21.

53. Krishnan S, Lin EH, Gunn GB, et al. Conformal radiotherapy of the dominant liver metastasis: A viable strategy for treatment of unresectable chemotherapy refractory colorectal cancer liver metastases. *Am J Clin Oncol Cancer Clin Trials*. 2006;29:562-567.
54. Tai A, Erickson B, Khater KA, Li XA. Estimate of Radiobiologic Parameters From Clinical Data for Biologically Based Treatment Planning for Liver Irradiation. *Int J Radiat Oncol Biol Phys*. 2008;70:900-907.
55. Strigari L, D'Andrea M, Abate A, Benassi M. A heterogeneous dose distribution in simultaneous integrated boost: The role of the clonogenic cell density on the tumor control probability. *Phys Med Biol*. 2008;53:5257-5273.
56. Kalogianni E, Flux GD, Malaroda A. The use of BED and EUD concepts in heterogeneous radioactivity distributions on a multicellular scale for targeted radionuclide therapy. *Cancer Biother Radiopharm*. 2007;22:143-150.
57. Strigari L, D'Andrea M, Maini CL, et al. Biological optimization of heterogeneous dose distributions in systemic radiotherapy. *Med Phys*. 2006;33:1857-1866.
58. Challeton C, Branea F, Schlumberger M, et al. Characterization and radiosensitivity at high or low dose rate of four cell lines derived from human thyroid tumors. *Int J Radiat Oncol Biol Phys*. 1997;37:163-169.
59. Howell RW, Goddu SM, Rao D V. Proliferation and the advantage of longer-lived radionuclides in radioimmunotherapy. *Med Phys*. 1998;25:37-42.
60. Fertil B, Deschavanne PJ, Lachet B, Malaise EP. In Vitro Radiosensitivity of Six Human Cell Lines: A Comparative Study with Different Statistical Models. *Radiat Res*. 1980;82:297.
61. Walrand S, Hesse M, Chiesa C, Lhommel R, Jamar F. The low hepatic toxicity per gray of 90Y glass microspheres is linked to their transport in the arterial tree favoring a nonuniform trapping as observed in post-therapy PET imaging. *J Nucl Med*. 2014;55:135-140.
62. Cremonesi M, Ferrari M, Botta F, et al. Planning combined treatments of external beam radiation therapy and molecular radiotherapy. *Cancer Biother Radiopharm*. 2014;29:227-237.
63. Bodey RK, Flux GD, Evans PM. Combining dosimetry for targeted radionuclide and external beam therapies using the biologically effective dose. *Cancer Biother Radiopharm*. 2003;18:89-97.
64. Delacroix D, Guerre J-P, Leblanc P, Hickman C. Radionuclide and Radiation Protection Data Handbook (2002) (2nd Edition, 2002): Special Issue: Radiation Protection Dosimetry. *Int J Radioact Mater Transp*. 2003;14:77-77.
65. Howell RW, Rao D V, Hou D-Y, Narra VR, Sastry KSR. The Question of Relative Biological Effectiveness and Quality Factor for Auger Emitters Incorporated into Proliferating Mammalian Cells. *Radiat Res*. 1991;128:282.
66. Salvat F, Fernández-Vera J, Sempau J. PENELOPE-2008: A Code System for

Monte Carlo Simulation of Electron and Photon Transport.; 2009.
67. Goddu SM, Howel RW, Bouchet LG, Bloch WE, Rao D. MIRD Cellular S values. Society of Nuclear Medicine; 1997.
68. Ma C-M, Coffey CW, DeWerd LA, et al. AAPM protocol for 40-300 kV x-ray beam dosimetry in radiotherapy and radiobiology. *Med Phys*. 2001;28:868-893.
69. Fiorini F, Kirby D, Thompson J, et al. Under-response correction for EBT3 films in the presence of proton spread out Bragg peaks. *Phys Medica*. 2014;30:454-461.
70. Dale RG. Dose-rate effects in targeted radiotherapy. Vol 41.; 1996.
71. Lea DE, Catcheside DG. The mechanism of the induction by radiation of chromosome aberrations in Tradescantia. *J Genet*. 1942;44:216-245.
72. Dale RG, Jones B. The assessment of RBE effects using the concept of biologically effective dose. *Int J Radiat Oncol Biol Phys*. 1999;43:639-645.
73. Fowler JF. Sensitivity Analysis of Parameters in Linear-Quadratic Radiobiologic Modeling. *Int J Radiat Oncol*. 2009;73:1532-1537.
74. Kutcher GJ, Burman C, Brewster L, Goitein M, Mohan R. Histogram reduction method for calculating complication probabilities for three-dimensional treatment planning evaluations. *Int J Radiat Oncol Biol Phys*. 1991;21:137-146.
75. Niemierko A, Goitein M. Calculation of normal tissue complication probability and dose-volume histogram reduction schemes for tissues with a critical element architecture. *Radiother Oncol*. 1991;20:166-176.
76. Choi B, Deasy JO. The generalized equivalent uniform dose function as a basis for intensity-modulated treatment planning. *Phys Med Biol*. 2002;47:3579-3589.
77. Chiesa C, Mira M, Maccauro M, et al. Radioembolization of hepatocarcinoma with 90Y glass microspheres: development of an individualized treatment planning strategy based on dosimetry and radiobiology. *Eur J Nucl Med Mol Imaging*. 2015;42:1718-1738.
78. Willowson KP, Tapner M, The QUEST Investigator Team, et al. A multicentre comparison of quantitative 90Y PET/CT for dosimetric purposes after radioembolization with resin microspheres: The QUEST Phantom Study. *Eur J Nucl Med Mol Imaging*. 2015;42:1202-1222.
79. Siman W, Mikell JK, Kappadath SC. Practical reconstruction protocol for quantitative 90 Y bremsstrahlung SPECT/CT. *Med Phys*. 2016;43:5093-5103.
80. Nelson A, Swallen A, Arpidone M, Nelson D. Dosimetry for Yttrium-90 Microsphere Brachytherapy. Cleveland, OH; 2017.
81. Lee BQ, Abbott EM, Able S, et al. Radiosensitivity of colorectal cancer to 90Y and the radiobiological implications for radioembolisation therapy. *Phys Med Biol*. 2019;64:135018.
82. Chapiro J, Duran R, Lin M De, et al. Early survival prediction after intra-arterial therapies: a 3D quantitative MRI assessment of tumour response after TACE or radioembolization of colorectal cancer metastases to the liver. *Eur Radiol*. 2015;25:1993-2003.
83. General Electric Company Inc. CT Perfusion 4D User Guide. 2014:81.

84. Irving B. Perfusion-supervoxels for DCE-MRI based tumor subregion assessment. *ISMRM*. 2017.
85. Irving B, Franklin JM, Papież BW, et al. Pieces-of-parts for supervoxel segmentation with global context: Application to DCE-MRI tumour delineation. *Med Image Anal*. 2016;32:69-83.
86. R Development Core Team R. R: A Language and Environment for Statistical Computing. *R Found Stat Comput*. 2011;1:409.
87. Kao YH, Steinberg JD, Tay YS, et al. Post-radioembolization yttrium-90 PET/CT-part 2: Dose-response and tumor predictive dosimetry for resin microspheres. *EJNMMI Res*. 2013;3:1-27.
88. Liu X, Byrne RH. Rare earth and yttrium phosphate solubilities in aqueous solution. *Geochim Cosmochim Acta*. 1997;61:1625-1633.
89. Miura K, Sakata K ichi, Someya M, et al. The combination of olaparib and camptothecin for effective radiosensitization. *Radiat Oncol*. 2012;7:62.
90. Gao X, Saha D, Kapur P, Anthony T, Livingston EH, Huerta S. Radiosensitization of HT-29 cells and xenografts by the nitric oxide donor DETANONOate. *J Surg Oncol*. 2009;100:149-158.
91. Abbott EM, Falzone N, Lee BQ, et al. The impact of radiobiologically informed dose prescription on maximising the clinical benefit of 90Y SIRT in colorectal cancer patients. *J Nucl Med*. 2020:jnumed.119.233650.
92. Pan CC, Kavanagh BD, Dawson LA, et al. Radiation-Associated Liver Injury. *Int J Radiat Oncol Biol Phys*. 2010;76:94-100.
93. Sundlöv A, Sjögreen-Gleisner K, Svensson J, et al. Individualised 177Lu-DOTATATE treatment of neuroendocrine tumours based on kidney dosimetry. *Eur J Nucl Med Mol Imaging*. 2017;44:1480-1489.
94. Howard M, Beltran C, Sarkaria J, Herman MG. Characterization of relative biological effectiveness for conventional radiation therapy: A comparison of clinical 6 MV X-rays and 137Cs. *J Radiat Res*. 2017;58:608-613.
95. Dale RG, Jones B. The assessment of RBE effects using the concept of biologically effective dose. *Int J Radiat Oncol Biol Phys*. 1999;43:639-645.
96. Strigari L, Konijnenberg M, Chiesa C, et al. The evidence base for the use of internal dosimetry in the clinical practice of molecular radiotherapy. *Eur J Nucl Med Mol Imaging*. 2014;41:1976-1988.
97. Kupchak C, Battista J, Van Dyk J. Experience-driven dose-volume histogram maps of NTCP risk as an aid for radiation treatment plan selection and optimization. *Med Phys*. 2008;35:333-343.
98. Porter CA, Bradley KM, Hippeläinen ET, Walker MD, McGowan DR. Phantom and clinical evaluation of the effect of full Monte Carlo collimator modelling in post-SIRT yttrium-90 Bremsstrahlung SPECT imaging. *EJNMMI Res*. 2018;8:7.
99. Dewaraja YK, Chun SY, Srinivasa RN, et al. Improved quantitative ^{90} Y bremsstrahlung SPECT/CT reconstruction with Monte Carlo scatter modeling. *Med Phys*. 2017;44:6364-6376.

100. Rong X, Du Y, Ljungberg M, Rault E, Vandenberghe S, Frey EC. Development and evaluation of an improved quantitative 90Y bremsstrahlung SPECT method. *Med Phys*. 2012;39:2346-2358.
101. Pacilio M, Amato E, Lanconelli N, et al. Differences in 3D dose distributions due to calculation method of voxel S-values and the influence of image blurring in SPECT. *Phys Med Biol*. 2015;60:1945-1964.
102. Cremonesi M, Ferrari ME, Bodei L, et al. Correlation of dose with toxicity and tumour response to 90Y- and 177Lu-PRRT provides the basis for optimization through individualized treatment planning. *Eur J Nucl Med Mol Imaging*. 2018;45:2426-2441.
103. European Parliament. Council Directive 2013/59/Euratom of 5 December 2013 laying down basic safety standards for protection against the dangers arising from exposure to ionising radiation, and repealing Directives 89/618/Euratom, 90/641/Euratom, 96/29/Euratom, 97/43/Euratom a. *Off J Eur Commun L13*. 2014:1-73.
104. Wasan H, van Hazel G, Heinemann V, et al. Overall survival analysis of the FOXFIRE-SIRFLOX-FOXFIRE global prospective randomized studies of first-line selective internal radiotherapy (SIRT) in patients with liver metastases from colorectal cancer. *Ann Oncol*. 2017;28:iii148.
105. Willowson KP, Hayes AR, Chan DLH, et al. Clinical and imaging-based prognostic factors in radioembolisation of liver metastases from colorectal cancer: a retrospective exploratory analysis. *EJNMMI Res*. 2017;7:46.
106. Bhooshan N, Sharma NK, Badiyan S, et al. Pretreatment tumor volume as a prognostic factor in metastatic colorectal cancer treated with selective internal radiation to the liver using yttrium-90 resin microspheres. *J Gastrointest Oncol*. 2016;7:931-937.
107. Kao YH, Hock Tan AE, Burgmans MC, et al. Image-guided personalized predictive dosimetry by artery-specific SPECT/CT partition modeling for safe and effective 90Y radioembolization. *J Nucl Med*. 2012;53:559-566.
108. Smits MLJ, Elschot M, Sze DY, et al. Radioembolization dosimetry: the road ahead. *Cardiovasc Interv Radiol*. 2015;38:261-269.
109. Tong AKT, Kao YH, Too CW, Chin KFW, Ng DCE, Chow PKH. Yttrium-90 hepatic radioembolization: clinical review and current techniques in interventional radiology and personalized dosimetry. *Br J Radiol*. 2016;89:20150943.
110. Coenegrachts K, Bols A, Haspeslagh M, Rigauts H. Prediction and monitoring of treatment effect using T1-weighted dynamic contrast-enhanced magnetic resonance imaging in colorectal liver metastases: Potential of whole tumour ROI and selective ROI analysis. *Eur J Radiol*. 2012;81:3870-3876.
111. Bolch WE, Eckerman KF, Sgouros G, Thomas SR. MIRD Pamphlet No. 21: A Generalized Schema for Radiopharmaceutical Dosimetry--Standardization of Nomenclature. *J Nucl Med*. 2009;50:477-484.

8 Appendix: equations and derivations

Since great effort is required to first appreciate these equations for application specific to ^{90}Y SIRT, they are curated together in this appendix with the aim to avoid a future need to spend time deriving them from scratch. Because these equations are developed from first-principles, the derivations provide multiple different expressions for the same concept, e.g. $EQD = RBE_{max} \cdot \frac{BED_{90Y}}{\left(1+\frac{d}{(\alpha/\beta)_{LINAC}}\right)}$ requires estimates of radiobiological measures RBE_{max}, BED_{90Y}, and $(\alpha/\beta)_{LINAC}$ while the equation $EQD = \frac{\alpha_{90Y}D_{90Y}+\beta_{90Y}D_{90Y}^2}{\alpha_{LINAC}+\beta_{LINAC}\cdot d}$ allows for direct substitution of LQ model fit parameters

8.1 Dosimetry

8.1.1 MIRD formalism

Radiation dose in Gy was calculated using the MIRD formalism (*111*)

$$D(T) = \int_0^T \dot{D}(t)\, dt$$

$$= \int_0^T A(t)S(t)\, dt$$

where $\dot{D}(t)$ is the dose rate, $A(t)$ is the activity, and $S(t)$ is the *S*-value at time t.

For ^{90}Y, the time-activity curve follows exponential decay

$$A(t) = A_0 e^{-\lambda t}$$

where A_0 is the initial activity and λ is the physical decay constant given by $\lambda = \ln 2/T_{phys}$ where T_{phys} is 64.1 hours (the half-life of ^{90}Y).

8.1.2 Decay correction

A general expression reduced to be independent of time is given as $D = \tilde{A} \times S$ where $\tilde{A}$ is the cumulated activity. A general expression for cumulative activity is $\tilde{A} = \int_{t_1}^{t_2} A_0 e^{-\lambda t}\, dt = \frac{A_0}{\lambda}\left[e^{-\lambda t}\right]_{t_2}^{t_1} = \frac{A_0}{\lambda}\,(\, e^{-\lambda t_1} - e^{-\lambda t_2})$ where t_1 is the initial time the radioactivity is exposed and t_2 is the time the radioactivity is removed. If not decay-correcting, then $t_1 = 0$ so the cumulated activity can be expressed as $\tilde{A} = \frac{A_0}{\lambda}(1 - e^{-\lambda t_2})$. If the source is exposed indefinitely, then $t_2 \to \infty$ so the cumulated activity expression reduces to $\tilde{A} = \frac{A_0}{\lambda} e^{-\lambda t_1}$. If not decay correcting and the source is exposed indefinitely, then $t_1 = 0$ and $t_2 \to \infty$ so the cumulated activity simplifies to $\tilde{A} = \frac{A_0}{\lambda}$.

8.2 Determination of *S*-values

8.2.1 Extraction of *S*-values from PENELOPE Monte Carlo simulation

The *S*-value is related to the energy deposited in PENELOPE simulation detector, $\boldsymbol{E}$. The simulation results are posted in a file in the simulation folder, e.g. 'penmain-res.dat'. The line "Average deposited energies (energy detectors):" gives the deposited energy results in each detector. The values are measured per single decay.

The mass of the detector, **m**, was determined based on volume from the geometry file. The density of the detector—the monolayer of cells—was assumed equivalent to water using the relationship $1\ \text{kg} = 1000\ \text{g} = 1000\ \text{cm}^3$.

The following relationships are used to convert the deposited energy to an *S*-value.

$$1\ \text{Gy} = 1\frac{\text{J}}{\text{kg}}$$

$$1\ \text{eV} = 1.61 \times 10^{-19}\ \text{J}$$

$$1\frac{\text{decay}}{\text{second}} = 1\ \text{Bq}$$

$$1\ \text{MBq}\ =\ 10^6\,\frac{\text{decays}}{\text{second}}$$

An example calculation and the general formula are as follows.

$$\boldsymbol{S} = \left(\frac{\boldsymbol{E}\ \cancel{eV}}{\cancel{decay}}\right)\left(\frac{1.61\times10^{-19}\ \cancel{J}}{\cancel{eV}}\right)\left(\frac{Gy\cdot\cancel{kg}}{\cancel{J}}\right)\left(\frac{10^3\ \cancel{g}}{\cancel{kg}}\right)\left(\frac{}{\boldsymbol{m}\ \cancel{g}}\right)\left(\frac{10^6\ \cancel{decays}}{MBq\cdot\cancel{s}}\right)\left(\frac{8.64\times10^4\ \cancel{s}}{d}\right)$$

$$= \frac{\boldsymbol{E}}{\boldsymbol{m}}\times 1.39104\times10^{-5}\left(\frac{Gy}{MBq\cdot d}\right)$$

8.2.2 Derivation of ClonogenCity *S*-values corrected for evaporation

Evaporation of the media from the culture dishes was continuous and variable in the stack. This evaporation changed the depth of media through which the ^{90}Y β radiation travelled, causing significant changes in the MC S-value. Monte Carlo modelling was used to derive S-values based on initial ($S_{initial}$) and final (S_{final}) media volumes adopting a cylindrical geometry for the dishes. The evaporation was described using a linear function assuming a constant rate since the cylindrical geometry means that the surface area from which the evaporation happens is constant at any depth. The intercept was the initial *S*-value ($b = S_{initial}$) and the slope was the rate of change in the S-value $\left(m = \frac{S_{final}-S_{initial}}{T}\right)$ during the total exposure period (T).

$$S(t) = mt + b = \left(\frac{S_{final} - S_{initial}}{T}\right)t + S_{initial}$$

Radiation dose in Gy was calculated based on the MIRD formalism (8.1.1 above). Combining the time-activity curve and linear S-value function of $S(t)$ resulted in the equation where $D(T)$ is the dose for cells exposed to ^{90}Y for duration T:

$$D(T) = \int_0^T \dot{D}(t)\,dt$$

$$= \int_0^T A(t)S(t)\,dt$$

$$= \int_0^T \left(A_0 e^{-\lambda t}\right)(mt + b)\, dt$$

$$= \int_0^T mtA_0 e^{-\lambda t} + bA_0 e^{-\lambda t}\, dt$$

$$= A_0 m \int_0^T te^{-\lambda t}\, dt + A_0 b \int_0^T e^{-\lambda t}\, dt$$

$$= \frac{A_0 m}{\lambda^2}\left[1 - (1 + \lambda T)e^{-\lambda T}\right] + \frac{A_0 b}{\lambda}\left[1 - e^{-\lambda T}\right]$$

$$= \frac{A_0}{\lambda}\left[\frac{m}{\lambda}\left(1 - (1 + \lambda T)e^{-\lambda T}\right) + b\left(1 - e^{-\lambda T}\right)\right]$$

$$= \frac{A_0}{\lambda}\left[\frac{S_{final} - S_{initial}}{\lambda T}\left(1 - (1 + \lambda T)e^{-\lambda T}\right) + S_{initial}\left(1 - e^{-\lambda T}\right)\right]$$

8.3 Radiobiological equations

8.3.1 Biological effect

The biological effect E is obtained as the negative natural logarithm of the measured surviving fraction (SF) of cells after exposure to the absorbed reference radiation dose of D (Gy). The biological effect parameters α (Gy^{-1}) and β (Gy^{-2}) are obtained through multiple regression of E against D and D^2.

$$-\ln(SF) = \alpha D + \beta D^2 = E$$

For exposure to the external beam radiotherapy (EBRT) linear accelerator (LINAC), the above equation can be denoted as follows.

$$-\ln(SF) = \alpha_{LINAC} D + \beta_{LINAC} D^2 = E_{LINAC}$$

When EBRT is delivered n fractions of dose d Gy, the above equation is modified as follows.

$$-\ln(SF) = n \cdot (\alpha_{LINAC} d + \beta_{LINAC} d^2) = E_{LINAC}$$

This denotation can similarly be done for exposure to ^{90}Y SIRT such that

$$-\ln(SF) = \alpha_{90Y} D_{90Y} + \beta_{90Y} D_{90Y}^2 = E_{90Y}$$

However, assuming a direct relationship between LINAC and ^{90}Y SIRT, the biological response parameters can be rewritten in terms of those given for EBRT. $\alpha_{90Y} = RBE_{max} \cdot \alpha_{LINAC}$ due to differences between LET of each radiation source. $\beta_{90Y} = G_T \cdot \beta_{LINAC}$ where the G_T term is the Lea-Catcheside protraction factor for a given exposure period T.

$$-\ln(SF) = (RBE_{max} \cdot \alpha_{LINAC}) D_{90Y} + (G(T) \cdot \beta_{LINAC}) D_{90Y}^2 = E_{90Y} \qquad \textbf{(3)}$$

The full formulation of the Lea-Catcheside protraction factor $G(T)$ given in (*46*) accounts for the interplay between sublethal damage repair μ (h^{-1}) and the physical decay of a given radionuclide λ (h^{-1}).

$$G(T) = G_T = \frac{2\lambda^2}{(\mu - \lambda)(1 - e^{-\lambda T})^2} \left(\frac{1 - e^{-2\lambda T}}{2\lambda} - \frac{1 - e^{-(\lambda+\mu)T}}{\lambda + \mu} \right) \qquad \textbf{(4)}$$

For acute exposure where $T \to 0$, $G(T)$ is unity, as derived in section 8.4.1.1.

$$G(T \to 0) = G_0 = 1$$

For protracted exposure where $T \to \infty$, $G(T)$ reduces to

$$G(T \to \infty) = G_\infty = \frac{\lambda}{\lambda + \mu} = \frac{T_{\text{rep}}}{T_{\text{rep}} + T_{phys}}$$

as derived in section 8.4.1.2, where $\mu = \ln(2) / T_{rep}$ and $\lambda = \ln(2) / T_{phys}$. For ^{90}Y, $T_{phys} = 64.1$ hours.

8.3.2 Biological effective dose

The biological effective dose (BED) is obtained as E/α in Equation 1 as follows.

$$BED = \frac{-\ln(SF)}{\alpha} = D\left(1 + \frac{D}{\alpha/\beta}\right)$$

The ratio α/β is commonly cited as it describes the curvature of the survival curve. Because α/β appears in the BED equation, it is an important derived parameter and is often quoted for radiobiological analysis, e.g. $\alpha_{LINAC}/\beta_{LINAC} = (\alpha/\beta)_{LINAC}$.

The $\left(1 + \frac{D}{\alpha/\beta}\right)$ term is the relative effectiveness (RE). For fractionated EBRT, the RE term is the same despite a total dose $D = nd$:

$$BED_{LINAC} = \frac{-\ln(SF)}{\alpha_{LINAC}} = nd\left(1 + \frac{d}{(\alpha/\beta)_{LINAC}}\right)$$

For exposure to ^{90}Y SIRT, BED can be written based on Equation 4 as $BED_{90Y} = \frac{-\ln(SF)}{\alpha_{90Y}} = D\left(1 + \frac{D}{(\alpha/\beta)_{90Y}}\right)$. However, BED is more useful in terms of EBRT as the reference radiation derived from Equation 5:

$$BED_{LINAC} = \frac{-\ln(SF)}{\alpha_{LINAC}} = D_{90Y}\left(RBE_{max} + G_{\infty}\frac{D_{90Y}}{(\alpha/\beta)_{LINAC}}\right)$$

8.3.3 Equivalent dose

It can be convenient to describe absorbed dose by ^{90}Y SIRT in terms of equivalent dose (EQD) from a fractionated EBRT treatment. This is given as follows and is derived in Section 8.4.2 below).

$$EQD = nd = \frac{RBE_{max} \cdot BED_{90Y}}{\left(1 + \frac{D}{(\alpha/\beta)_{LINAC}}\right)} \approx \frac{RBE_{max} \cdot D_{90Y}}{\left(1 + \frac{D_{LINAC}/n}{(\alpha/\beta)_{LINAC}}\right)}$$

It may be convenient to derive EQD values in terms of LINAC BED values. This allows for easy conversion for different fractionation schedules using simplified terms. The equivalent formula using this approach is

$$EQD = \frac{BED_n}{\frac{1}{D}(BED_N)} = \frac{BED_n}{RE_N}$$

8.3.4 Relative biological effectiveness

Relative biological effectiveness is derived from the LQ model parameters. First demonstrate

$$-\ln(SF) = \alpha D + \beta G D^2$$

$$0 = \beta G D^2 + \alpha D + \ln(SF)$$

$$[-\ln SF]^{-1} = D = \frac{-\alpha \pm \sqrt{\alpha^2 - 4\beta G \ln SF}}{2\beta G}$$

Using the above relationship, an equation for RBE in terms of $\ln SF$ is derived.

$$RBE = \frac{D_{EBRT}}{D_{90Y}} = \frac{[\ln SF]_{linac}{}^{-1}}{[\ln SF]_{90Y}{}^{-1}}$$

$$= \frac{\frac{-\alpha_{EBRT} + \sqrt{\alpha_{EBRT}{}^2 - 4\beta_{EBRT} \ln SF}}{2\beta_{EBRT}}}{\frac{-\alpha_{90Y} + \sqrt{\alpha_{90Y}{}^2 - 4\beta_{90Y} \ln SF}}{2\beta_{90Y}}}$$

$$= \frac{\frac{-\alpha_{EBRT} + \sqrt{\alpha_{EBRT}{}^2 - 4\beta_{EBRT} \ln SF}}{2\beta_{EBRT}}}{\frac{-\alpha_{90Y} + \sqrt{\alpha_{90Y}{}^2 - 4\beta_{90Y} \ln SF}}{2\beta_{90Y}}}$$

$$= \frac{\beta_{90Y}}{\beta_{EBRT}} \cdot \frac{\alpha_{EBRT} - \sqrt{\alpha_{EBRT}{}^2 - 4\beta_{EBRT} \ln SF}}{\alpha_{90Y} - \sqrt{\alpha_{90Y}{}^2 - 4\beta_{90Y} \ln SF}}$$

8.4 Radiobiological equation derivations

8.4.1 Derivation of general Lea-Catcheside protraction (G_T)

For a population of cells $N(t)$ at time t, then the accumulation of lethal and sub-lethal damage exposed to protracted irradiation can be modelled by the following relationship adapted from equation 2.7 of (*33*).

$$\frac{1}{N(t)}\frac{dN(t)}{dt} = -\alpha_{90Y}\dot{D}(t)_{90Y} - 2\beta_{LINAC}\dot{D}(t)_{90Y}\int_0^t \dot{D}(t')_{90Y}e^{-\mu(t-t')}dt'$$

Integration yields an expression of the surviving fraction.

$$\int_0^T \frac{1}{N(t)}\frac{dN(t)}{dt}dt = -\alpha_{90Y}\int_0^T \dot{D}(t)_{90Y}\,dt - 2\beta_{LINAC}\int_0^T \dot{D}(t)_{90Y}\int_0^t \dot{D}(t')_{90Y}e^{-\mu(t-t')}dt'\,dt$$

$$-[\ln N(t)]_0^T = \alpha_{90Y}\int_0^T \dot{D}(t)_{90Y}\,dt + 2\beta_{LINAC}\int_0^T \dot{D}(t)_{90Y}\int_0^t \dot{D}(t')_{90Y}e^{-\mu(t-t')}dt'\,dt$$

$$-[\ln N(T) - \ln N(0)] =$$

$$-\ln\left(\frac{N(T)}{N(0)}\right) =$$

$$-\ln(SF) =$$

The linear quadratic model adapted for dose protraction is given as equation 2.12 from (*33*)

$$-\ln(SF) = \alpha_{90Y}D(T)_{90Y} + 2\beta_{LINAC}\int_0^T \dot{D}(t)_{90Y}\int_0^t \dot{D}(t')_{90Y}e^{-\mu(t-t')}dt'\,dt$$

where $D(T)_{90Y}$ is the total dose after exposure of time T and $t - t'$ is the interval of time after the induction of damage. The following must hold for the sublethal damage term.

$$(G_T \cdot \beta_{LINAC})D(T)_{90Y}^2 = 2\beta_{LINAC}\int_0^T \dot{D}(t)_{90Y}\int_0^t \dot{D}(t')_{90Y}e^{-\mu(t-t')}dt'\,dt$$

$$G_T = \frac{2}{D(T)_{90Y}^2}\int_0^T \dot{D}(t)_{90Y}\int_0^t \dot{D}(t')_{90Y}e^{-\mu(t-t')}dt'\,dt$$

The dose rate for ^{90}Y SIRT at time t is based on the physical decay of ^{90}Y and given by $\dot{D}(t)_{90Y} = \dot{D}_0 e^{-\lambda t}$, where $\dot{D}_0$ is the initial dose rate (Gy/h).

$$G_T = \frac{2}{D(T)_{90Y}^2} \int_0^T \dot{D}_0 e^{-\lambda t} \int_0^t \dot{D}_0 e^{-\lambda t'} e^{-\mu(t-t')} dt'\, dt$$

$$= \frac{2\dot{D}_0^2}{D(T)_{90Y}^2} \int_0^T e^{-\lambda t} \underbrace{\int_0^t e^{-\lambda t'} e^{-\mu(t-t')} dt'}_{I(t)}\, dt$$

For clarity, the inner integral $I(t)$ is solved integrating by substitution:

$$I(t) = \int_0^t e^{-\lambda t'} e^{-\mu(t-t')} dt'$$

$$= \int_{t'=0}^{t'=t} e^{-\lambda t' - \mu(t-t')} dt'$$

$$= \int_{u=-\mu t}^{u=-\lambda t} e^u \left(\frac{du}{\mu - \lambda}\right)$$

$$= \left[\frac{e^u}{\mu - \lambda}\right]_{-\mu t}^{-\lambda t}$$

$$= \frac{e^{-\lambda t} - e^{-\mu t}}{\mu - \lambda}$$

Replacing the inner integral $I(t)$, yields

$$G_T = \frac{2\dot{D}_0^2}{D(T)_{90Y}^2} \int_0^T e^{-\lambda t} \left(\frac{e^{-\lambda t} - e^{-\mu t}}{\mu - \lambda}\right) dt$$

$$= \frac{2\dot{D}_0^2}{D(T)_{90Y}^2} \int_0^T e^{-\lambda t} \left(\frac{e^{-\lambda t} - e^{-\mu t}}{\mu - \lambda}\right) dt$$

$$= \frac{2\dot{D}_0^2}{D(T)_{90Y}^2} \left(\frac{1}{\mu - \lambda}\right) \int_0^T e^{-\lambda t} \left(e^{-\lambda t} - e^{-\mu t}\right) dt$$

$$= \frac{2\dot{D}_0^2}{D(T)_{90Y}^2} \left(\frac{1}{\mu - \lambda}\right) \left\{ \int_0^T e^{-\lambda t} e^{-\lambda t} - e^{-\lambda t} e^{-\mu t}\, dt \right\}$$

$$= \frac{2\dot{D}_0^2}{D(T)_{90Y}^2}\left(\frac{1}{\mu-\lambda}\right)\left\{\int_0^T e^{-2\lambda t}\,dt - \int_0^T e^{-(\lambda+\mu)t}\,dt\right\}$$

$$= \frac{2\dot{D}_0^2}{D(T)_{90Y}^2}\left(\frac{1}{\mu-\lambda}\right)\left\{\left[\frac{e^{-2\lambda t}}{-2\lambda}\right]_0^T - \left[\frac{e^{-(\lambda+\mu)t}}{-(\lambda+\mu)}\right]_0^T\right\}$$

$$= \frac{2\dot{D}_0^2}{D(T)_{90Y}^2}\left(\frac{1}{\mu-\lambda}\right)\left\{\left[\frac{-\left(e^{-2\lambda T}-1\right)}{2\lambda}\right] - \left[\frac{-\left(e^{-(\lambda+\mu)T}-1\right)}{(\lambda+\mu)}\right]\right\}$$

$$= \frac{\dot{D}_0^2}{D(T)_{90Y}^2}\left(\frac{2}{\mu-\lambda}\right)\left[\frac{1-e^{-2\lambda T}}{2\lambda} - \frac{1-e^{-(\lambda+\mu)T}}{(\lambda+\mu)}\right]$$

Substituting $D(T)_{90Y} = \int_0^T \dot{D}_0 e^{-\lambda t}\,dt = \frac{\dot{D}_0}{\lambda}(1-e^{-\lambda T})$

$$= \frac{\dot{D}_0^2}{\frac{\dot{D}_0^2}{\lambda^2}(1-e^{-\lambda T})^2}\left(\frac{2}{\mu-\lambda}\right)\left[\frac{1-e^{-2\lambda T}}{2\lambda} - \frac{1-e^{-(\lambda+\mu)T}}{(\lambda+\mu)}\right]$$

$$= \frac{\lambda^2}{(1-e^{-\lambda T})^2}\left(\frac{2}{\mu-\lambda}\right)\left[\frac{1-e^{-2\lambda T}}{2\lambda} - \frac{1-e^{-(\lambda+\mu)T}}{\lambda+\mu}\right]$$

$$G(T) = G_T = \frac{2\lambda^2}{(\mu-\lambda)(1-e^{-\lambda T})^2}\left(\frac{1-e^{-2\lambda T}}{2\lambda} - \frac{1-e^{-(\lambda+\mu)T}}{\lambda+\mu}\right)$$

8.4.1.1 Lea-Catcheside protraction factor for acute exposure (G_0)

For acute exposure where $T \to 0$, $G(T)$ is unity, found by applying L'Hôpital's rule twice

$$G(T\to 0) = G_0 = \lim_{T\to 0}\left[\frac{2\lambda^2}{(\mu-\lambda)(1-e^{-\lambda T})^2}\left(\frac{1-e^{-2\lambda T}}{2\lambda} - \frac{1-e^{-(\lambda+\mu)T}}{\lambda+\mu}\right)\right]$$

$$= \lim_{T\to 0}\left[\frac{2\lambda^2}{(\mu-\lambda)(1-e^{-\lambda T})^2}\left(\frac{(\lambda+\mu)\left(1-e^{-2\lambda T}\right)}{2\lambda(\lambda+\mu)} - \frac{(2\lambda)\left(1-e^{-(\lambda+\mu)T}\right)}{2\lambda(\lambda+\mu)}\right)\right]$$

$$= \lim_{T\to 0}\left[\frac{2\lambda^2}{(\mu-\lambda)(1-e^{-\lambda T})^2}\frac{(\lambda+\mu)\left(1-e^{-2\lambda T}\right) - (2\lambda)\left(1-e^{-(\lambda+\mu)T}\right)}{2\lambda(\lambda+\mu)}\right]$$

$$= \lim_{T\to 0}\left[\frac{2\lambda^2(\lambda+\mu)\left(1-e^{-2\lambda T}\right) - 2\lambda^2(2\lambda)\left(1-e^{-(\lambda+\mu)T}\right)}{2\lambda(\lambda+\mu)(\mu-\lambda)(1-e^{-\lambda T})^2}\right]$$

$$= \lim_{T\to 0}\left[\frac{\lambda(\lambda+\mu)\left(1-e^{-2\lambda T}\right)-2\lambda^2\left(1-e^{-(\lambda+\mu)T}\right)}{(\lambda+\mu)(\mu-\lambda)(1-e^{-\lambda T})^2}\right]$$

$$\overset{H}{=} \lim_{T\to 0}\left[\frac{\lambda(\lambda+\mu)\left(2\lambda e^{-2\lambda T}\right)-2\lambda^2(\lambda+\mu)\left(e^{-(\lambda+\mu)T}\right)}{(\lambda+\mu)(\mu-\lambda)(2)(1-e^{-\lambda T})(\lambda e^{-\lambda T})}\right]$$

$$= \lim_{T\to 0}\left[\frac{\lambda\left(e^{-2\lambda T}\right)-\lambda\left(e^{-(\lambda+\mu)T}\right)}{(\mu-\lambda)(1-e^{-\lambda T})(e^{-\lambda T})}\right]$$

$$\overset{H}{=} \lim_{T\to 0}\left[\frac{-2\lambda^2\left(e^{-2\lambda T}\right)+\lambda(\lambda+\mu)\left(e^{-(\lambda+\mu)T}\right)}{(\mu-\lambda)(\lambda e^{-\lambda T})(e^{-\lambda T})}\right]$$

$$= \frac{-2\lambda^2\left(e^{-2\lambda 0}\right)+\lambda(\lambda+\mu)\left(e^{-(\lambda+\mu)0}\right)}{(\mu-\lambda)(\lambda e^{-\lambda 0})(e^{-\lambda 0})}$$

$$= \frac{-2\lambda^2(1)+\lambda(\lambda+\mu)(1)}{(\mu-\lambda)(\lambda)(1)}$$

$$= \frac{-2\lambda+(\lambda+\mu)}{(\mu-\lambda)}$$

$$= \frac{\mu-\lambda}{(\mu-\lambda)}$$

$$G_0 = 1$$

8.4.1.2 Lea-Catcheside protraction factor for indefinite exposure (G_∞)

For protracted exposure where $T \to \infty$, $G(T)$ reduces to

$$G(T\to\infty) = G_\infty = \lim_{T\to\infty}\left[\frac{2\lambda^2}{(\mu-\lambda)(1-e^{-\lambda T})^2}\left(\frac{1-e^{-2\lambda T}}{2\lambda}-\frac{1-e^{-(\lambda+\mu)T}}{\lambda+\mu}\right)\right]$$

$$= \frac{2\lambda^2}{(\mu-\lambda)(1-0)^2}\left(\frac{1-0}{2\lambda}-\frac{1-0}{\lambda+\mu}\right)$$

$$= \frac{2\lambda^2}{(\mu-\lambda)}\left(\frac{1}{2\lambda}-\frac{1}{\lambda+\mu}\right)$$

$$= \frac{2\lambda^2}{(\mu-\lambda)}\left(\frac{\lambda+\mu}{2\lambda(\lambda+\mu)}-\frac{2\lambda}{2\lambda(\lambda+\mu)}\right)$$

$$= \frac{2\lambda^2}{(\mu-\lambda)}\left(\frac{\lambda+\mu-2\lambda}{2\lambda(\lambda+\mu)}\right)$$

$$= \frac{2\lambda^2}{(\mu-\lambda)} \frac{(\mu-\lambda)}{2\lambda(\lambda+\mu)}$$

$$G_\infty = \frac{\lambda}{\lambda+\mu}$$

$$= \frac{\lambda}{\lambda+\mu} \cdot \frac{\frac{1}{\mu\lambda}}{\frac{1}{\mu\lambda}}$$

$$= \frac{\frac{1}{\mu}}{\frac{1}{\mu}+\frac{1}{\lambda}}$$

$$= \frac{\frac{T_{rep}}{\ln 2}}{\frac{T_{rep}}{\ln 2}+\frac{T_{phys}}{\ln 2}}$$

$$G_\infty = \frac{T_{\mathrm{rep}}}{T_{\mathrm{rep}}+T_{phys}}$$

8.4.2 Derivation of equivalent dose

Describing absorbed dose by ^{90}Y SIRT in terms of equivalent dose (EQD) from a fractionated EBRT treatment is achieved by equating the biological responses from each modality, as follows.

$$E_{LINAC} = E_{90Y}$$

$$\alpha_{LINAC} BED_{LINAC} = \alpha_{90Y} BED_{90Y}$$

$$\alpha_{LINAC} \cdot nd\left(1+\frac{d}{(\alpha/\beta)_{LINAC}}\right) = \alpha_{90Y} BED_{90Y}$$

EQD is then the equivalent total dose from n fractions of d Gy. Rearranging the above expression yields:

$$EQD = nd = \frac{\alpha_{90Y} BED_{90Y}}{\alpha_{LINAC}\left(1+\frac{d}{(\alpha/\beta)_{LINAC}}\right)}$$

$$= RBE_{max} \cdot \frac{BED_{90Y}}{\left(1 + \frac{d}{(\alpha/\beta)_{LINAC}}\right)}$$

$$= \frac{\alpha_{90Y} D_{90Y} + \beta_{90Y} D_{90Y}^2}{\alpha_{LINAC} + \beta_{LINAC} \cdot d}$$

$$= \frac{E_{90Y}}{RE_{LINAC}}$$

Alternatively, demonstrating the equivalence to ^{90}Y biological dose already measured in terms of BED_{LINAC} units can be a convenient way to convert into EQD. The notation BED'_{LINAC} is applied here to emphasise that ^{90}Y is used in the numerator. First the substitution for ^{90}Y is defined as follows.

$$E_{LINAC} = E_{90Y}$$

$$\alpha_{LINAC} BED'_{LINAC} = \alpha_{90Y} BED_{90Y}$$

$$BED'_{LINAC} = \frac{\alpha_{90Y}}{\alpha_{LINAC}} BED_{90Y}$$

$$BED'_{LINAC} = RBE_{max} \cdot BED_{90Y}$$

Using the above substitution, with respect to the derived EQD equation above, EQD can be expressed for ^{90}Y in terms of BED'_{LINAC}.

$$EQD = nd = RBE_{max} \cdot \frac{BED_{90Y}}{\left(1 + \frac{d}{(\alpha/\beta)_{LINAC}}\right)}$$

$$= \frac{RBE_{max} \cdot BED_{90Y}}{\left(1 + \frac{\frac{D}{n}}{(\alpha/\beta)_{LINAC}}\right)}$$

$$= \frac{RBE_{max} \cdot BED_{90Y}}{\frac{1}{D} \cdot D\left(1 + \frac{D/n}{(\alpha/\beta)_{LINAC}}\right)}$$

$$= \frac{RBE_{max} \cdot BED_{90Y}}{\frac{1}{D} \cdot BED_{LINAC}}$$

$$= D \times \frac{RBE_{max} \cdot BED_{90Y}}{BED_{LINAC}}$$

$$= D \times \frac{BED'_{LINAC}}{BED_{LINAC}}$$

8.5 Error propagation

8.5.1 Propagation of α/β errors

$$\sigma_{\alpha/\beta} = \left(\frac{1}{\beta^2}\right) var\,(\alpha) - \left(\frac{2\alpha}{\beta^3}\right) cov\,(\alpha, \beta) + \left(\frac{\alpha^2}{\beta^4}\right) var\,(\beta)$$

8.5.2 Propagation of errors for derived radiobiological parameters

For a given addition or subtraction involving several variables,

$$P = a + b + \cdots + c - (x + y + \cdots + z)$$

uncertainties are added in quadrature.

$$\sigma_P{}^2 = \sigma_a{}^2 + \sigma_b{}^2 + \cdots + \sigma_c{}^2 + \sigma_x{}^2 + \cdots + \sigma_y{}^2 + \sigma_z{}^2$$

$$\sigma_P = \sqrt{\sigma_a{}^2 + \sigma_b{}^2 + \cdots + \sigma_c{}^2 + \sigma_x{}^2 + \cdots + \sigma_y{}^2 + \sigma_z{}^2}$$

For a given multiplication or division involving several variables,

$$Q = \frac{ab \cdots c}{xy \cdots z}$$

uncertainties are propagated as fractional uncertainties added in quadrature.

$$\left(\frac{\sigma_Q}{Q}\right)^2 = \left(\frac{\sigma_a}{a}\right)^2 + \left(\frac{\sigma_b}{b}\right)^2 + \cdots + \left(\frac{\sigma_c}{c}\right)^2 + \left(\frac{\sigma_x}{x}\right)^2 + \left(\frac{\sigma_y}{y}\right)^2 + \cdots + \left(\frac{\sigma_z}{z}\right)^2$$

$$\sigma_Q = |Q| \sqrt{\left(\frac{\sigma_a}{a}\right)^2 + \left(\frac{\sigma_b}{b}\right)^2 + \cdots + \left(\frac{\sigma_c}{c}\right)^2 + \left(\frac{\sigma_x}{x}\right)^2 + \left(\frac{\sigma_y}{y}\right)^2 + \cdots + \left(\frac{\sigma_z}{z}\right)^2}$$

Therefore, for $RBE_{max} = \alpha_{90Y} / \alpha_{LINAC}$, the expression for uncertainty is:

$$\sigma_{RBE_{max}} = |RBE_{max}| \sqrt{\left(\frac{\sigma_{\alpha_{90Y}}}{\alpha_{90Y}}\right)^2 + \left(\frac{\sigma_{\alpha_{LINAC}}}{\alpha_{LINAC}}\right)^2}$$

For $G_T = \beta_{90Y}/\beta_{LINAC}$, the expression for uncertainty is:

$$\sigma_{G_T} = |G_T| \sqrt{\left(\frac{\sigma_{\beta_{90Y}}}{\beta_{90Y}}\right)^2 + \left(\frac{\sigma_{\beta_{LINAC}}}{\beta_{LINAC}}\right)^2}$$

For $G_\infty = \frac{T_{\mathrm{rep}}}{T_{\mathrm{rep}}+T_{\mathrm{phys}}}$:

$$\sigma_{G_\infty} = |G_\infty| \sqrt{\left(\frac{\sigma_{T_{\mathrm{rep}}}}{T_{\mathrm{rep}}}\right)^2 + \left(\frac{\sigma_{(T_{\mathrm{rep}}+T_{\mathrm{phys}})}}{T_{\mathrm{rep}}+T_{\mathrm{phys}}}\right)^2}$$

and

$$\sigma_{(T_{\mathrm{rep}}+T_{\mathrm{phys}})}{}^2 = \sigma_{T_{\mathrm{rep}}}{}^2 + \sigma_{T_{\mathrm{phys}}}{}^2$$

However, $\sigma_{T_{\mathrm{phys}}} \approx 0$, leaving just

$$\sigma_{(T_{\mathrm{rep}}+T_{\mathrm{phys}})}{}^2 = \sigma_{T_{\mathrm{rep}}}{}^2$$

$$\sigma_{(T_{\mathrm{rep}}+T_{\mathrm{phys}})} = \sigma_{T_{\mathrm{rep}}}$$

Therefore,

$$\sigma_{G_\infty} = |G_\infty| \sqrt{\left(\frac{\sigma_{T_{\mathrm{rep}}}}{T_{\mathrm{rep}}}\right)^2 + \left(\frac{\sigma_{T_{\mathrm{rep}}}}{T_{\mathrm{rep}}+T_{\mathrm{phys}}}\right)^2}$$

For $\frac{G_\infty}{G_6}\beta_{90Y}$, the expression for uncertainty is:

$$\sigma_{\frac{G_\infty}{G_6}\beta_{90Y}} = \left|\frac{G_\infty}{G_6}\beta_{90Y}\right| \sqrt{\left(\frac{\sigma_{G_\infty}}{G_\infty}\right)^2 + \left(\frac{\sigma_{G_6}}{G_6}\right)^2 + \left(\frac{\sigma_{\beta_{90Y}}}{\beta_{90Y}}\right)^2}$$

For $\frac{G_6}{G_\infty}(\alpha/\beta)_{90Y}$, the expression for uncertainty is:

$$\sigma_{\frac{G_6}{G_\infty}(\alpha/\beta)_{90Y}} = \left|\frac{G_6}{G_\infty}(\alpha/\beta)_{90Y}\right| \sqrt{\left(\frac{\sigma_{G_6}}{G_6}\right)^2 + \left(\frac{\sigma_{G_\infty}}{G_\infty}\right)^2 + \left(\frac{\sigma_{(\alpha/\beta)_{90Y}}}{(\alpha/\beta)_{90Y}}\right)^2}$$

8.5.3 Propagation of T_{rep} errors

Applying the uncertainty formula for general functions yields the following relationship:

$$\sigma_{G_T}{}^2 = \sigma_\mu{}^2 \left(\frac{\partial G_T}{\partial \mu}\right)^2 + \sigma_\lambda{}^2 \left(\frac{\partial G_T}{\partial \lambda}\right)^2 + \sigma_T{}^2 \left(\frac{\partial G_T}{\partial T}\right)^2$$

One can approximate the uncertainty of T_{rep} by assuming λ and T are known with zero uncertainty. Therefore, $\sigma_\lambda \to 0$ and $\sigma_T \to 0$ yielding the simplified relationship:

$$\sigma_{G_T}{}^2 = \sigma_\mu{}^2 \left(\frac{\partial G_T}{\partial \mu}\right)^2$$

$$\sigma_\mu{}^2 = \frac{\sigma_{G_T}{}^2}{\left(\frac{\partial G_T}{\partial \mu}\right)^2}$$

However, since $T_{rep} = \frac{\ln(2)}{\mu}$, the uncertainty expression in should be in terms of T_{rep}

$$\sigma_{T_{rep}}{}^2 = \sigma_\mu{}^2 \left(\frac{\partial T_{rep}}{\partial \mu}\right)^2$$

$$= \sigma_\mu{}^2 \left(\frac{\partial}{\partial \mu}\frac{\ln 2}{\mu}\right)^2$$

$$= \sigma_\mu{}^2 \left(\frac{-\ln 2}{\mu^2}\right)^2$$

Substituting $\sigma_\mu{}^2$ from above yields the following expression for $\sigma_{T_{rep}}{}^2$

$$\sigma_{T_{rep}}{}^2 = \frac{\sigma_{G_T}{}^2}{\left(\frac{\partial G_T}{\partial \mu}\right)^2}\left(\frac{-\ln 2}{\mu^2}\right)^2$$

$$\sigma_{T_{rep}} = \frac{\sigma_{G_T}}{\left|\frac{\partial G_T}{\partial \mu}\right|}\left|\frac{-\ln 2}{\mu^2}\right|$$

As no analytical solution exists when solving for $\frac{\partial G_T}{\partial \mu}$, MATLAB's symbolic toolbox yields the following high-precision numeric solution:

$$\frac{\partial G_T}{\partial \mu} = \frac{2\,\lambda^2 \left(\frac{e^{-T\,(\lambda+\mu)} - 1}{(\lambda+\mu)^2} + \frac{T\,e^{-T\,(\lambda+\mu)}}{\lambda+\mu} \right)}{(\lambda-\mu)\,(e^{-T\,\lambda}-1)^2} + \frac{2\,\lambda^2 \left(\frac{e^{-2\,T\,\lambda} - 1}{2\,\lambda} - \frac{e^{-T\,(\lambda+\mu)} - 1}{\lambda+\mu} \right)}{(\lambda-\mu)^2\,(e^{-T\,\lambda}-1)^2}$$

Therefore

$$\sigma_{T_{rep}} = \frac{\sigma_{G_T}}{\left| \frac{2\,\lambda^2 \left(\frac{e^{-T\,(\lambda+\mu)} - 1}{(\lambda+\mu)^2} + \frac{T\,e^{-T\,(\lambda+\mu)}}{\lambda+\mu} \right)}{(\lambda-\mu)\,(e^{-T\,\lambda}-1)^2} + \frac{2\,\lambda^2 \left(\frac{e^{-2\,T\,\lambda} - 1}{2\,\lambda} - \frac{e^{-T\,(\lambda+\mu)} - 1}{\lambda+\mu} \right)}{(\lambda-\mu)^2\,(e^{-T\,\lambda}-1)^2} \right|} \left| \frac{-\ln 2}{\mu^2} \right|$$